Pontificia Universidad Católica del Perú

Escuela de Posgrado

Tesis de Maestría

Control of an Over-Actuated Nanopositioning System by means of Control Allocation

Para optar el grado académico de
Magíster en Ingeniería de Control y Automatización

Presentado por:
Ing. Renzo Andre Seminario Reategui

Profesor Responsable en TU Ilmenau: Prof. Dr.-Ing. Johann Reger Prof. Dr.
Profesor Responsable en PUCP (Asesor): Antonio Manuel Morán Cárdenas

Supervisor en TU Ilmenau: Dr.-Ing. Christoph Weise
Supervisor en IMMS: Dr.-Ing. Stephan Gorges

Noviembre, 2020

Abstract

This Master's Thesis is devoted to the analysis and design of a control structure for the nanopositioning system LAU based on the dynamic control allocation technique. The objective is to control the vertical displacement with nanometer precision under a control effort distribution criterion among the actuator set. In this case, the pneumatic actuator is used as a passive gravity compensator while the voice coil motor generates the transient forces. The analysis of the system characteristics allows defining the design criterion for the control allocation. In this direction, the proposed dynamic control allocation stage considers a frequency distribution of the control effort. The lower frequency components are assigned to the pneumatic actuator while the higher frequencies are handled by the voice coil drive. The significant actuator dynamics are compensated through a Kalman filter approach. The position controller is based on a feedback linearization framework with a disturbance observer for enhanced robustness. The experimental validation demonstrates the feasibility of the proposed technique.

TECHNISCHE UNIVERSITÄT ILMENAU

Department of Computer Science and Automation

Master Thesis

Control of an Over-Actuated Nanopositioning System by means of Control Allocation

---

Submitted by:	Renzo Andre Seminario Reategui
Course of studies:	Technische Kybernetik und Systemtheorie
Manufacture in the field of:	Control Engineering Group
	Department of Computer Science and Automation
Responsible professor at TU Ilmenau:	Prof. Dr.-Ing. Johann Reger
Responsible professor at PUCP:	Prof. Dr. Antonio Morán Cárdenas
Supervisor at TU Ilmenau:	Dr.-Ing. Christoph Weise
Supervisor at IMMS:	Dr.-Ing. Stephan Gorges
Submission Date:	30. 11. 2020

ET LUX IN TENEBRIS LUCET
MCMXVII

Declaration

I declare that the work is entirely my own and was produced with no assistance from third parties. I certify that the work has not been submitted in the same or any similar form for assessment to any other examining body and all references, direct and indirect, are indicated as such and have been cited accordingly.

Ilmenau, den 30. 11. 2020 Renzo Andre Seminario Reategui

ET LUX IN TENEBRIS LUCET
MCMXVII

Kurzfassung

Diese Masterarbeit widmet sich der Analyse und dem Entwurf einer Regelungsstruktur für das Nanopositioniersystem LAU. Dabei werden Methoden untersucht, welche das notwendige Stellsignal auf zwei Aktoren aufteilen. Ziel ist es, die vertikale Verschiebung des LAU mit Nanometerpräzision zu regeln. In diesem Fall wird der pneumatische Aktor als passiver Schwerkraftkompensator verwendet, während die elktromagnetische Tauchspule die transienten Kräfte erzeugt. Die Analyse der Eigenschaften des LAU-Systems ermöglicht die Definition der Entwurfskriterien zur Aufteilung der Stellgröße. In dieser Richtung berücksichtigt die vorgeschlagene dynamische Methode eine Aufteilung der Stellgröße bezüglich der Frequenzanteile. Die niederfrequenten Komponenten werden dem pneumatischen Aktor zugeordnet. Dem elektromagnetische Aktor werden die verbliebenen hochfrequenten Anteile zugeordnet. Die signifikanten Effekte der Aktordynamik in Bezug auf die Bewegungsdynamik werden durch einen Kalman-Filteransatz kompensiert. Nichtlineare Streckenanteile werden basierend auf dem Modell und einem Störbeobachter kompensiert, sodass der verbleibende Anteil des Positionsreglers mit linearen Methoden entworfen werden kann. Die experimentelle Validierung zeigt die Effektivität des untersuchten Konzeptes.

ET LUX IN TENEBRIS LUCET
MCMXVII

Abstract

This Master's Thesis is devoted to the analysis and design of a control structure for the nanopositioning system LAU based on the dynamic control allocation technique. The objective is to control the vertical displacement with nanometer precision under a control effort distribution criterion among the actuator set. In this case, the pneumatic actuator is used as a passive gravity compensator while the voice coil motor generates the transient forces. The analysis of the system characteristics allows defining the design criterion for the control allocation. In this direction, the proposed dynamic control allocation stage considers a frequency distribution of the control effort. The lower frequency components are assigned to the pneumatic actuator while the higher frequencies are handled by the voice coil drive. The significant actuator dynamics are compensated through a Kalman filter approach. The position controller is based on a feedback linearization framework with a disturbance observer for enhanced robustness. The experimental validation demonstrates the feasibility of the proposed technique.

ET LUX IN TENEBRIS LUCET
MCMXVII

Contents

1 Introduction

1.1 Background

Nanotechnology is a foundational, general purpose technology that refers to the research, development and precise manipulation of matter at atomic and molecular level to create structures and systems applicable to a wide range of fields [1–3]. The concept indistinctively applies to an extensive disciplinary spectrum of science and engineering fields. In this sense, nanoscience studies the physical, chemical and biological properties of matter at nanoscale. From that point, engineering develops technology based on these properties to create structures and systems with new capabilities for a wide range of applications in the industry.

Nanotechnology promises a similar impact to the digital revolution capable of a paradigm shift in the industry due to its multiple applications [2]. Nevertheless, the societal and economic impact will be perceivable once the research methods, manufacturing tools and processes are defined. In this direction, the European Association of National Metrology Institutes (EURAMET) traced the Strategic Research Agenda (SRA) for metrology [4] in order to establish a high-level strategic view of measurement capability requirements to suffice the advancement of end-user needs for the next five to ten years. This vision revolves around the main challenges to be undertaken in health, energy and environment while encouraging innovation through metrology to address these concerns. In this context, metrology represents an essential component in scientific research and support for technological innovation, laying the foundations for new industrial processes and products.

In this sense, development in nanometrology enables the further extension of research fields and the implementation of new technologies. Areas such as nanobiotechnology, material science and nanorobotics require high precision nanoinstrumentation capable to measure and implement structures at nanoscale [5, 6]. Under the scope of indus-

trial applications, the SRA retrieves the length realization requirement trend set by International Roadmap for Devices and Systems (IRDS). It considers as a priority the need of research methods for advanced modeling of complex (3D) structures based on improved probe-sample procedures among others.

Under the scope of the semiconductor industry, new manufacturing technologies are required to reach smaller technology nodes and achieve high throughput for massive production. Advanced lithographic and multi-patterning processes are the principal pushing factors of metrology boundaries in dimensional, compositional and doping measurements. However, industrial production based on optical lithography process is approaching a point where it is only profitable under mass production conditions not to mention that reliability issues tend to outcome the benefits.

Beyond CMOS materials, new structures and processes present new challenges for matter manipulation and imagining. The IRDS [7] projects a structure dimension reduction to less than 5 nanometers within the following 10 years. Scaling up to this dimension implies metrology tools capable of characterizing structures in atomic distances while physical limits are being reached. Moreover, stacking technologies used in integrated circuit (IC) manufacture such as 3D, wafer-to-wafer (W2W) and die-to-wafer (D2W) are being further developed aiming to reduce the dimension of the components. The complex 3D structures and new materials used in these methods represent considerable challenges for all metrology areas.

Trending metrology conception considers an integrated vision of metrology data, process information, optimum feedback and real-time process control as key to handle new technology process requirements. Under this scenario, improved metrology techniques in conjunction with new nanofabrication methods and high precision tools are combined to overcome the presented challenges. This includes advances related to 3D structure manufacture and higher complexity due to shrinking dimensions, among others. Success in this task results in increased industrial production while maintaining affordable manufacturing cost.

1.2 Nanofabrication

Optical lithography methods are used in the semiconductor industry due to their resolution and high production throughput. In this direction, an Extreme Ultraviolet

(EUV) lithography machine capable of massive production at 7 nm node was released in 2019 by ASML. For future manufacturing requirements, a technique improvement [8] is being developed with a higher numerical aperture of 0.55 (High-NA) in order to reach 3 nm node structures with an expected performance boost of 70 % with respect to current EUV platform. Despite the promising features, the viability of this technique is limited by the increasing complexity of its implementation pushing its physical limits. As EUV is being adopted by the leading foundries as a new standard in the industry, alternative lithography methods are being researched to comply with IRDS roadmap.

Advances in scanning probe methods are a promising option for nanostructure manufacture. The main concept is based on the use of a fine probe located at the end of a cantilever. As the scanner moves the setup around, it creates a pattern or image on the surface below without the need for a mask. It allows great flexibility to apply a variety of techniques and functions depending on the probe type.

Scanning probe lithography (SPL) methods are able to cover the requirement of material manipulation at atomic level with sub-10 nm resolution for increasing complex patterns leading to 3D structures. It can surpass EUV lithography resolution that is limited by optical diffraction without the need for extreme operating conditions as ultra high vacuum (UHV). Furthermore, sub-10 nm structures, which is considered critical size for any technology, can be patterned at environment conditions and without the need of an etching step depending on the applied method. In addition, proximity effects are minimized in these techniques due to their focalized nature.

SPL can be classified in destructive or constructive approaches according to the interaction with the surface material [9]. Destructive methods remove material from the substrate. This category includes the field-emission SPL (FE-SPL) method [10] that emits low energy (<100 eV) electron beam, triggered by Fowler-Nordheim effect, that exposes the resist-covered substrate. Then, the created pattern is transferred to the wafer by an etching process. It is possible to reach high structure and displacement resolutions, (<5 nm) and (<10 nm) respectively, using a low thicknesses calixarene resist (10 nm). Another method is removal thermal SPL [11] that uses a sharp heated tip to induce local modification on the surface forming high-resolution patterns up to 8 nm half-pitch and capable of 3D structures with 1 nm of vertical resolution.

On the other side, constructive SPL methods allow depositing material on the surface. For instance, Dip-Pen Nanolithography (DPN) [12] is based on the water meniscus

capillarity effect to transport material "inks" (molecules, polymers, nanoparticles, etc.) from the probe tip to the surface.

Certain SPL techniques can be combined with scanning probe microscopy (SPM) for patterning and imaging the surface with the same probe. Particularly, the FE-SPL probe can be modified to include a thermomechanical actuator for atomic force microscopy (AFM) capabilities, so called active cantilever. Dual function cantilevers work based on two independent feedback loops to alternate between both tasks. This configuration makes possible to switch between patterning and imaging functions allowing pre and post surface inspection for error detection and increased accuracy for partial patterns stitching along the wafer as well as overlay alignment.

Tip-based nanofabrication has some drawbacks to be overcome in order to aim for industrial mass production. Due to the SPL and AFM manufacturing process, the probe tip wears out causing degradation in resolution and image quality. The work of Hoffman *et al.* [13] proposes a diamond coated silicon tip for dual FE-SPL and non-contact AFM purposes to counteract the tip deformation thus increasing its utility time. Another aspect is the limited working area below 100 x 100 μm^2 in the *xy* plane and lower than 10 μm in height [14] subjected to the resolution of the probe scanner, thus requiring high alignment accuracy for pattern stitching. Nevertheless, the primary limitation of SPL is its low production throughput compared to optical lithography, as it is a serial process. Throughput enhancement alternatives include using a probe array for parallel patterning, therefore increasing the printed area, produce high resolution templates to be used in Soft UV-Nanoimprint Lithography (Soft UV-NIL), or consider a mix and match approach to combine SPL fine patterns in critical layers and optical lithography for larger features layers.

1.3 Nanomeasurement Machines for Scanning Probe Methods

The small processing range of SPL scanners requires the use of additional methods to cover the large wafer area. The success of these approaches lay on the accurate position of the wafer with respect to the probe for precise stitching or overlay alignment. Nanopositioning and nanomeasuring machines (NPMM) are a motion alternative to probe scanners with large displacement to cover wafer dimensions, high measurement

accuracy and stable nanopositioning dynamics.

As discussed in Weidenfeller *et al.* paper [15], integration of NPMM with SPL techniques offer flexible configurations, increased throughput and improved alignment due to its nanoposition accuracy. For example, pattern task assignment according to critical dimension capability between FE-SPL and Direct Laser Writing (DWL) can produce layers with high detail structures with a mix and match technique. In addition, the master template can be created for Soft UV-NIL to increase throughput. During this process, the NPMM positions the sample to the desired location for patterning or replication by stamping in a side-by-side placement.

The realization of NPMM for large displacement range with nanoposition precision needs to meet higher standards as new design objectives are being developed in the nanotechnology industry [5]. Applications in the sub-nanometer scale not only require high-precision displacement in the xy stage but also needs machines capable of large displacement in the vertical axis to form 3D structures. Holistic design with respect to nanomeasurement strategies, nanoposition and tools to be supported must be considered to reach growing resolution requirements, accuracy, reproducibility and high position dynamics.

The nanomeasuring machine NPMM-200 [5] designed by Technische Universität Ilmenau provides a wide working space of 200 mm x 200 mm x 25 mm. In this approach, the sample is placed on a platform that moves relative and under a probe tool fixed to the NPMM frame. Linear electromagnetic drives, with weight force compensation in the vertical axis to reduce the power consumption, are able to displace the sample stage with a resolution of 0.02 nm.

The system can reach sub-nanometer precision in a large range thanks to the high resolution interferometer measurements (20 pm) and its metrological design based on the 3D realization of the Abbe comparator principle. It is thereby possible to minimize the length measurement errors in the three orthogonal axes by reducing the angular deviations about each one.

The platform displacement and angular deviation are measured by a set of laser interferometers (LIF), angle sensors and mirrors in each axis. A double-beam LIF in each $x-$ and $y-$axes allow determining the rotation about the $z-$axis by value difference. With the same method, the rotation measurement about $x-$ and $y-$axes requires a triple-beam LIF in the $z-$axis below the sample stage. A control loop aims

to keep the angular orientation constant based on the collected data, therefore reducing the length measurement error in all three axes.

To complete the Abbe principle implementation, the probe tip is located at the intersection point of the measuring LIF beams on each axis, so called Abbe point. This fixed point in the space represents the reference point for the sample stage displacement control.

The NPPS100-6D [16] is an alternative nanoposition system presented by IMMS GmbH, that aims for a travel range of 100 mm × 100 mm × 10 mm. It is based on the former NPPS100 system, able to position a slider in the horizontal $xy-$plane and rotate it about the vertical axis with electromagnetic drivers in a friction free framework due to aerostatic guidance. The Abbe comparator concept is maintained with the use of LIF measurements in each motion axis and setting the probe tip in the Abbe point.

The system is extended to 6 degrees of freedom with the support of three vertical lifting and actuating units (LAU). These actuators combine pneumatic and electromagnetic forces to allow the slider displacement in the $z-$direction as well as control the rotation around x- and y-axes. In addition, the LAU is capable to provide passive gravity compensation via its pneumatic force component.

1.4 Actuation in the Vertical Direction

Focusing on the displacement in the vertical axis, the actuator needs to generate enough force to lift the slider and payload mass while keeping high precision and disturbance rejection. Typically, electromagnetic force based actuators, e.g. voice coil motors (VCM), are used for this task due to their high dynamic operation range and precision. However, it has the disadvantage that higher currents mean higher copper losses which increase the temperature. In several applications and with more emphasis on nanoposition, the temperature rise is not desired as disturbances are added to the system [17] [18].

As an alternative, a dual-stage system is considered where the overall force can be divided into two components: a passive gravity compensation and an active force component. The first component provides a constant levitation force around the desired equilibrium point while the latter aims to reach the desired position with precision in a

fine stage and handle disturbances if applicable.

Several devices have been developed to provide gravity compensation based on pneumatic or magnetic forces. For instance, the work of Harbin Institute of Technology [18] proposes an actuator that combines active Lorentz force in four coils and passive magnetic force by magnet arrays. Even though the passive magnetic force between two permanent magnets have highly position-dependent characteristics, the resultant passive levitation force is constant along the ± 1 mm travel range. It has also been demonstrated that the active force has a linear force factor. Furthermore, the vertical actuation in the wafer stage micropositioner used in the work of Gong *et al.* [19] is based on magnetic levitation compensation and voice coils in a water-cooled base to avoid temperature rise.

In the work of Ehsan Asadi *et al.* [20] a modular pneumatic and electromagnetic actuator with high force density and wide bandwidth is developed. The passive compensation is supported by the magnetic force between two magnets with opposite magnetization direction and a pneumatic spring from a constant pressure source. The active force is produced by a vertical coil around the magnet which changes the resultant magnetic field. In consequence, a variation in the initial distance is produced due to the magnetic spring.

1.5 Lifting and Actuating Unit

The device to be controlled in the present thesis is the Lifting and Actuating Unit System (LAU) designed by IMMS GmbH [21]. It is presented as one degree of freedom nanoposition actuator with a large travel range of 10 mm in the vertical axis.

It is a dual-stage system that features a combination of a piston-like pneumatic actuator with an electromagnetic actuator based on a VCM architecture. This arrangement takes advantage of the properties of each independent component able to generate force in the $z-$direction. The pneumatic high density force provides passive gravity compensation, i.e. supports the LAU at the desired position. Whereas the voice coil drive produces dynamic forces in a broad bandwidth for fine positioning and disturbance rejection. With this operation mode, the power consumption of the coil is minimized hence avoiding temperature rise and further disturbances in the system [22].

The LAU consists of a cylindrical structure with two main pieces: a base or stator and a top housing or mover as shown in Figure 1.1. The base structure consists of a planar air bearing at constant 4 bar and a center shaft. The formed air cushion between the base and the surface reduces the vibration transmission into the system. The voice coil is installed around the center shaft and on top of the integrated base cooling channel.

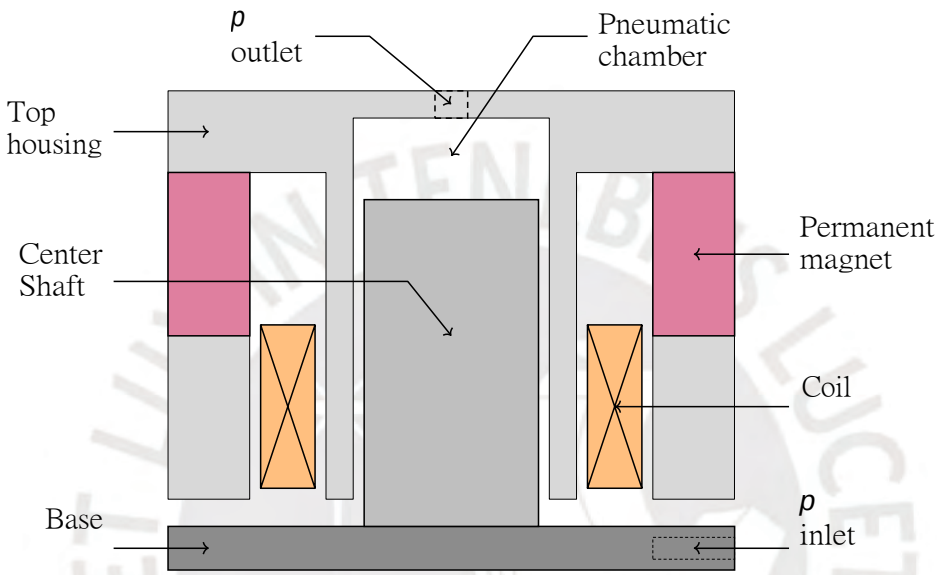

Figure 1.1: LAU structure diagram.

On the other side, the top housing is composed of two rings made of magnetic flux conducting metal with a permanent magnet ring in the middle. This piece provides the magnetic flux for the coil drive at the same time that closes the magnetic circuit and concentrates the flux density in the coil area.

When the base and the top housing fit together, a vertical aerostatic guiding is created that allows frictionless relative displacement between the two pieces. The diameter and height difference between the pieces leaves a cylindrical space and a chamber on top of the shaft respectively. Carved channels in the shaft conduct the airflow from the base into cylindrical space creating a stiff air bearing. Furthermore, this is the pressurized air source to the pressure chamber for pneumatic actuation.

External pressure and current controllers manage the pressure inside the chamber and the coil current, hence the force generated for each actuator. When the force is not enough to lift the top housing, it rests on the base O-ring.

The device also features a linear encoder and a rotational locking based on air bearings supported in a block attached to the side of the main cylindrical structure.

The LAU is designed to be an actuator with linear dynamics, however, the prototype used in this work presents a nonlinear behavior. The reason is the interaction between the ferromagnetic shaft with the magnetic field of the device that results in internal nonlinear forces.

At resting position, the ferromagnetic shaft is magnetized under the constant magnetic field as the attraction force pulls the shaft into the mover. When the top housing moves relative to the base, it causes a flux variation through the shaft that originates magnetic hysteresis [23, 24]. This results in a stroke-dependent residual flux density in the shaft that alters the overall magnetic field in the device. This effect translates into the fluctuation of the electromagnetic attraction force that leads to LAU hysteretic displacement behavior.

Additional magnetic coupling phenomena occur in the shaft during the system operation. The magnetic field from the coil drive can modify the remnant flux density, although it has a minor influence as small currents in the order of μA are intended to be used. The dynamic response of the system, dominated by the pressure controller and airflow dynamics, is also affected by the magnetic damping due to the induced eddy currents that prevent high acceleration.

The hysteresis effect is appreciated in larger strokes in the millimeter range. On the contrary, the resultant magnetic flux at the nanometer scale can be considered constant. The overall effect on the system behavior is discussed in Section 2.3.1.

Reaching sub-nanometer precision presents additional challenges as environmental conditions affect the performance of the equipment. Sources of disturbance include vibration from the surroundings, air drafts and force ripples due to external controllers dynamics that are reflected as position variations. In addition, the coil heat, due to copper losses, produces thermal expansion in the device components, magnetic flux alteration as well as distortions in LIF measurements [18, 19, 25].

Certain design and operation measures can be considered in order to mitigate the influence of environmental disturbances. A controlled ambient temperature and reduced use of the coil helps to avoid the temperature rise in the device. Furthermore, external forces are minimized by encapsulating the system and placing it on an optical table.

1.6 Motivation & Objective

The LAU is a one degree of freedom (DoF) device that consists of two actuators, a voice coil drive and a piston, where both can generate force in the vertical axis to move the top housing to the desired position. The LAU application in nanopositioning systems requires motion over a large displacement range with nanometric precision. For this purpose, the design considers the use of pneumatic force as gravity compensation at equilibrium state while the electromagnetic force handles disturbances and transient behavior. The challenge relies on how to divide the required force between the actuators to accomplish this task.

The main objective of this work is to design a controller for the overactuated LAU system to reach nanometer precision under a force distribution criterion. The system presents three main challenges: hysteretic position behavior, disturbances and temperature increase. The position hysteretic behavior due to an undetermined magnetic force represents an issue for the controller asymptotical stability. The system is also subjected to environmental, electromagnetic and pneumatic disturbances. Furthermore, significant heat distortion can occur in nanoscale applications if high coil currents are used for long periods.

Therefore, the controller design has to consider the complex dynamic behavior of the LAU due to the electromagnetic effects produced by the iron core of the LAU. Thus, the control strategy should be robust against disturbances. Since it is an overactuated system, we use control allocation to obtain adequate handling of each component of the device.

2 System Modeling

2.1 System Architecture

In this section, the overall system is described and implementation considerations are defined. The system architecture is shown in Figure 2.1

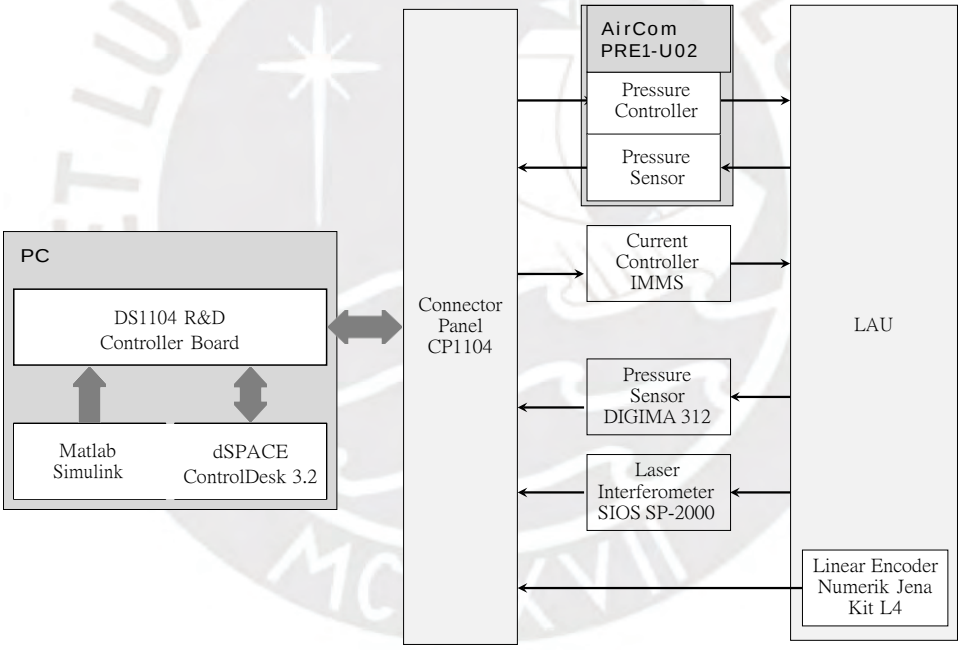

Figure 2.1: LAU System Diagram.

The controller is designed in Matlab Simulink 2007a and implemented on the dSPACE DS1104 Controller Board. The real-time application operates at a sampling rate of 10 kHz and communicates with dSPACE ControlDesk 3.2 for user interface functions.

The LAU is installed on a test bench that provides support for the laser interferometer, force sensor and pressure air lines. It features a movable test load of 0.9164 kg that

travels on the vertical axis. The mass is guided via two air bushings running on two parallel shafts to avoid friction. Also, the maximum travel distance can be fixed by a micrometer screw. The test station is placed on top of an optical table (Newport RS 1000) to reduce environmental vibrations.

The pressure controller (AirCom PRE1-U02) regulates the pressure in the LAU chamber in a range of 0 to 2 bar. It also incorporates a pressure sensor accessible to the system. The coil current is provided by a current controller designed by IMMS GmbH with a ± 1.33 A range. Both controllers receive the setpoint through the 16-bit D/A converter channels that allow a resolution of 30.51 µbar and 40.58 µA respectively.

The LAU displacement measurements are obtained from a laser interferometer (LIF) and a linear encoder. The laser interferometer (SIOS SP-2000) reaches a resolution of 0.3955 nm after interpolation. The interpolator configuration sets the maximum input frequency to 6.25 kHz. Therefore, it limits the maximum traversing speed of the LAU to 1.977 mm s^{-1}. In addition, the linear encoder (Numerik Jena Kit LIK4) integrated into the LAU is capable to measure the position with a precision of 1 µm under a maximum travel speed of 6.6 m s^{-1}.

Both sensors provide quadrature signals to their respective incremental encoder interface on the dSPACE board. Considering the laser interferometer resolution, the 24-bit counter can track up to 3.317 mm. Therefore, a software counter is implemented to cover the entire LAU travel range. The velocity is calculated from the counter pulse delta by the elapsed time. This straight forward implementation is susceptible to errors in case of few pulses counted over a period [26]. This implies that the measurement error increases at low speeds. Under this scenario, the signal is processed by a Kalman filter for a clearer measurement.

Additional sensors are used for testing purposes. A second pressure sensor (DIGIMA 312) located near the LAU pressure chamber helps to compare the pressure transient behavior in the line. While the force sensor (AST KAP-S), with a range of ± 10 N, installed in the test framework can measure the generated force by the LAU actuation components. All the sensors are connected to the parallel A/D converter 12-bit channels.

2.2 Position Measurement Deviation

Since nanopositioning systems are susceptible to environmental conditions, it is of interest to determine their influence on the position measurements. For this purpose, the position variation was recorded over 60 h with the LAU top housing resting on the base O-ring without pressure or current to avoid additional disturbances. Figure 2.2 shows the mean position of data taken in 10 s periods. As result, a position variation is observed in the micrometer range. The mean variance per period is 0.1027 nm^2.

A common source of disturbance may be the temperature change in the laboratory. It is not determined whether it affects the surrounding air of the IF laser beam, causes the LAU structure deformation, or if it is an actual displacement. For the purpose of this work, the IF measurement is assumed to be actual LAU movements.

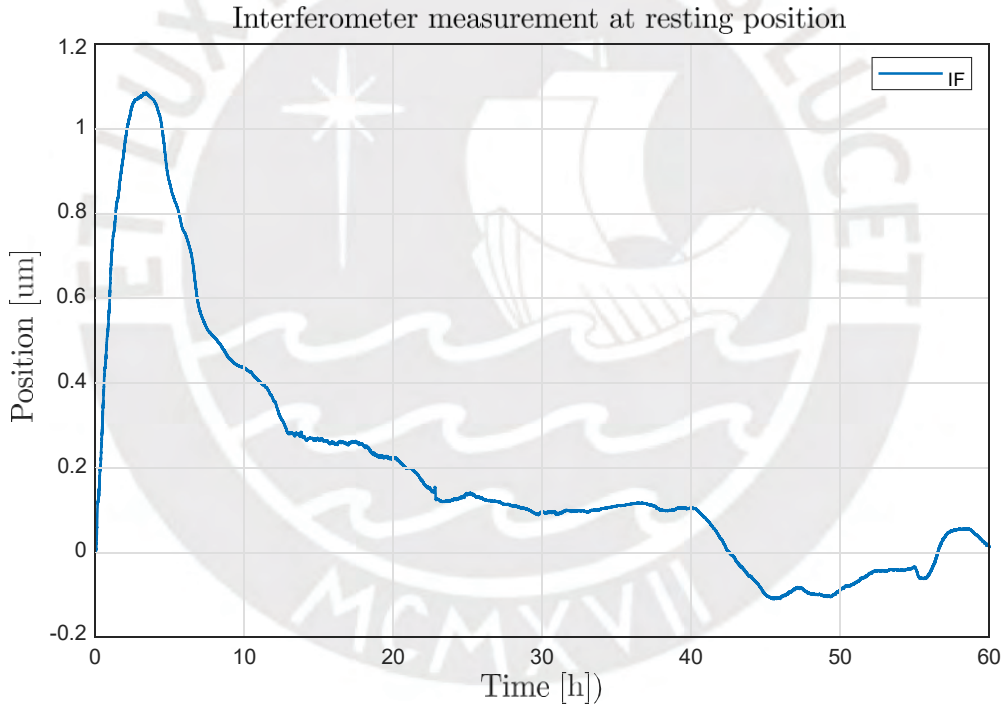

Figure 2.2: Interefometer measurement at LAU resting condition.

2.3 LAU Dynamics

The vertical lifting force generated by the LAU is composed of the pneumatic and electromagnetic forces. Since the force produced by each component is independent, it

is possible to analyze its overall effect on the device. Therefore, the dynamics of the LAU system (see Figure 2.3) can be described by the combination of three components: pressure and electromagnetic dynamics, as well as LAU internal forces.

As mentioned in Section 1.5, the underlying pressure and current controllers aim to maintain their corresponding variable level constant despite changes in the LAU internal parameters. However, the unknown dynamics of the controllers affect the overall LAU behavior.

The objective is to identify the dynamics of each controller and its interaction with the LAU. The performed test considers input signals able to generate sufficient force to move the LAU in the millimeter range.

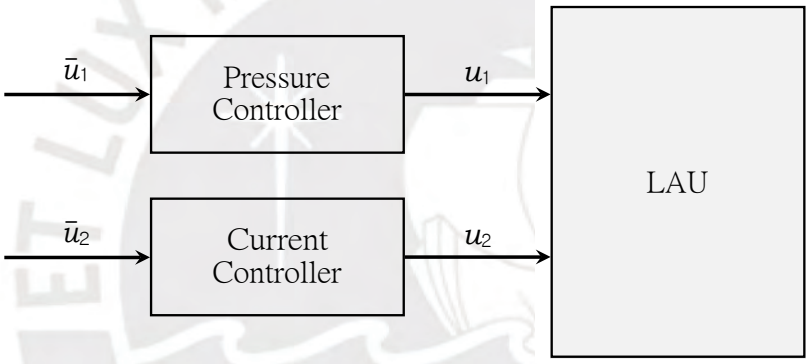

Figure 2.3: LAU system

2.3.1 Characteristic Curve

One tool to identify the system behavior is to analyze its characteristic curve, that is, how the stationary gain varies over the operation range. For this purpose, the pressure input is used since the voice coil does not generate enough force to lift the top housing by itself. Furthermore, the coil electromagnetic field may add magnetic disturbances in the LAU, as discussed in the Section 1.5. The procedure consists of a pressure staircase input with a fixed step size to the open loop system and measure the steady state position until it reaches the maximum travel range. Then return to the initial position by decreasing the pressure in a similar way. The result is shown in Figure 2.4.

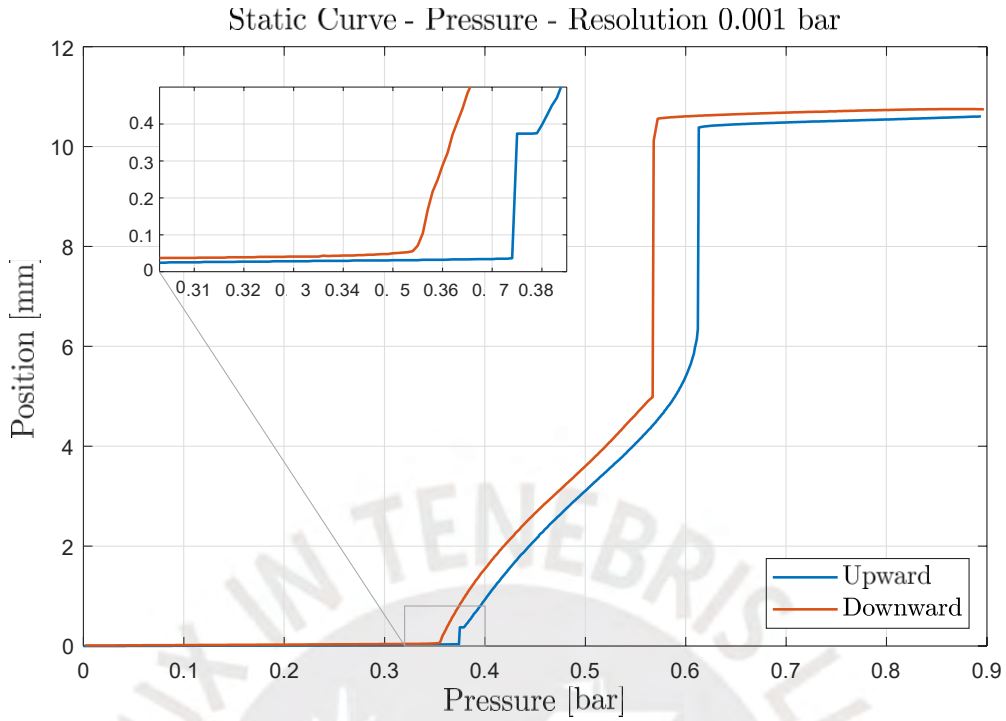

Figure 2.4: Characteristic Curve - Pressure resolution 0.001 bar.

Starting from the resting position at 0 mm with 0 bar, the top housing is in contact with the base O-ring. In this state, the magnetic attraction of the permanent magnet towards the ferromagnetic shaft and the weight force must be overcome. As the chamber pressure increases to 0.374 bar, the pneumatic force is not yet sufficient to fully compensate the initial forces. Nevertheless, a small displacement of 36.48 µm is observed due to the base O-ring deformation.

It is required at least 0.375 bar to produce enough force to significantly move the LAU up in the millimeter range. A position discontinuity due to the loss of contact with the O-ring results in a displacement to 0.374 mm. The upward smooth motion is interrupted at 6.345 mm. A pressure higher than 0.612 bar causes a straight travel to the position limiter of the test framework at 10.5 mm. From this point, the LAU is pushed against the limiter cushion, so the observed displacement is due to its deformation.

The overall downward motion over the travel range has a similar profile to the upward direction but with a pressure offset. When the pressure decreases to 0.568 bar, the position drops from 10.11 mm to 4.979 mm. In this case, the smooth downward motion continues until the top housing lays on the base.

The pressure difference to reach the same position evidence a change in the LAU internal magnetic force over the range of displacement. From the resultant static curve in Figure 2.4, the system requires lower pressure in the downward direction to reach the same position. Furthermore, the internal magnetic force variation produces displacement discontinuities at least in three points.

2.3.2 Magnetic Force Behavior

To study the effect of magnetic force variation, the open loop system response to a pressure square wave input provides additional information. The average step response of a cycle at three different operating points where the system is stable at the stationary point show nonlinear effects (see Figures 2.5, 2.6, 2.7). The output level and transient response to the same step magnitude depends on the operation point. Since no additional external forces are assumed to act on the system, it confirms that the magnetic force changes over the position.

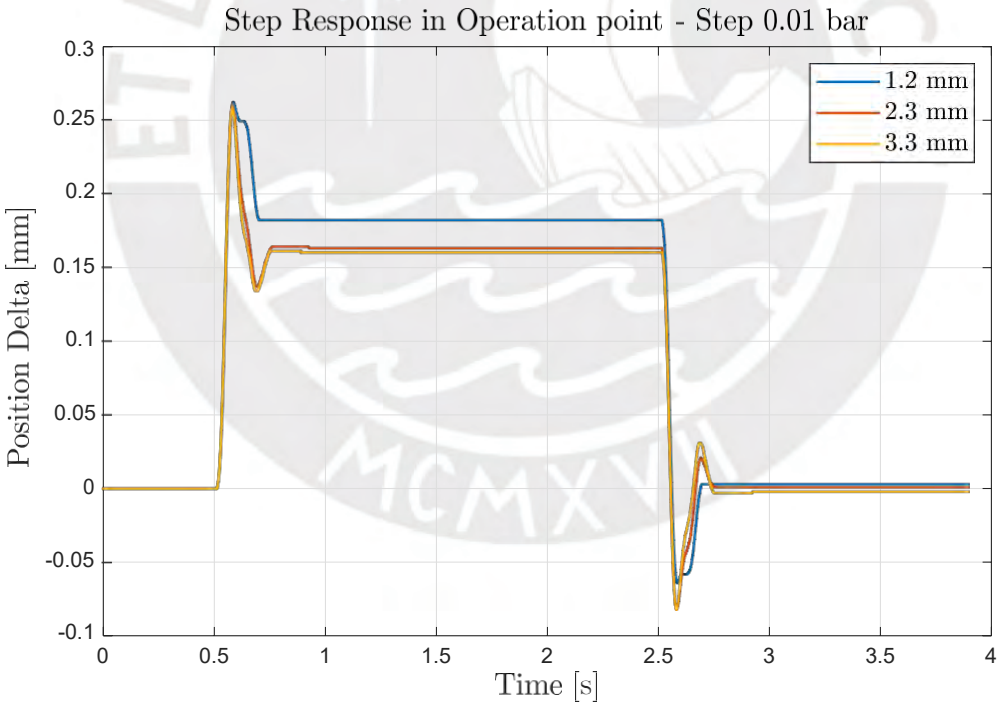

Figure 2.5: Average position response to a pressure step of 0.01 bar.

Furthermore, the final position depends on previous movements and direction. Figure 2.8 compares the system response to different square inputs that start and finish at the same pressure. In both cases, the LAU starts at the same initial position, however,

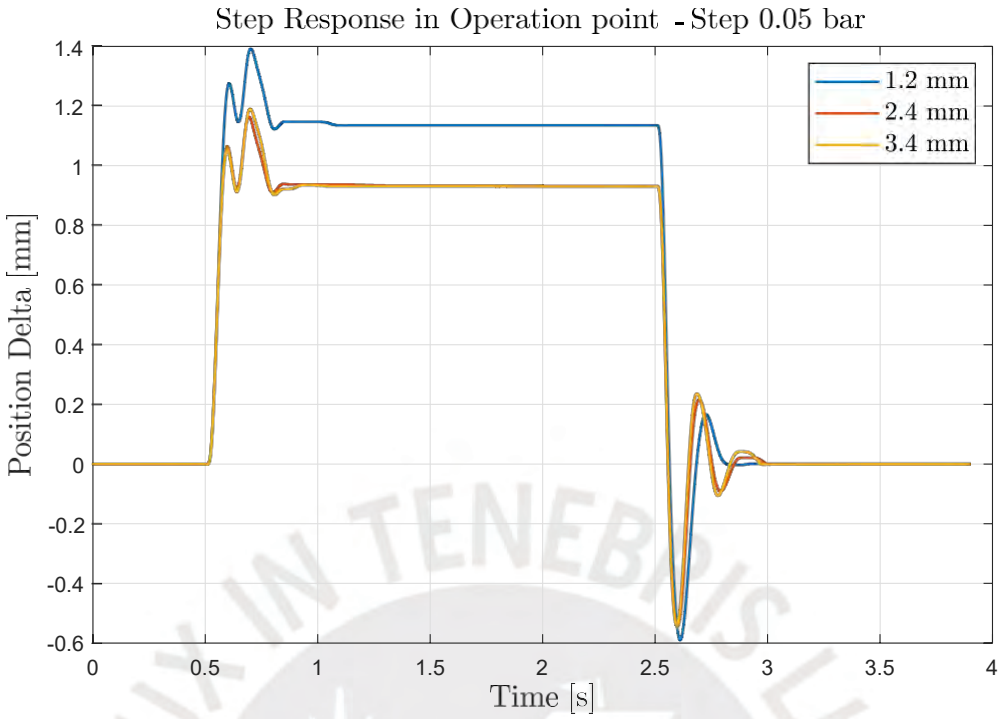

Figure 2.6: Average position response to a pressure step of 0.05 bar.

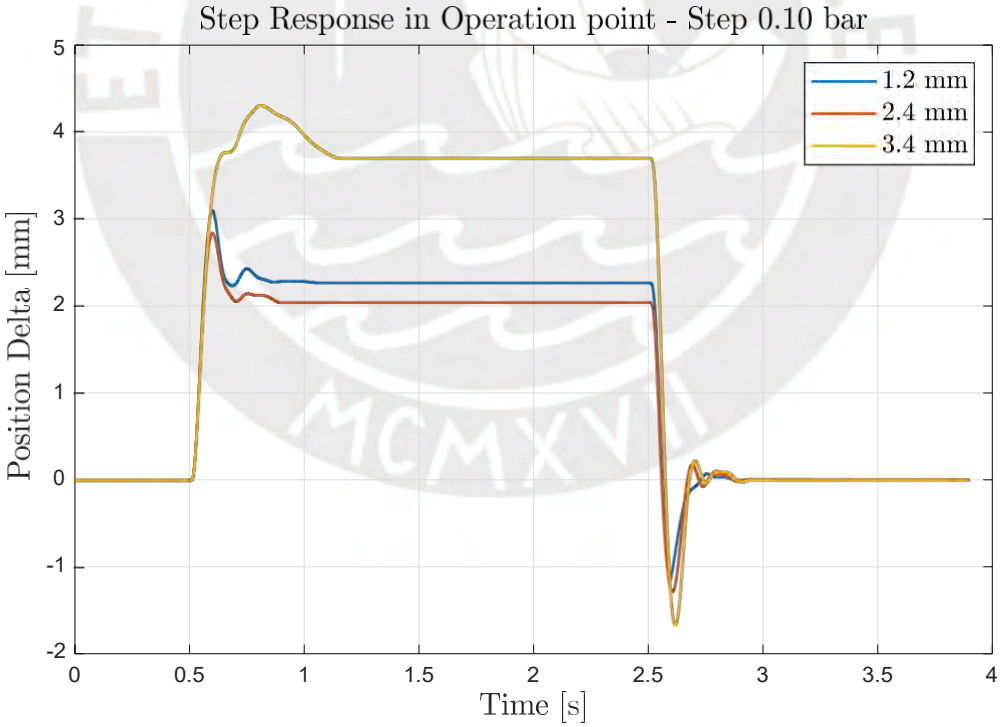

Figure 2.7: Average position response to a pressure step of 0.1 bar.

depending on how the final pressure is reached the final position differs. If the final pressure is reached in one step, the stationary final position is higher than reaching it by a series of smaller steps. The displacement direction also influences the position. Once the final position is reached, the pressure is set back to the initial value through the same input signal in opposite direction. As result, the final position is different from the initial one.

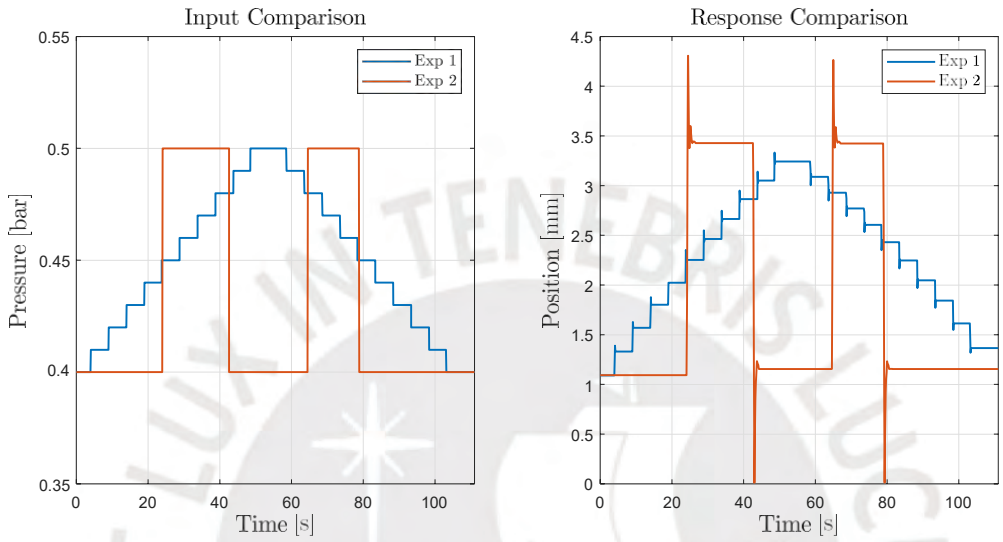

Figure 2.8: Comparison final position to different input history

On a deeper view, it is observed that system orbits in position loops in an input-output graphic. For instance, a periodic stair input oscillates between two position points as shown in Figure 2.8, experiment 1. This behavior is mapped into Figure 2.9 along the characteristic curve position over pressure. In the first cycle, the initial position results from previous history inputs. Nevertheless, the steady position oscillates between two limit points denoted as cycle 2 after the periodic input.

The overall phenomena describes the hysteretic behavior mentioned in Section 1.5. This means that the system states are attracted to different equilibrium points for the same input which leads to different outputs. It can be represented in an input-output graphic as a persistent loop due to a periodic input at the dc limit [27]. In fact, the characteristic curve (Figure 2.4) presents the equilibrium points after a stair step input with a 0.001 bar resolution in the upward and downward direction, therefore, it can be considered as the persistent loop in the static limit.

This the reason why it is not feasible to get an accurate linear model in the millimeter range for inputs other than periodic signals with constant amplitude. On the other

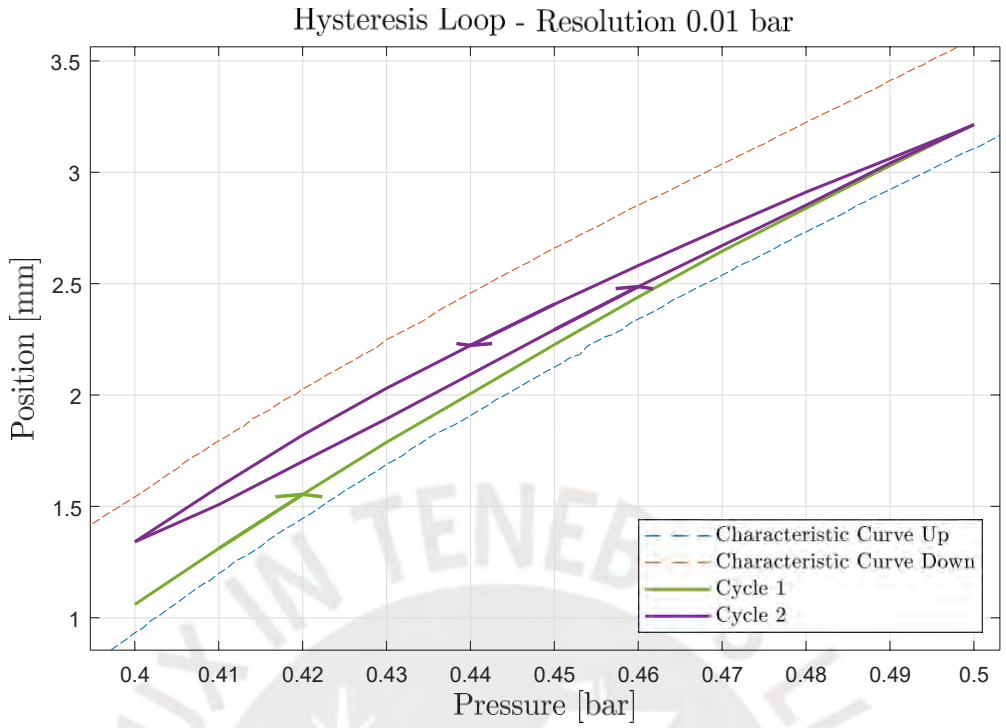

Figure 2.9: Final position comparison to different input history

side, a nonlinear model will increase its accuracy with a hysteresis model component; nonetheless, it is not the main goal of this work. As an alternative, the hysteresis boundaries are delimited and its overall effect on the system is considered as an unknown limited magnetic force. This approach is validated using actual system measurements.

One approach to obtain the magnetic force over the position is based on the characteristic curve information. The measurements at the equilibrium points $\dot{x} = 0$ lead to the following equations:

$$\begin{aligned} F_{\text{pneumatic}} - F_{\text{weight}} - F_{\text{magnetic}} &= 0 \\ F_{\text{magnetic}} &= F_{\text{pneumatic}} - F_{\text{weight}} \end{aligned} \tag{2.1}$$

where $F_{\text{pneumatic}}$, F_{magnetic} and F_{weight} are the pneumatic, magnetic and the total weight force respectively.

It is possible to determine the magnetic force with Equation (2.1) since the total weight and the pressure are known. Nevertheless, there is no information in the characteristic curve measurements in the upper range due to the displacement gap around 6 mm.

An accurate alternative is to use a force sensor to map the magnetic force along the travel range under constant pressure. The experiment setup uses a force sensor in the vertical axis at a fixed position set by a micrometer screw. In this way, it acts as the upper position limit for the LAU. The system is preloaded with a constant pressure of 0.67 bar and the position limit is set to 0 mm. During the experiment, the position limit is gradually moved along the travel range up to 10 mm and returned to the initial position.

The magnetic and normal force due to the force sensor contact are considered to act in the opposite direction to the pneumatic force in the balance of forces as shown in Equation (2.2). Since $F_{\text{pneumatic}}$ and F_{weight} are constant, the variation captured of by force sensor belongs to the magnetic effect. To completely define the magnetic force over the motion range is it required to know the initial value $F_{0\ \text{magnetic}}$. It can be related to the characteristic curve measurements by taking the pressure at 0.375 mm after the first displacement discontinuity and applying the Equation (2.1).

$$F_{\text{pneumatic}} - F_{\text{magnetic}} - F_{\text{sensor}} = F_{\text{weight}} \tag{2.2}$$

$$\Delta F_{\text{magnetic}} = -\Delta F_{\text{sensor}} \tag{2.3}$$

$$F_{\text{magnetic}}(x) = -\Delta F_{\text{sensor}} + F_{0\ \text{magnetic}} \tag{2.4}$$

The resultant magnetic force from the experiment is shown in Figure 2.10. The magnetic force determined by characteristic curve measurements and the method based on the force sensor has a similar profile in the lower section. However, the latter allows mapping the force in a range higher than 5 mm. The values at positions lower than 0.4 mm should not be considered due to the contact with the base O-ring and the initial discontinuity. The negative force in a position lower than 1.75 mm can be interpreted as a small magnetic repulsion. The hysteretic behavior of the system is now isolated in a bounded resultant magnetic force.

The magnetic force curves can be approximated to polynomials of 6 order (see Equations (2.5),(2.6)). The average magnetic force curve (Equation (2.7)) is considered for the implementation in the nonlinear LAU model. Since no hysteresis model is available, the approximation to the average magnetic force may reduce the error with

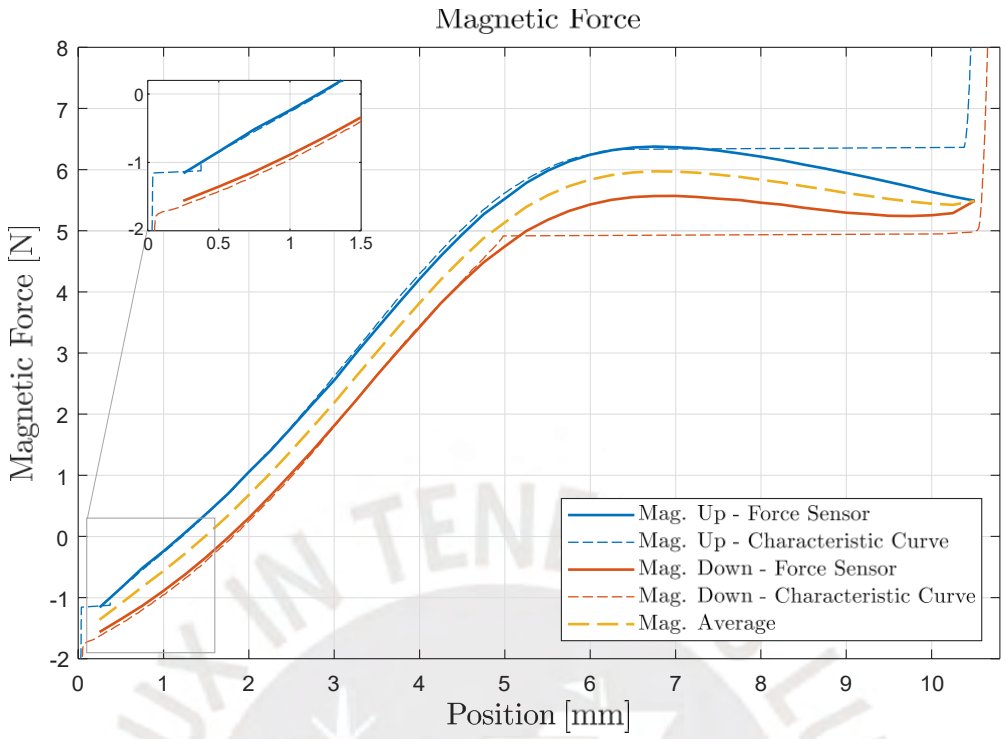

Figure 2.10: Magnetic force determined from experimental data based on force sensor measurements

respect to the real value.

$$F_{\text{magnetic up}}(x) = -0.0002x^6 + 0.0061x^5 - 0.0715x^4 + 0.3441x^3 - 0.6299x^2 + 1.6490x - 1.5349 \tag{2.5}$$

$$F_{\text{magnetic down}}(x) = -0.0001x^6 + 0.0045x^5 - 0.0510x^4 + 0.2130x^3 - 0.1912x^2 + 0.9059x - 1.7757 \tag{2.6}$$

$$F_{\text{magnetic avg}}(x) = -0.0002x^6 + 0.0053x^5 - 0.0614x^4 + 0.2793x^3 - 0.4125x^2 + 1.2795x - 1.6558 \tag{2.7}$$

2.3.3 Hysteresis Range Validation

As demonstrated in the previous section, the characteristic curve profile is related to the magnetic force hysteretic behavior. A method to validate the magnetic force boundaries consists in excite the system with a random square input and map the resultant stationary magnetic force points in the magnetic curve. For this purpose, a random square pressure input between 0.36 and 0.62 bar is used to drive the system in

open loop in its stable region. The resultant stationary position points are identified in Figure 2.11.

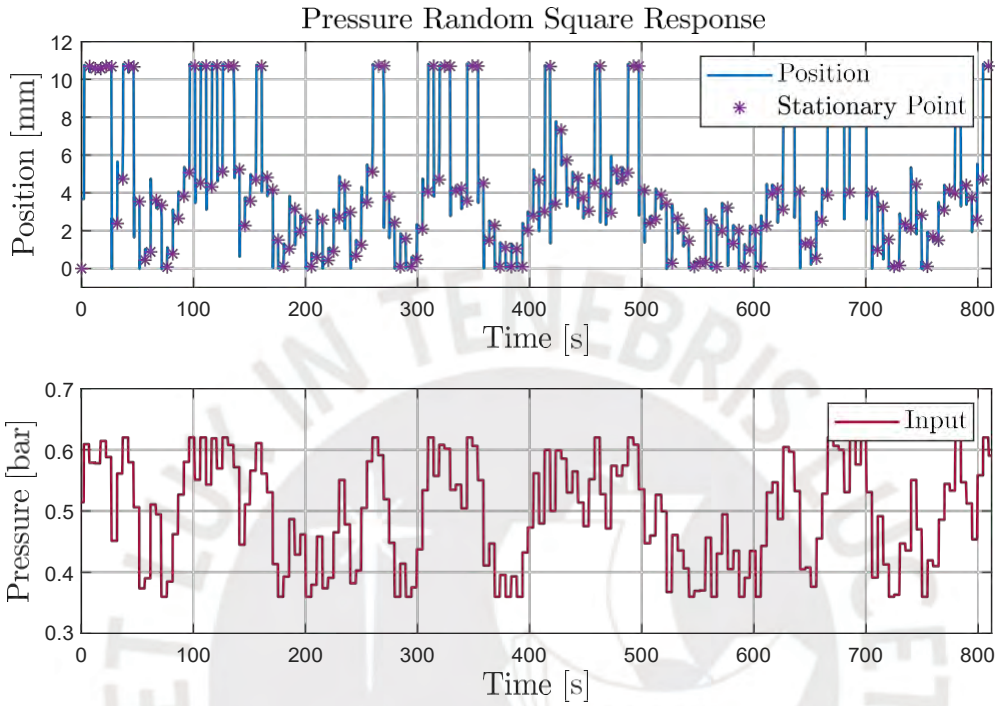

Figure 2.11: Pressure Random Square Response - Stationary Points

The corresponding magnetic force at each stationary point is calculated with the Equation (2.1). Figure 2.12 shows the magnetic force at each position mapped along the hysteresis magnetic loop. As expected, most stationary magnetic force points belong inside the loop boundaries where the system is intrinsically stable. A single stationary point was reached at 7.3 mm during the experiment due to the initial conditions before its respective pressure variation. This evidence the magnetic force variation dependence on the input history. The points above 10 mm are not considered valid because the input pressure lifted the LAU out of the operation range.

In conclusion, the magnetic force is represented by the hysteresis loop. Even though the force is bounded, the precise value at each position in normal operation is still unknown and requires a hysteresis model. The approach in this work considers the average magnetic curve as an attempt to reduce the force error.

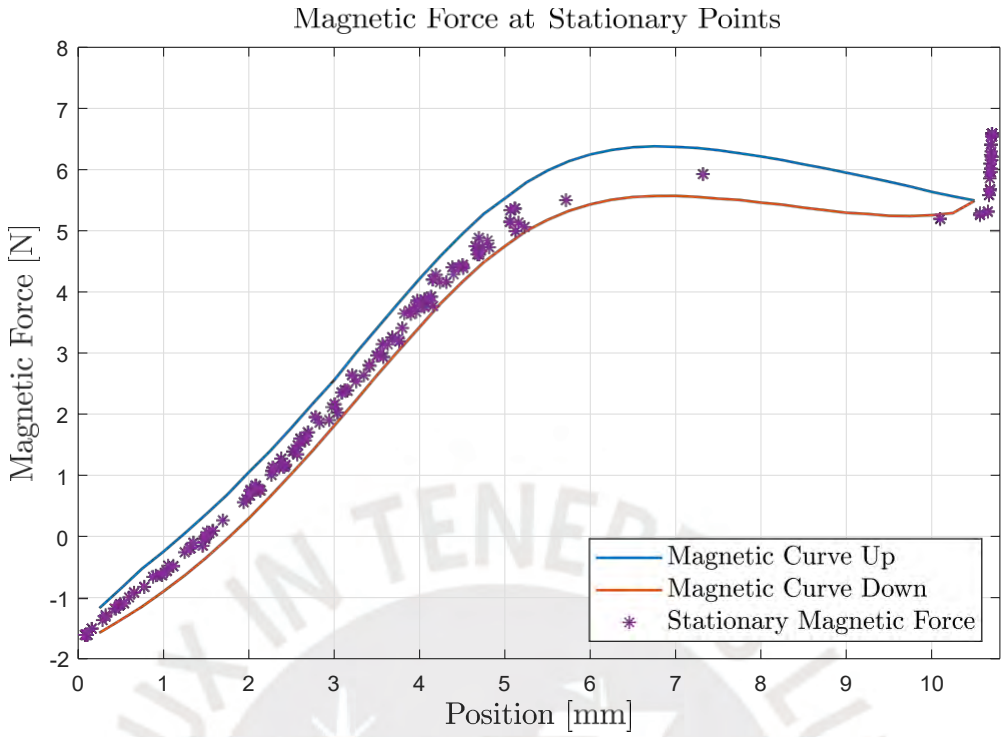

Figure 2.12: Stationary Point Mapping on the Magnetic Loop

2.4 Pneumatic Actuator

The idea behind the LAU is to use pneumatic force to compensate for the weight force of the system. The high force density of the pneumatic actuation ultimately provides the total force required to achieve equilibrium at a specific position, i.e. act as passive gravity compensation.

This is accomplished through the piston-like structure build-in the LAU and connected to the pressure controller. The pneumatic chamber continuously receives pressurized air at 4 bar and an outlet in the top housing allows the connection with the controller through an air hose. In this way, the pressure can be regulated up to 2 bar. That is enough to lift the total mass of 1.317 kg, consisting of the mover and the test mass, up to the maximum travel of 10 mm. This setup creates an air cushion that is modeled as a spring-damper system with a controlled variable spring rate.

For modeling purposes, the pressure p along the mover cross section area A inside the chamber is considered to be uniform and equal to the pressure set by the pressure controller at the other extreme of the air hose at stationary condition. Under this

consideration, the pneumatic force is determined by the Equation 2.8.

$$F_{\text{pneumatic}} = pA \tag{2.8}$$

2.5 Voice Coil Drive

The LAU features an electromechanical actuator based on a voice coil drive. This type of linear motor exhibits high bandwidth and precision. Its basic principle relies on the Lorentz force induced from the interaction between the current I through the coil and a magnetic field [17]. The force equation is given by

$$\vec{F}_{\text{Lorentz}} = \int_{U} I \mathrm{d}\vec{u} \times \vec{B}, \tag{2.9}$$

where $\vec{F}$ is the Lorentz force vector, $\vec{B}$ the magnetic flux density vector, I wire current, U represents the coil section under magnetic flux.

In voice coil motor (VCM) applications, the direction of the resultant force is aligned to the displacement direction, in this case to the vertical axis. The drive structure is designed to make the current and magnetic flux vectors directions perpendicular to each other. The permanent magnet located in the moving cap provides the magnetic field B. The mover structure is made of steel with high magnetic permeability so it acts as a flux conductor creating a magnetic circuit. This circuit is interrupted by an air gap in which the coil is placed such that the magnetic flux is redirected from the steel cap through the coil wires.

The thrust force Equation (2.9) can be formulated with a factor that relates the produced force to the coil current. This proportional factor is called motor constant [$\mathrm{N\,A^{-1}}$] and is given by

$$K_{\text{motor}} = \frac{4 S V_{\text{c}} B_{\text{gap}}}{\pi d^2}, \tag{2.10}$$

where V_{c} is the total volume of the coil, B_{gap} the magnetic flux in the air gap, d diameter of the conducting wire and $S \in [0, 1]$ is the ratio of the coil section under the magnetic flux (see [17]).

Hence, the Equation (2.9) can be further reduced to Equation (2.11) under a constant magnetic flux and coil volume.

$$F_{\text{Lorentz}} = K_{\text{motor}}\, I \tag{2.11}$$

2.5.1 Motor Thrust Factor

The coil drive has a moving magnet approach design where the coil is fixed to the base. This results in a relative movement between the coil and the top housing. As the cap moves in the positive direction in the vertical axis, the coil volume under the magnetic flux decreases. From Equation 2.9 the generated force is proportional to the intensity of the magnetic flux through the wires [28]. Thus, at constant current, the VCM thrust force changes over the position as the amount of coil wires under the flux varies.

In addition, the center shaft magnetization hysteresis described in Section 2.3.2 affects the overall magnetic flux over the travel distance. The coil drive operation also produces a magnetic field that may change the magnetization of the ferromagnetic shaft, then altering the resultant flux over the wires. Nevertheless, this effect is disregarded as the flux intensity generated by the coil current is reduced as it is intended to be used with small currents in the order of milliamperes. Under this premise, the demagnetization of the permanent magnet is also discarded.

In consequence, the resulting thrust force generated by a settled current is not constant over the position. So instead of a constant motor factor, the force can be related to the current by a position varying parameter.

In order to capture the previous effects, this parameter is obtained experimentally using a force sensor. The experiment consists of two stages: (i) obtaining the motor parameter at a certain position and then (ii) mapping its variation along the position range. The experimental setup uses a force sensor in the vertical axis in a fixed position that can be set with the help of a micrometer. In this way, it will act as the upper position limit for the LAU.

In the first stage, the idea is to measure the thrust force variation caused by a change in the voice coil current. The LAU is preloaded with a constant pressure that lifts the mover to 4 mm, where the force sensor is located until it registers a force offset.

Equation (2.12) shows the force balance at the equilibrium:

$$F_{\text{coil}} + F_{\text{pneumatic}} - F_{\text{weight}} - F_{\text{magnetic}} = F_{\text{sensor}} \tag{2.12}$$

where F_{coil} is the electromagnetic force generated by the voice coil and F_{sensor} the measured force by the load cell.

After a current step, the voice coil drive produces a force change measured by the sensor. Note that the force sensor also acts as a position limit, therefore, the position variation is minimal. Ideally, the system should be in equilibrium during the experiment, that is, the acceleration of the LAU should be 0. However, a position deviation was captured since the force sensor stiffness is not high enough. This difference is up to 60 μm after a 500 mA step. Moreover, the sensor still measures a force delta after the current excitation return to its initial value. This effect reveals the nonlinear internal force change in the system corresponding to the hysteresis magnetic force change.

Despite the mentioned phenomena, its influence on the motor parameter measurement is considered negligible. The LAU operation intends to use current magnitudes in the milliampere range, so a similar motor parameter profile is expected. Based on this consideration, F_{magnetic} is assumed to be constant in the test, as well as $F_{\text{pneumatic}}$ and F_{weight}. Therefore, the force variation corresponds to the force induced in the coil.

$$\Delta F_{\text{coil}} = \Delta F_{\text{sensor}} \tag{2.13}$$

Hence, the relation of the thrust force to current at a specified operating point is represented by

$$K_{\text{motor}} = \frac{\Delta F_{\text{sensor}}}{\Delta I} \tag{2.14}$$

The procedure is repeated in the same position with different step sizes. Figure 2.13 shows the results of the experiment at a fixed position of 4 mm. The relation of the force variation with respect to the current presents a linear behavior, where the slope is the force factor.

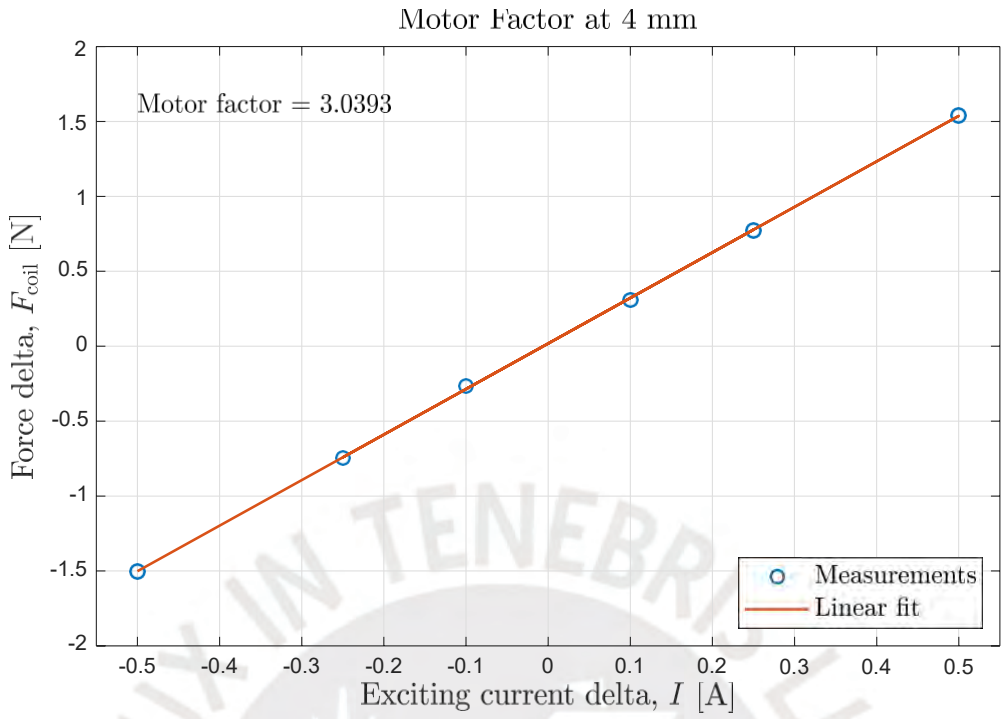

Figure 2.13: Motor Factor at 4 millimeters.

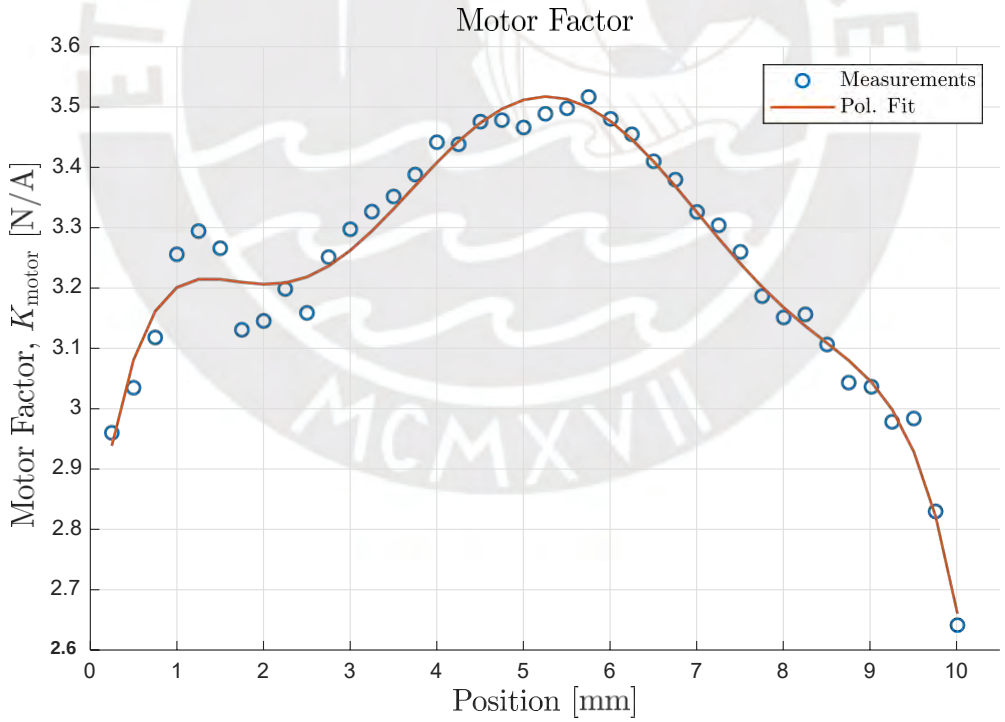

Figure 2.14: Average motor factor - Resolution 0.25 mm, Current step +-250 mA.

In the second stage, this procedure is repeated to cover the complete travel range of the LAU in the upward and downward direction. Figure 2.14 presents the average motor factor behavior along the position. As expected, the thrust force produced by the current changes along the position. The measurements are fitted to a polynomial of 6 order given by Equation (2.15) for its implementation in the system model.

$$\begin{aligned} K_{\text{motor}}(x) = &-0.0002x^6 + 0.0052x^5 - 0.0617x^4 \\ &+ 0.3445x^3 - 0.9160x^2 + 1.1171x + 2.7123 \end{aligned} \tag{2.15}$$

where x is the LAU position in mm and K_{motor} in $\mathrm{N\,A^{-1}}$.

2.6 Controller Dynamics

The LAU movement is produced by the force generated due to the chamber pressure and the coil current. These magnitudes depend on the setpoint provided by the position controller and the dynamics of each controller. In this sense, the identification of the pressure and current controllers enhances the accuracy of the model and provides information about the system characteristics. For this purpose, the systems are identified through a pseudo-random binary sequence (PRBS) as persistent excitation in order to obtain a model and its respective operation bandwidth. This information is useful to establish a criterion design for the system controller.

2.6.1 Pneumatic Dynamics

The model intends to include the AirCom pressure controller and the air transmission dynamics. For this purpose, the pressure setpoint and the pressure near the LAU outlet (DIGIMA 312) are defined as the input and output of the system respectively, as shown in Figure 2.15. Under this scenario, the steady and dynamic response are analyzed.

At steady state condition, the controlled pressure presents a disturbance component that is reflected as position variation in the LAU. Under a constant pressure setpoint of 0.45 bar, the filtered pressure measurement near the LAU shows a pressure offset with respect to the desired one with disturbances and peaks over time.

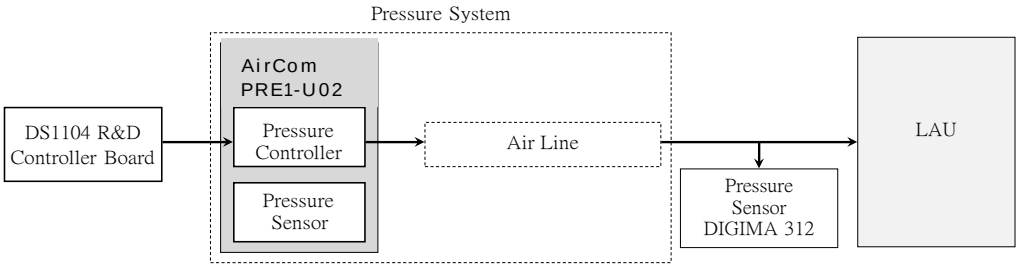

Figure 2.15: Pressure system diagram

The pressure variation is reflected as LAU position change that, influenced by the hysteresis effect, produces a displacement in the micrometer scale (see Figure 2.16). The position variance is 14×10^3 nm^2 in a period of 100 s, higher than at resting position. From the control point of view, this effect represents an input disturbance to be compensated by the position controller.

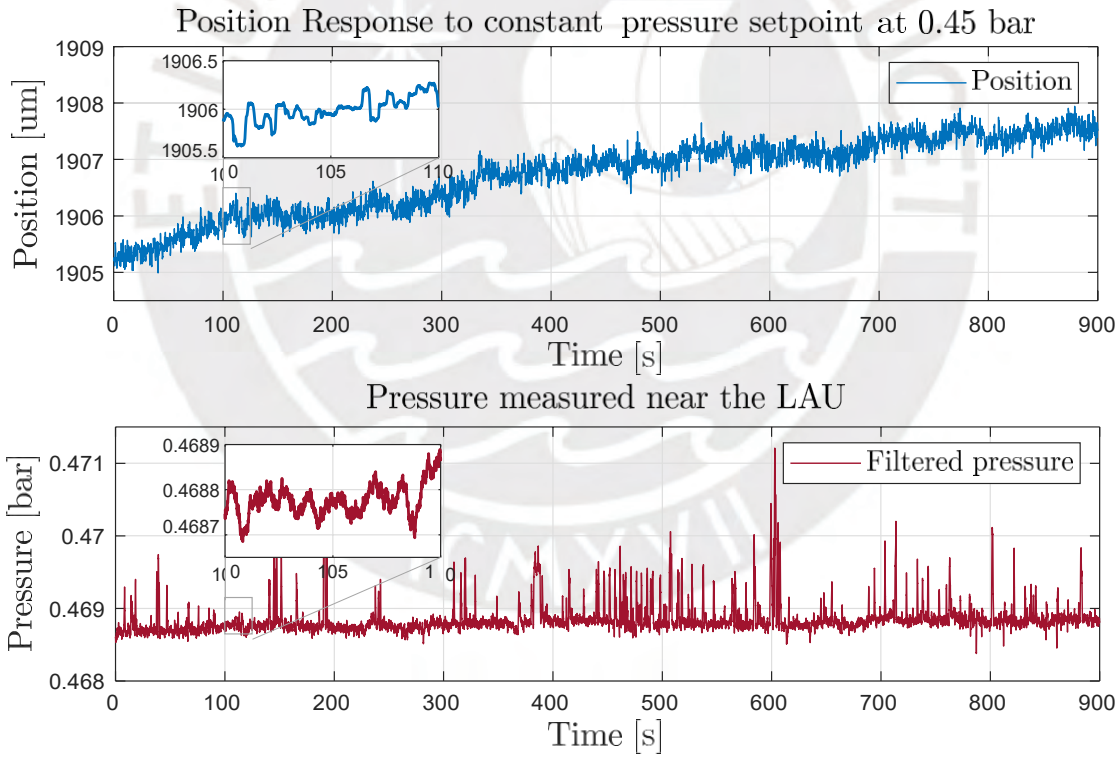

Figure 2.16: Position response to constant pressure at 0.45 bar

An overview of the dynamic behavior can be represented by the system response to pressure step of 0.05 bar at 2.4 mm. Figure 2.17 compares the resultant pressure and position variation.

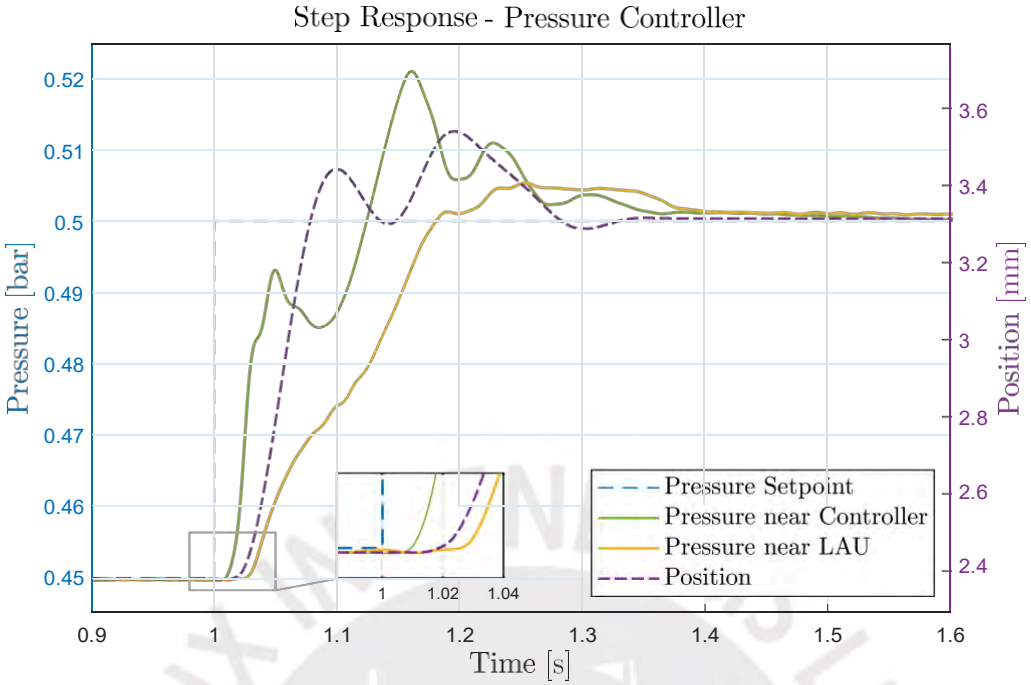

Figure 2.17: Step Response - Filtered pressure measurement at the extremes of the air line compared to position.

The transient response denotes a nonlinear behavior with delay. The initial pressure near the controller and at the end of the air line has a delay of 8 ms and 24 ms from the input step rise, respectively. Despite the characteristics of the pressure near the LAU, the rise time of the position response is closer to the pressure right after the controller with a delay of 14 ms. Also, it is possible to appreciate the clear phase difference between the pressure near the controller and the position response. This means that the pressure inside the chamber has more affinity to the initial pressure curve measurement.

Based on this assumption, the pressure response near the controller is approximated to a second order model without delay. An initial model is obtained from the pressure PRBS response, where its natural frequency ω_n and damping ratio ζ are then optimized to improve the position fit of the overall LAU model. The transfer function expressed in the Equation (2.16) is governed by the rise time of the first pressure peak with a response fit of 95.31%. It is a stable system with poles in $-58.32 \pm 74.83i$ in the negative left side of the s-plane with a bandwidth of 17.04 Hz determined using the Equation (2.17) [29].

$$G_{\text{pneumatic}}(s) = \frac{9001.4}{s^2 + 116.64s + 9001.4}, \qquad \omega_n = 0.6147,\ \zeta = 94.876 \tag{2.16}$$

$$BW = \omega_n \left[(1 - 2\zeta^2) + \sqrt{4\zeta^4 - 4\zeta^2 + 2} \right]^{1/2} \text{rad s}^{-1} = 17.04\,\text{Hz} \tag{2.17}$$

The step response of the obtained model and the pressure measurement are compared in Figure 2.18. The model follows the first pressure peak that leads to a closer approximation to the pressure system bandwidth. Since it is a linear second order model, it is not capable to match the pressure transient behavior.

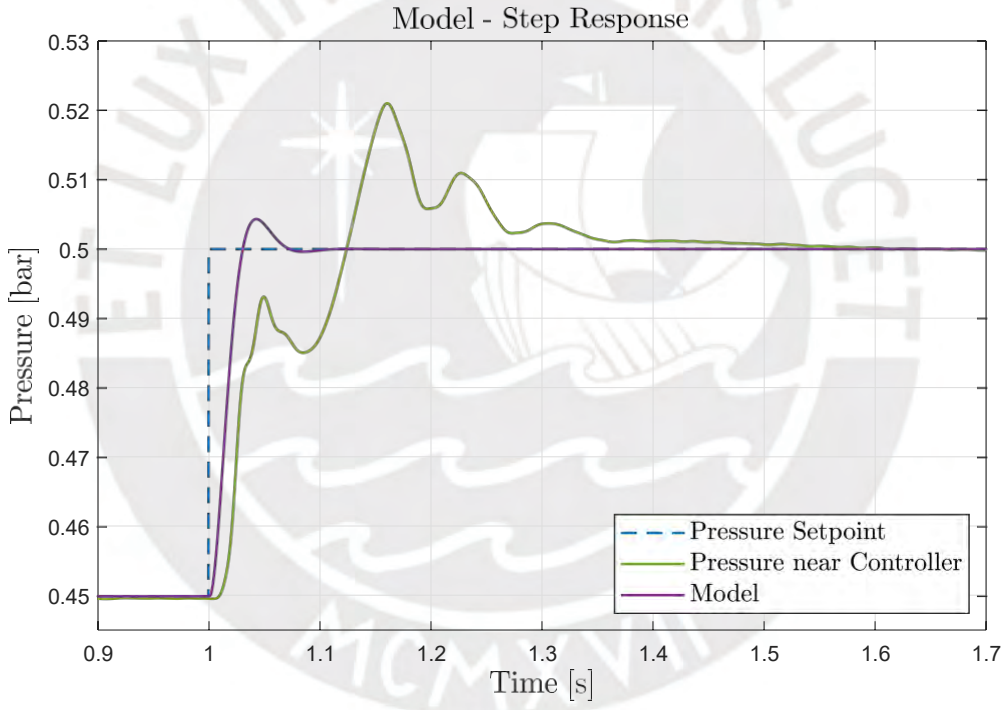

Figure 2.18: Step Response - Comparison between model and filtered measured pressure.

The pressure model is validated in a later stage where the LAU model position response is compared using two different pressure models, each one based on the pressure measurements at one of the extremes of the air hose. As result, the position transient response is improved with the model based on the pressure near the controller, which supports the previous assumption.

Finally. an output disturbance $d_p(s)$ is added to the nominal model $G_{pneumatic}(s)$ to cope with unmodeled dynamics and the pressure variation shown in Figure 2.16, then

$$u_1(s) = G_{pneumatic}(s)\bar{u}_1(s) + d_p(s), \tag{2.18}$$

where $\bar{u}_1$ is the controller setpoint and u_1 is the actual pressure delivered to the LAU.

2.6.2 Current Dynamics

A model of the current controller dynamics provides information about the electromagnetic force response bandwidth. The subsystem to be identified considers the current controller while is it connected to the LAU voice coil. In this scenario, the controller has to compensate for the back electromagnetic force and internal magnetic field changes in the LAU.

For the identification process, the LAU is set in the middle of the operating range by a constant pressure offset of 0.5 bar. The response to a current step (see Figure 2.19) is approximated to a first order model expressed in Equation (2.19). The model time constant τ results in a bandwidth of 4.2 kHz using Equation (2.20).

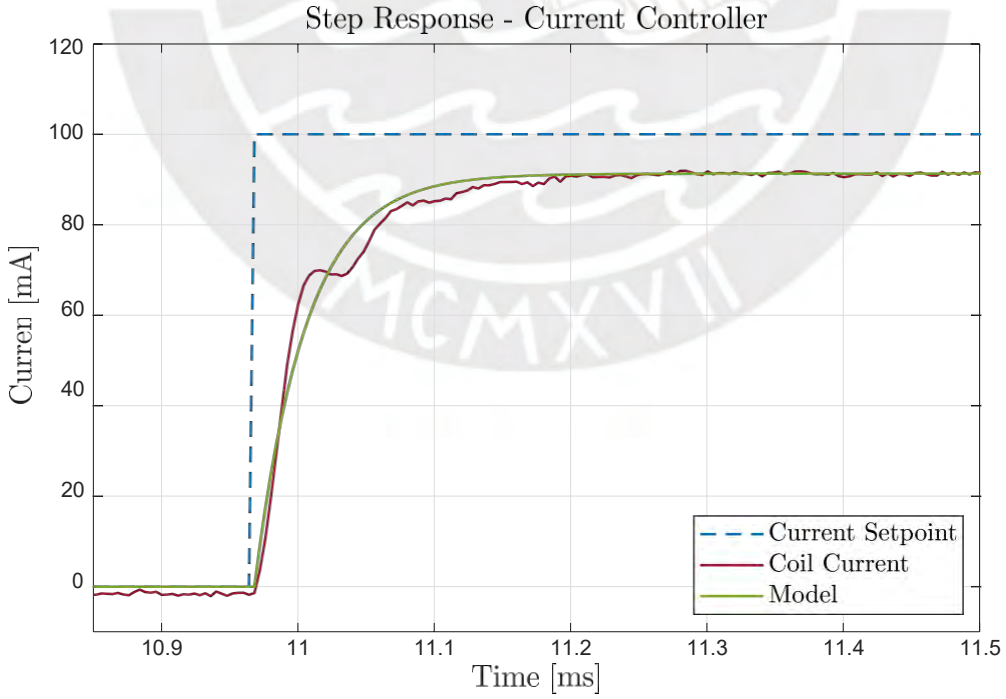

Figure 2.19: Step Response - Current.

$$G_{\text{current}}(s) = \frac{24159.045}{s + 26465.29}, \qquad \tau = 3.778 \times 10^{-5}, \; K_{\text{current}} = 0.91286 \tag{2.19}$$

$$BW \approx \frac{1}{2\pi\tau} = 4.2\,\text{kHz} \tag{2.20}$$

The voice coil drive bandwidth has a broader range than the pneumatic actuation. This means that the voice coil can produce a faster response force than its pneumatic counterpart. This property is useful to generate forces at different rates by allocating it to the appropriate actuator.

Although the fast force generation, the LAU position has a slower response due to the system inertia. Figure 2.20 shows the position change to a current step input of 100 mA. The response time rise is around 0.04 s, similar to the pressure timing. In conclusion, the actuating forces in the LAU can be generated at different rates, however, the position response is slower compared to the voice coil force.

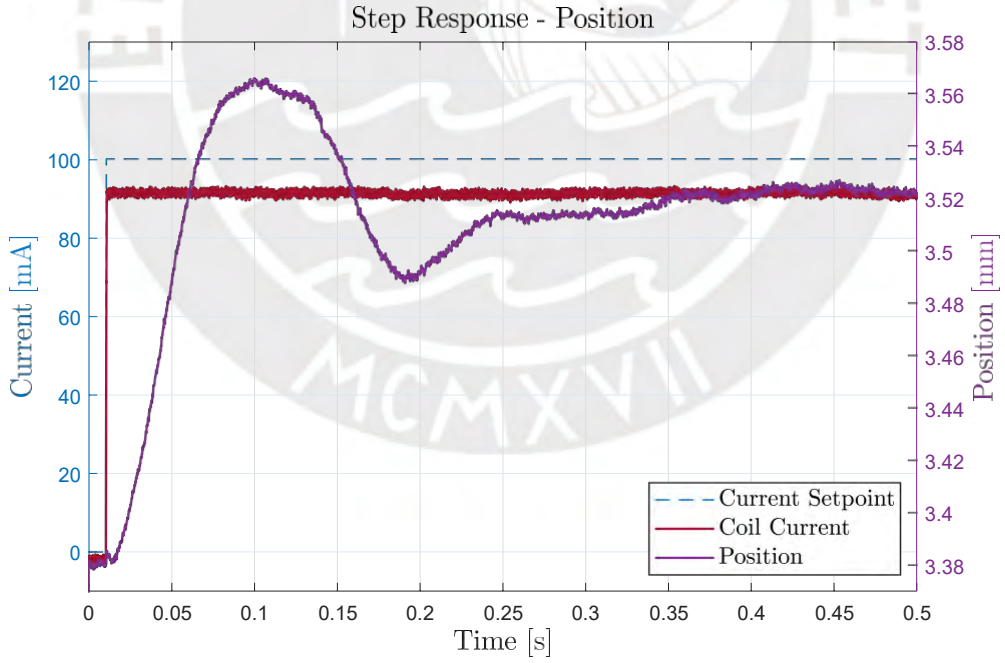

Figure 2.20: Step Response - Current to LAU position.

2.7 LAU Model

The LAU is a multiple input single output (MISO) system with nonlinear behavior (see Sections 2.3.2, 2.6.1). The inputs of the system are the pressure and current provided by the respective controller. While these controllers aim to track their respective setpoint, additional dynamics such as air dynamics, transmission delay and interaction with the LAU structure are intended to be included in their linear model approximation. In this manner, their overall dynamics are considered in the complete model.

Nevertheless, the model has an important level of model uncertainties and input disturbances. In Section 2.3.2, it is shown that the hysteretic behavior adds a strong nonlinear component. In the present work, the magnetic hysteresis is represented as an undetermined but bounded internal force. Instead of obtaining a model of the hysteresis loop, the average force value along the position (Equation (2.7)) is used. This approach introduces an uncertainty component F_h in the model, associated with the force difference with respect to the real magnetic force. In addition, the forces generated by the pressure and current are given by the Equations (2.22) and (2.24) respectively. Both are composed of the nominal force determined by actuator models and an additive input disturbance component.

$$F_{\text{pneumatic}} = p\,A, \qquad p = u_1 + d_p \tag{2.21}$$

$$= u_1\,A + F_{\text{d pneumatic}}, \qquad F_{\text{d pneumatic}} = d_p\,A \tag{2.22}$$

$$F_{\text{coil}} = K_{\text{motor}}(x)\,I, \qquad I = u_2 \tag{2.23}$$

$$= K_{\text{motor}}(x)\,u_2 + F_{\text{d current}}, \qquad F_{\text{d current}} = \Delta K_{\text{motor}}(x)\,u_2, \tag{2.24}$$

where $\Delta K_{\text{motor}}(x)$ is the difference with respect to the real motor parameter at position x; d_p is the pressure difference with respect to its setpoint, including the pressure disturbance; and $F_{\text{d pneumatic}}$, $F_{\text{d current}}$ are the pneumatic and current force disturbance, respectively. Note that the output from the actuator models has to be scaled to Pa and A, respectively.

In conjunction with the previous approximations, the difference respect to the real force applied to the LAU is defined as a bounded disturbance force F_d,

$$F_d = F_h + F_{\text{d pneumatic}} + F_{\text{d current}}. \tag{2.25}$$

The dynamics can be described by a second order nonlinear model in a mass-spring-damper scheme. The damping coefficient can be estimated from the position response using standard identification methods. For this purpose, a random square signal excites the system and the responses of the model and LAU are compared. The determined damping factor C_{damp} is $27.365\,\text{N}\,\text{s}\,\text{m}^{-1}$.

Finally, the actuator dynamics are included

$$u_1(s) = G_{\text{pneumatic}}(s)\,\bar{u}_1(s) \tag{2.26}$$

$$u_2(s) = G_{\text{current}}(s)\,\bar{u}_2(s), \tag{2.27}$$

where $\bar{u}_1(s)$, $\bar{u}_2(s)$ are their setpoints; $u_1(s)$, $u_2(s)$, $\bar{u}_1(s)$ and $\bar{u}_2(s)$ are the Laplace transform of $u_1(t)$, $u_2(t)$, $\bar{u}_1(t)$ and $\bar{u}_2(t)$, respectively.

The LAU dynamic model consists of the following differential equations based on the sum of forces

$$\begin{aligned} \dot{x}_1 &= x_2 \\ \dot{x}_2 &= \frac{1}{m}\Big[F_{\text{pneumatic}}(u_1) + F_{\text{coil}}(x_1, u_2) \\ &\qquad - F_{\text{weight}} - F_{\text{magnetic}}(x_1) - F_{\text{damping}}(x_2) + F_{\text{d}}\Big], \end{aligned} \tag{2.28}$$

with the position x_1 [m], velocity x_2 [$\text{m}\,\text{s}^{-1}$] and the input pressure u_1 [Pa] and current u_2 [A]. The model parameters are listed in Table 2.1.

Table 2.1: Model Parameters

Parameter	Description
Gravitational acceleration (g)	$9.81\,\text{m}\,\text{s}^{-2}$
Mass to be lifted (m)	1.3174 kg
Chamber cross section area (A)	$3.1466 \times 10^{-4}\,\text{m}^2$
LAU damping Factor (C_{damp})	$27.365\,\text{N}\,\text{s}\,\text{m}^{-1}$
F_{weight}	$m\,g$
$F_{\text{damping}}(x_2)$	$C_{\text{damp}}\,x_2$
$F_{\text{pneumatic}}(u_1)$	$A\,u_1$
$F_{\text{coil}}(x_1, u_2)$	$K_{\text{motor}}(x_1)\,u_2$
$F_{\text{magnetic}}(x_1)$	see Equation (2.7)
$K_{\text{motor}}(x_1)$	see Equation (2.15)
F_{d}	disturbance as undetermined bounded force

The model is implemented in Simulink, with $F_d = 0$, and compared with the data measurements from the LAU in open loop as shown in Figure 2.21 . The dSPACE framework provides a combination of setpoints to the controller inputs: only random pressure (Figure 2.22), constant pressure with random current (Figure 2.23) and a square wave combination of both inputs (Figure 2.24). Then, the position response is compared with the model simulation under the same input.

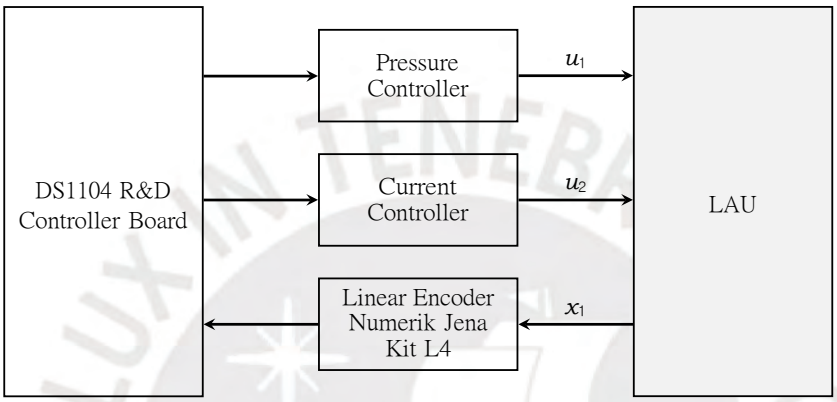

Figure 2.21: Test overall diagram

We can observe that the model accuracy depends on the actuator, operation point and input history. Since the magnetic force caused by the hysteresis is approximated to its average curve, the force error leads to a position difference in the stationary points. Furthermore, the coil operation generates a magnetic flux that can alter the shaft magnetization and change the magnetic force. Even more these effects, the model transient response is similar to real data with a model fit up to 93.82 % [1], which is acceptable for our work objectives.

As mentioned in Section 2.6.2, the current controller dynamics are faster than the pressure. The current model (see Equation (2.19)) has a pole located at -2646 in the $s-$plane. Its pressure counterpart (see Equation (2.16)) has complex conjugate poles at $-58.3200 \pm 74.8346i$. In comparison with the pressure and LAU dynamics, the influence of the current controller dynamics is negligible. Hence, it can be considered instantaneous and we resort to a static gain factor K_{current} in Equation (2.19).

[1] Determined with support of Matlab System Identification toolbox.

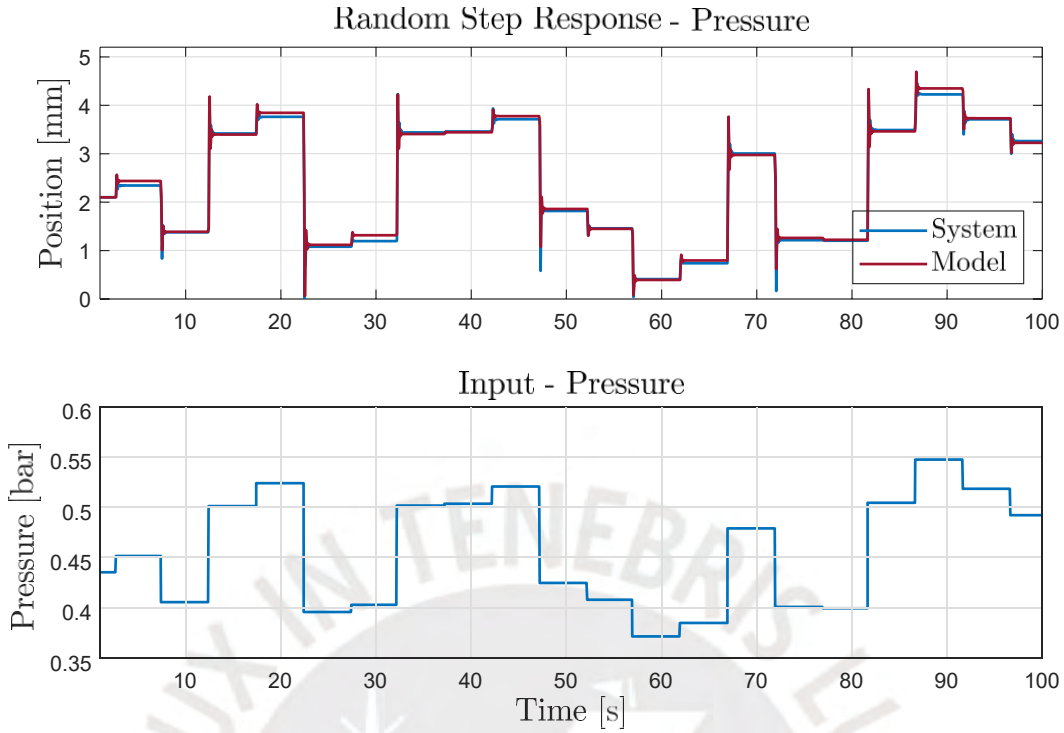

Figure 2.22: Comparison Random Pressure - Constant Current 0 mA

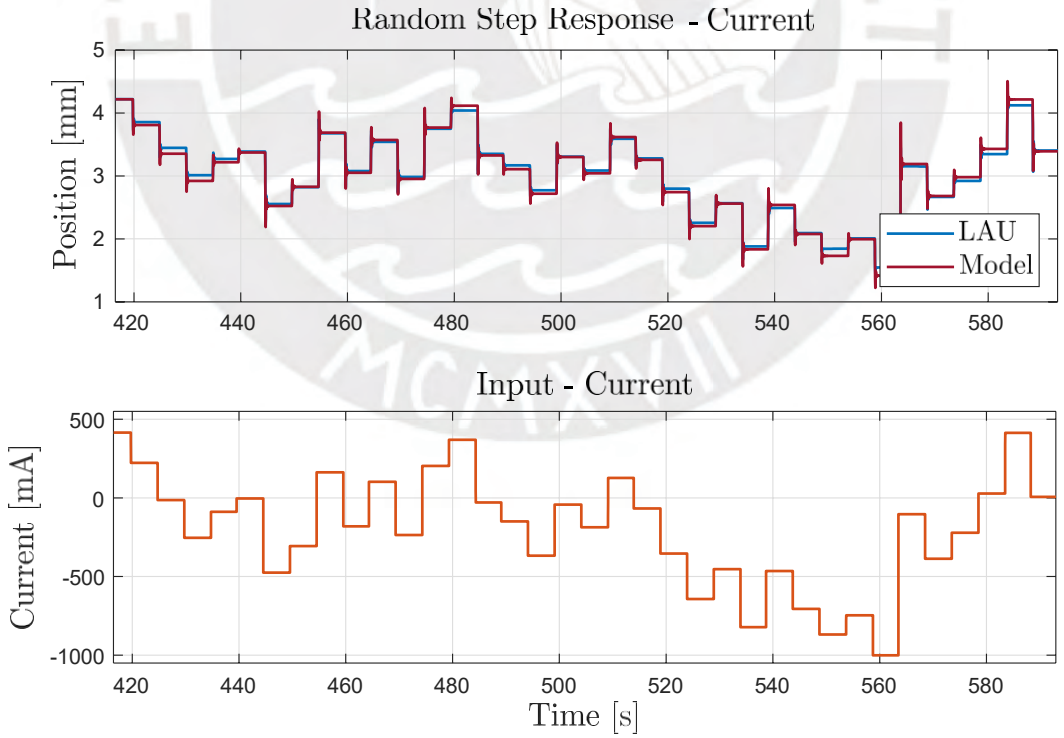

Figure 2.23: Comparison Random Current - Constant Pressure 0.5 bar & random current

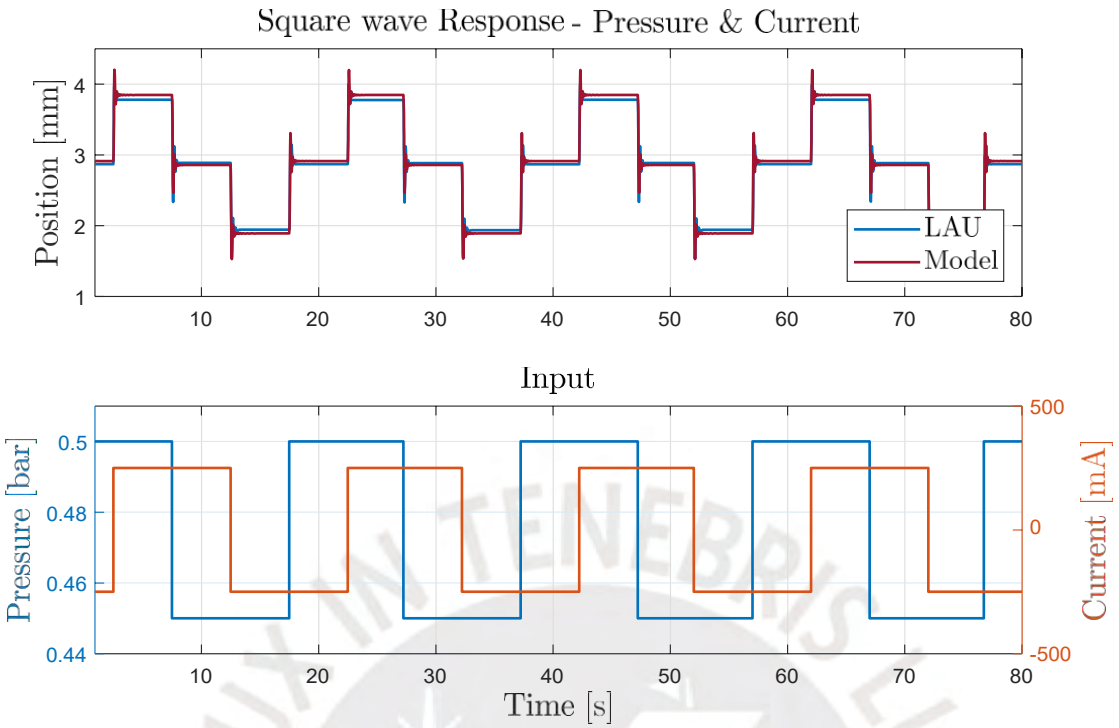

Figure 2.24: Comparison - Square Pressure & Current inputs

Linearization

Given the stationary operation point x_R with constant input u_R for the nonlinear system [30] [31]

$$\dot{x} = f(x, u) \tag{2.29}$$

where $f: D \rightarrow \mathrm{R}^n$ is a continuously differentiable function and $D \subset \mathrm{R}^n$ is a neighborhood of the point (x_R, u_R) where $f(x_R, u_R) = 0$. The linearized system about x_R, u_R is given by

$$\Delta\dot{x} = A\Delta x + B\Delta u \tag{2.30}$$

for sufficient small deviations $\Delta x = x - x_R$, $\Delta u = u - u_R$ with

$$A = \left.\frac{\partial f(x,u)}{\partial x}\right|_{\substack{x=x_R \\ u=u_R}} \tag{2.31}$$

$$B = \left.\frac{\partial f(x,u)}{\partial u}\right|_{\substack{x=x_R \\ u=u_R}}, \tag{2.32}$$

where the jacobian A is the state matrix and B is the input matrix.

The state space representation of the linearized nominal LAU system, i.e. no disturbances and uncertainties considered, can be expressed as

$$\begin{bmatrix} \dot{x}_{\text{LAU}} \\ \dot{x}_{\text{pneu}} \end{bmatrix} = \begin{bmatrix} A_{\text{LAU}} & B_{\text{s}} \\ 0 & A_{\text{pneu}} \end{bmatrix} \begin{bmatrix} x_{\text{LAU}} \\ x_{\text{pneu}} \end{bmatrix} + \begin{bmatrix} 0 & B_{\text{LAU}} \\ B_{\text{pneu}} & 0 \end{bmatrix} u \tag{2.33}$$

with $x = [x_{\text{LAU}}^{\text{T}} \; x_{\text{pneu}}^{\text{T}}]^{\text{T}} \in \text{R}^{\text{n}}$, $n = 4$, as the state vector and the input $u = [u_1 \; u_2]^{\text{T}} \in \text{R}^{\text{m}}$, $m = 2$, with u_1 in bar and u_2 in mA. The matrices $A_{\text{LAU}} \in \text{R}^{2\times2}$, $B_{\text{LAU}} \in \text{R}^{2}$, $B_{\text{s}} \in \text{R}^{2\times2}$ are the linearized dynamics around $(x_{\text{R}}, u_{\text{R}})$ defined as

$$A_{\text{LAU}} = \begin{bmatrix} 0 & 1 \\ \frac{\text{d}K_{\text{motor}}(x_{mm})}{\text{d}x_{mm}} K_{\text{current}} u_2 - \frac{\text{d}F_{\text{magnetic}}(\quad)}{\text{d}x_{mm}} \times 10^{3} & -\frac{c_{\text{damp}}}{\text{m}} \end{bmatrix}_{\substack{x_{mm}=x_R \\ u=u_R}} \tag{2.34}$$

where x_{mm} is the position in mm and the factor 10^3 results from the chain rule applied in the derivative of F_{magnetic}.

$$B_{\text{LAU}} = \begin{bmatrix} 0 \\ \frac{K_{\text{motor}}(x_{1\ mm}) K_{\text{current}} \times 10^{-3}}{\text{m}} \end{bmatrix}, \qquad B_{\text{s}} = \begin{bmatrix} 0 & 0 \\ \frac{A \times 10^{5}}{\text{m}} & 0 \end{bmatrix} \tag{2.35}$$

where the factors 10^{-3} and 10^5 correspond to the scale of the input u to A and Pa, respectively.

$$A_{\text{pneu}} = \begin{bmatrix} 0 & 1 \\ -9001.4 & -116.64 \end{bmatrix}, \qquad B_{\text{pneu}} = \begin{bmatrix} 0 \\ 9001.4 \end{bmatrix} \tag{2.36}$$

where the pair $(A_{\text{pneu}}, B_{\text{pneu}})$ is the state space representation of pressure controller dynamics given by Equation (2.16). Finally, 0 are zero matrices with appropriate dimensions.

ET LUX IN TENEBRIS LUCET
MCMXVII

3 Control Allocation

Actual applications in nanotechnology require positioning systems with nanometer scale precision over extended ranges. In this regard, multiple level actuators in series on a single axis are introduced to overcome this challenge. Dual-stage actuators (DSA) refer to systems that use two actuation sources. It is common that a low bandwidth primary stage positions the system in a large range. On the other side, the secondary actuator is capable of fine coarse with high precision and wide bandwidth. The combination of the two actuators increases the bandwidth, displacement range and precision of the system.

The controller design can take advantage of the multiple stage structure by driving the actuators according to their properties. Furthermore, the actuator redundancy in a single axis opens the possibility of achieving the desired position in several combinations of forces produced by the actuator set.

In this section, a control strategy with separate stages of regulation and distribution is evaluated. A control effort distribution scheme is presented with the objective to set a criterion to handle the actuator set.

3.1 Introduction

Over-actuated mechanical systems have two or more actuators that influence in the same degree of freedom. The challenge is the distribution of the control effort among the available actuation means in order to achieve the control objective. Control allocation (CA) was developed to redistribute the required force by the system between redundant actuators with constraints under a desired criterion. The general control structure is shown in Figure 3.1.

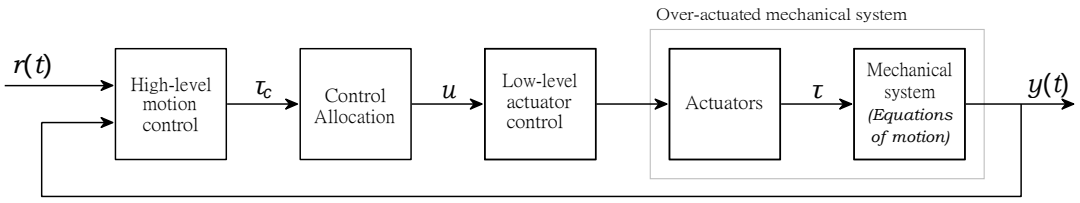

Figure 3.1: Control system diagram with control allocation [32].

Johansen *et al.* [32] describe control algorithms for over-actuated mechanical systems in three stages. A high-level motion controller determines the commanded virtual control efforts τ_c, i.e. the required force to meet the control objectives. That means that the virtual input τ should equal the required effort τ_c. It handles the system nonlinearities and guarantees the overall stability. The second stage focuses on the distribution of the desired forces between the actuators under specific criterion in a control allocation algorithm. These considerations may include actuator constraints, dynamic properties and power consumption of the actuators. Finally, the third stage consists of the low-level controller for each actuator. The modular control design presents several benefits [33].

- *Reduced motion controller complexity design*. The design of the high-level motion controller does not need to consider the detailed actuator knowledge or constraints. Since these characteristics are handled by the control allocation module, the motion controller design focuses on the total force requirement.

- *Facilitates Tuning*. In a single stage control method, the changes of control parameters, such as weights, not only modify the force distribution between actuators but alter the close loop behavior of the system. In theory, the closed loop dynamics are independent of the distribution of forces in CA approach.

- *Control allocation method exchange*. Since the closed loop dynamics are not affected by the force distribution algorithm, the control allocation method can be changed, in theory, without affecting the system behavior.

- *Actuator constraints*. The operational and physical actuator constraints can be taken into account in the control allocation stage. Restrictions such as input saturation, rate limits and power efficiency can be handled as secondary objectives in an optimization-based design. With this approach, the actuator capabilities are exploited and the system performance degradation, due to unfeasible control

commands, can be minimized.

- *Failure recovery*. In the event that an actuator is not available due to random failure, the control allocation algorithm will attempt to redistribute the required force between the remaining actuators under their own capabilities. Therefore, the failure is transparent to the high-level motion controller and instability can be avoided in the damaged system.

Problem Statement Following [33], consider a nonlinear input affine system of the form

$$\dot{x} = f(x) + B_u(x)\,u, \tag{3.1}$$

where $f(x) \in \mathrm{R}^n$, $B_u(x) \in \mathrm{R}^{n\times m}$ are nonlinear state-dependent functions, $x(\cdot) \in \mathrm{R}^n$ is the state vector and $u(\cdot) \in \mathrm{R}^m$ is the control input.

Under the scope of an over-actuated system, it is important to note that more than one actuator effects the force applied in the controlled degree of freedom. In essence, the following assumption has to be satisfied

Assumption 3.1.1 *$B_u(x)$ has rank $k < m$, i.e. $rank(B_u(x)) = k < m, \forall x \in \mathrm{R}^n$. That is, the matrix $B_u(x)$ is column rank deficient [34].*

Then, the input matrix $B_u(x)$ can be expressed as

$$B_u(x) = B_\tau(x)B(x), \tag{3.2}$$

where the matrix $B_\tau(x) \in \mathrm{R}^{n\times k}$ and $B(x) \in \mathrm{R}^{k\times m}$ both have rank k. In other words, the subspace spanned by the columns of $B_u(x)$ has the set of columns of $B_\tau(s)$ as basis. Therefore, the system (3.1) can be expressed as

$$\dot{x} = f(x) + B_\tau(x)\tau \tag{3.3}$$

$$\tau = B(x)\,u, \tag{3.4}$$

where $\tau \in A \in \mathrm{R}^k$ is the total force applied in each degree of freedom after the actuators dynamics and A is the attainable set of virtual commands.

Note that the system controllability requires that the number of virtual inputs τ to be at least the same as the number of degrees of freedom to be controlled [32].

Equation (3.4) represents the so called *effector model* that relates the total control effort τ with the system control input $u \in \mathrm{U}$, where U is the compact set of feasible inputs due to the actuator constraints such as

$$u \in \mathrm{U} := \{u \in \mathrm{R}^m | u^- \leq u \leq u^+\} \tag{3.5}$$

where $u^- := [u_1^-, u_2^-, \ldots, u_m^-]^T \in \mathrm{R}^m$, $u^+ := [u_1^+, u_2^+, \ldots, u_m^+]^T \in \mathrm{R}^m$ are the lower and upper actuators limit vectors and $u^- \leq u \leq u^+$ is an elementwise inequality, i.e. $u_i^- \leq u_i \leq u_i^+, i = 1, \ldots, m$.

Definition 3.1.1 *(Control Allocation Problem [32] [34]) The main objective is to determine the actuator input $u(t) \in \mathrm{R}^m$ that ensures that the commanded virtual control $\tau_c(t) \in \mathrm{R}^k$ is produced jointly by the actuators at all times t such as* (3.4) *and* (3.5) *are satisfied, leading to $\tau = \tau_c$.*

Assumption 3.1.2 *The actuator set is able to generate the commanded force τ_c from the high-level controller in at least one combination u within the actuator constrains* U.

As mentioned, there is actuator redundancy on the same system degree of freedom, that is $\dim(u) > \dim(\tau)$. This means there is a null space of dimension $m - k$ in which u can be altered while maintaining the same system dynamics. In consequence, there are several options to combine the actuators that result in the same total control effort.

The control allocation problem can lead to three different outcomes depending on the required control effort and the capability of the actuator set. Hence, it is possible that the control allocation problem has a unique, multiple or no solution [35]. In this sense, the required control effort τ_c may be obtained by a unique combination of the inputs taking into account the actuator constraints.

The second scenario considers that the set of actuators is not able to generate the desired total control effort due to actuator limitations or failure. This means that the Assumption 3.1.2 is not met. In this situation, the control allocation algorithm should provide the control input $u \in \mathrm{U}$ that minimizes the error $\tau_c - \tau$. In general, control

allocation is proposed as the optimization problem [32]

$$\begin{aligned} \min_{u} \quad & \|Q(\tau_c - B(x)u)\| \\ \text{subject to:} \quad & u \in \mathrm{U} \end{aligned} \tag{3.6}$$

where Q is a non-singular weighting matrix and $\|\cdot\|$ is some norm.

In case the control allocation problem has multiple solutions, secondary objectives can be met with lower priority in order to reach a unique solution. These may include diverse criteria such as minimization of the power consumption or actuator rates based on the input variation. In this sense, the Problem (3.6) is extended to a mixed optimization CA problem [36]

$$\begin{aligned} \min_{u} \quad & J(x, u, t) + \gamma\|Q(\tau_c - B(x)u)\| \\ \text{subject to:} \quad & u \in \mathrm{U} \end{aligned} \tag{3.7}$$

where γ is a scalar and $J(x, u, t)$ some secondary objective function.

The parameter γ balances the effort priority between the CA error and the secondary objective. A large magnitude of γ define the lower priority of $J(x, u, t)$. As γ tends to infinity, the problem (3.7) approximates to (3.6) [36]. An alternative representation is based on sequencial optimization process as presented in [37].

The solution to optimization-based control allocation problems depends on the formulation and complexity of the objective function and constraints. The distribution is usually determined by solving programming problems where computational power must be considered due to its implementation in real-time applications. Linear and quadratic objective functions with linear constraints are often preferred. Furthermore, certain methods allow explicit solutions for problems based on linear effector models. On the other side, complex formulations with nonlinear functions involve additional issues such as non-convex optimization problems, convergence to local minimums, a high number of iterations and computational complexities [32]. It is also worth noting that there are alternative CA methods not presented as optimal problem [38].

Despite the primary goal of control effort distribution under actuator constraints, some CA methods are capable to handle actuator failure. Since the CA algorithm is evaluated in each cycle, the force can be divided between the available actuators mapped in a distribution matrix leading to a fault tolerant system. Of course, additional

signals are needed to indicate the status of each actuator. Nevertheless, this function is not in the scope of the present work.

This section introduces the relevant control allocation methods for the work. Then, the proposed method to distribute the force in the LAU is presented.

3.2 Linear Control Allocation

Control allocation was mainly developed for the aeronautic industry, where aircrafts have several effectors able to generate moments in different axis. It was later extended to different vessels and to the automotive industry. In such systems, the dynamics of the actuators are negligible with respect to the motion dynamics. Then, following assumption is valid

Assumption 3.2.1 *The actuator set has an instantaneous response to the inputs or their dynamics are fast enough compared to the motion dynamics of the system* (3.1) *with a similar response time between each other. Then, the effectors are regarded as pure force generators.*

It should be noted that there are overactuated systems that do not present the actuator redundancy in the format required by Assumption 3.1.1. Such systems often include additional dynamic components at the input ports. These system models may be reformulated based on the Assumption 3.2.1. That is, neglecting the dynamics of the actuators and the input effects in some states [33]. As an alternative, a compensation technique may apply under a dynamic control allocation approach.

Definition 3.2.1 *(Static Effector Model [32, 34])*

A static effector model represents the analytical relationship between the physical control inputs u and virtual control input τ such as

$$\tau = h(u, x, t) \tag{3.8}$$

where $h : \mathrm{R}^m \times \mathrm{R}^n \times \mathrm{R} \rightarrow \mathrm{R}^k$ is a function, $u \in \mathrm{U} \subset \mathrm{R}^m$ is the control input to the actuators and $\tau \in \mathrm{R}^k$ is the virtual input vector that represents the total control effort.

Under the input affine system (3.1) and the time invariant case, the Equation (3.8) can be expressed as

$$\tau = h(u, x) = B(x)u \tag{3.9}$$

where $B(x) \in \mathrm{R}^{k \times m}$ is denominated the *control effectiveness matrix*.

Most control allocation methods are based on the underlying Assumption 3.2.1, hence they consider a static linear relationship between the actuators. Nevertheless, the effector matrix can change in each iteration since the CA algorithm is executed every cycle. Then, the time variant case is included in a sense. Following, some CA methods based on the described effectiveness matrix are presented.

Redistributed Pseudo Inverse

The method provides an explicit solution to the constrained two-norm optimal CA problem (3.10) based on the pseudo inverse of the generally non-square effectiveness matrix $B(x)$ [35].

$$\begin{aligned} \min_{u} \quad & \frac{1}{2}(u+c)^{\mathrm{T}} W(u+c) \\ \text{subject to:} \quad & \tau_c = B(x)u, \end{aligned} \tag{3.10}$$

where $W \in \mathrm{R}^{m \times m}$ is a positive definite weighting matrix and $c(u)$ is an offset vector that propagates the off-nominal or saturated value of the actuators. If no actuator has fixed input, c is a zero vector. In case the limits of u are reached, c includes the limit value in the respective entry and the problem is solved again.

The solution, subjected to a static effector model $B(x)$, is given by

$$u = -c + B^{\dagger}(x)(\tau_c + B(x)c) \tag{3.11}$$

$$B^{\dagger}(x) = W^{-1}B(x)^{\mathrm{T}}(B(x)W^{-1}B(x)^{\mathrm{T}})^{-1}, \tag{3.12}$$

where $B^{\dagger}(x)$ is the weighted pseudo inverse of $B(x)$.

Under Assumption 3.1.2, the redistribution of τ_c among the inputs u is done through iteration of Equations (3.12) (3.11) until each actuator reach its maximum capacity. Alternatively, actuator saturation can be prevented if the components of the matrix W

tend to high values as u is closer to its limits.

An extended redistributed pseudoinverse is proposed by Kirchengast *et al.* [39], where selected components of the vector τ_c are prioritized over others. As a result, the error between the commanded and output control effort in those components is reduced in the event that the actuator set is not able to provide the complete desired effort.

This versatile method has multiple applications. A variation of the pseudo-inverse has been used in thrust allocation among the propellers of an offshore supply vessel [40] where the weight component is used to minimize the energy consumption. The Exact Redistributed Pseudoinverse method is proposed in [41] for the distribution of torque between the rudder deflections of an aircraft. A dynamic weighting approach applied in a spacecraft model is able to avoid the saturation of the effectors and reduce the energy required [42]. In [43], a pseudo inverse control allocation in combination with model predictive control (MPC) demonstrates that under faulty conditions the inclusion of restriction in the main controller improves the performance of the system.

Error Minimization

Control allocation problems are usually solved by an optimal control design technique that minimizes the difference between τ_c and τ subject to actuator constraints and secondary objectives. Note that the control algorithm has to be implemented in real-time applications, so computational power is a factor to take into account. Recursive optimal procedures may not converge in the time window available as they have high computational costs. In this sense, simpler but effective alternatives may suit the application requirements better.

The basic approach for error minimization problem 3.6 applying the norm-1 is formulated as a linear programming problem through a slack variable in [35].

Nevertheless, minimization methods are used to take advantage of the null dimension to establish secondary objectives. Quadratic programming problems have been solved to allocate the force to the actuators of vehicle wheels with crosswind disturbances [44]. The quadratic objective function weights the error of the commanded effort in each axis with the control input components.

An energy criterion is considered in the distribution of force in an omnicopter with 8 propellers as effectors [45]. The system has 6 DoF with 2 degrees of redundancy, where the cost function is based on the power of the propeller thrust with an error minimization component similar to the formulation 3.7. In [46], the energy optimization is based on the dual actuator efficiency properties rather than the input magnitude of the actuator. It is applied to an electric vehicle, where each independent wheel motor can also be used in generator mode.

The control effort distribution considers the actuator limits with responses at their maximum rate. This approach may be inconvenient when large and fast commands are required with effectors that evidence rate limit saturation. In consequence, the effort applied in the system is not the same as the required one. To overcome this situation, it is possible to include the actuator rate limits as a restriction in the optimization problem [35]. This is a way to consider the actuator bandwidth in the allocation stage. The actuator constraints are reformulated to consider the most restrictive case based on the maximum rate of change $\dot{u}_{\max}$ such as,

$$u^{+} = \min(u_{\max}, u + \Delta t\, \dot{u}_{\max}) \tag{3.13}$$

$$u^{-} = \max(u_{\min}, u - \Delta t\, \dot{u}_{\max}), \tag{3.14}$$

where Δt is the system sampling interval.

3.2.1 Relationship between CA to Linear Quadratic Regulator

In particular, the control design based on CA is equivalent to the optimal control method for a certain system class if the performance indexes are quadratic in the inputs. Härkegård [33] demonstrates that both methods offer equal design freedom with an equivalent control law based on an l_2 optimal controller for overactuated nonlinear systems under certain conditions. Furthermore, in the specific case of a linear system control allocation leads to an LQR controller. The key points with respect to the method parallel are mentioned as an LQR controller is used as a reference.

Design I Consider the nonlinear system (3.1), where u is determined by solving

$$\min_{u(\cdot)} \int_0^{\infty} [q(x) + u^{\mathrm{T}} R_{\mathrm{u}}(x) u]\, \mathrm{d}t \tag{3.15}$$

where $q(x) \geq 0$ and $R_u(x) = R_u(x)^T > 0$.

Design 2 Consider the nonlinear system (3.3), where τ is determined by solving

$$\min_{v(\cdot)} \int_0^{\infty} [q(x) + \tau^T R_\tau(x)\tau]\, dt \tag{3.16}$$

where $q(x) \geq 0$ and $R_\tau(x) = R_\tau(x)^T > 0$. The commanded control effort τ is distributed by solving

$$\min_{u(t)} \quad u^T W(x) u \tag{3.17}$$

$$\text{subject to:} \quad \tau = B(x)u \tag{3.18}$$

where $W(x) = W(x)^T > 0$.

Then, u is determined by

$$u = W(x)^{-1}B(x)^T \left[B(x)W(x)^{-1}B(x)^T\right]^{-1} \tau \tag{3.19}$$

Theorem 3.2.1 *([33]) The control laws generated by Design 1 and Design 2 are the same in the following two cases.*

- *If, for given R_u, the matrices R_τ and W are chosen as*

$$R_\tau(x) = \left[B(x)R_u(x)^{-1}B(x)^T\right]^{-1} \tag{3.20}$$

$$W(x) = R_u(x) \tag{3.21}$$

- *If, for given R_τ and W, the matrix R_u is chosen as*

$$R_u(x) = W(x) + B(x)^T \left[R_\tau(x) - B(x)W(x)^{-1}B(x)^T\right]^{-1} B(x) \tag{3.22}$$

In the case the system (3.1) is linear and the performance indexes of the states x are quadratic, then the l_2 optimal problems (3.15),(3.16) can be resolved under the scope of linear quadratic regulation (LQR).

Consider the linear system

$$\dot{x} = Ax + B_u u \tag{3.23}$$

$$B_u = B_\tau B \tag{3.24}$$

$$\tau = Bu, \tag{3.25}$$

where B_u, B_τ , B are constant matrices with the appropriate dimensions. An LQR controller can be designed under the following requirements [33]: the pairs (A, B_τ) and (A, B_u) are stabilizable ; the pair (A, Q) is detectable. Also, the cost function (3.15) is in the form $q(x) = x^T Qx$, $Q = Q^T \geq 0$ with the constant matrices R_τ, R_u and W.

Then, the Ricatti equation has a unique positive definite solution $P = P^T > 0$, such that

$$\tau = -R_\tau^{-1} B_\tau^T P x \tag{3.26}$$

stabilizes the system asymptotically.

The LQR conditions assure that the l_2 optimal solution holds globally, then it is possible to apply the Theorem 3.2.1 to transform the controller indistinctly between Design 1 and Design 2.

Even though CA and l_2 optimal solutions are equivalent under the mentioned conditions, the former allows the separation of the control design in motion and distribution stages. In this way, motion stage design focuses on the close loop dynamics while the distribution stage enhances the design through the inclusion of the force allocation among the actuators under input constraints. It should be noted that the classic LQR design does not consider the actuator set constraints. In this case, the control effort distribution is based on the appropriate weighting matrix to avoid actuator limits.

3.3 Dynamic Control Allocation

In the literature, Dynamic Control Allocation (DCA) refers to methods that include dynamics in their formulation. However, the term is also used in distribution methods that consider actuator dynamics in their structure [47].

Härkegård [37] propose an optimal problem to assign the control effort between the actuator with differentiated rates. For this purpose, a weighted component of the difference of control inputs is included in the objective function to penalize the actuator rates. The method uses the previous control inputs in the cost function rather to explicitly use a filter structure. However, it can be related to a linear filter in the actuator unsaturated case.

The concept of frequency allocation allows defining a distribution criterion in the frequency domain. Hence, it is possible to assign the actuator's operation range to specific sections of the frequency spectrum. It takes advantage of the diverse actuator bandwidths to distribute the commanded control effort τ_c according to the actuator capabilities. It is a direct approach where τ_c is filtered and assigned according to the actuator bandwidth.

Davidson *et al.* [48] propose to use a complementary low and high pass filter in each component of τ_c in order to separate frequency components. Then, the fast changing signal is redistributed through the pseudoinverse method between the available actuators capable to handle the signal bandwidth. A similar procedure is done with the low frequency component. The method is described by the following equations,

$$m_l(s) = L(s)\tau_c(s) \tag{3.27}$$

$$m_h(s) = [1 - L(s)]\tau_c(s), \tag{3.28}$$

where $m_l(s)$ and $m_h(s)$ are the low and high frequency of τ_c respectively, $L(s)$ is a diagonal matrix with a first order low pass filter for each degree degree of freedom expressed in τ_c

$$L(s) = \text{diag}\left[\frac{1}{T_1 s + 1}, \ldots, \frac{1}{T_k s + 1}\right] \tag{3.29}$$

with $T_1, \ldots, T_k$ are the actuators time constant.

The actuator limits are considered through two pseudo inverse, so the assigned input control signal are given by

$$u_l = B_p^{\dagger}(x) m_l \tag{3.30}$$

$$u_h = B_r^{\dagger}(x) m_h \tag{3.31}$$

$$u = u_l + u_h, \tag{3.32}$$

where $B^{\dagger}_{p}(x)$ and $B^{\dagger}_{r}(x)$ are the pseudo inverse 3.12 based on range and rate limits respectively.

The signal phase shift due to the filter stage does not affect the final force distribution. Since the signal complement in Equation (3.28) is used for the high frequencies, the total control effort before and after the filter is the same.

Actuator Dynamics Compensation

In systems with an actuator set whose dynamics have a severe effect on the rigid body to be controlled, the basic Assumption 3.2.1 does not longer hold and the effort produced by the actuators may differ from the commanded one. In consequence, the total force τ reflected in the system is different from the commanded τ_c. Thus, the idea of linear CA as a pure distribution stage is broken and introduces a sort of disturbance, such as delays or magnitude difference, even with a full operational actuator set. Since the high-level controller does not consider the actuator dynamics, these effects need to be considered in order to guarantee the overall stability [37, 49]

In this sense, DCA stage considers the effect that the actuators dynamics have on the output control effort. The objective is to maintain $\tau_c = \tau$ or at least minimize its difference.

In a compensation approach, the output of a static control allocation method, i.e. pseudo inverse, is post processed to counteract the actuator dynamics. In this way, the actuator inputs are overdriven so the actual force applied in the system is the same as the required by the main controller. Oppenheimer *et al.* [50] [49] demonstrate its feasibility for a linear first and second order dynamics through a factor introduced in the discrete response.

The actuator's dynamics, such as different time delays and rates, can define the strategy to follow. For instance, Kissai *et al.* [51] use an MPC (Model Predictive Control) method as an CA stage to overcome the time delay actuator difference. MPC is capable to solve an online optimization problem with states and input constraints over a prediction horizon. With the actuator's delay included in its formulation, it is possible to enable the right actuator with proper timing as the most effective systems reach their saturation limit. However, CA problems based on MPC requires a fair

knowledge of the actuator dynamics and enough computational power.

On the other side, Morani *et al.* [52] propose to include the effects of the actuator dynamics in a DCA based on a Kalman filter structure. The process model consists of the extended actuator model with a virtual input. Through a Kalman filter, the virtual input is estimated so the response of the actuator model approximates the required control effort. Furthermore, the input constraints are managed by a dynamic change of the states in case the limits are reached.

3.4 Proposed method

The objective of this work is to apply the concepts of control allocation to the LAU system. Usually, CA is proposed as an optimization problem with effector constraints such as position and rate. As an alternative perspective, this approach is extended to consider a CA method based on the actuator dynamics. As a result, a dynamic control allocation scheme with frequency distribution and a Kalman filter compensation stage is proposed. The DCA structure is shown in Figure 3.2.

Figure 3.2: Proposed dynamic control allocation structure.

The LAU features studied in Section 2.6 allows defining the design criterion for this method. The design requirements include the minimization of the coil current, being the major heat source in the positioning system. Also, a compensation stage is needed since the pneumatic actuator dynamics are comparable to the LAU motion dynamics. In the following sections, the dynamic control allocation method is presented.

3.4.1 Rank Validation

The basic requirement for CA is the actuator redundancy in the system. As a dual stage system with one DoF, it is clear that the LAU satisfies this requirement in principle. However, the identified model (2.26)-(2.28) does not show the redundancy format expected in Assumption 3.1.1.

In particular, consider the case where the Assumption 3.2.1 is valid such as the actuator set is a pure force generator. Then, the model is simplified to Equation (2.28). In an input affine format the system is given by

$$\dot{x} = \begin{bmatrix} x_2 \\ \frac{1}{m}(-F_{\text{weight}} - F_{\text{magnetic}}(x_1) - F_{\text{damping}}(x_2) + F_{\text{d}}) \end{bmatrix} + \begin{bmatrix} 0 & 0 \\ \frac{1}{m} & \frac{1}{m} \end{bmatrix} \begin{bmatrix} u_1 \\ u_2 \end{bmatrix}, \tag{3.33}$$

where u_1 is the force generated by the pressure, $F_{\text{pneumatic}}$; and u_2 is the force generated by the current, F_{coil}.

Then, the input matrix $B_{\text{u}}(x)$ has rank 1 where the number of inputs is $m = 2$, i.e rank $B_{\text{u}}(x) < m$. Therefore, the system is column rank deficient. In consequence, it is possible to factorize $B_{\text{u}}(x)$ to obtain its base as in Equation (3.2)

$$B_{\text{u}}(x) = \begin{bmatrix} 0 \\ \frac{1}{m} \end{bmatrix} \begin{bmatrix} 1 & 1 \end{bmatrix}. \tag{3.34}$$

Therefore, the model (3.33) can be expressed as

$$\dot{x} = \begin{bmatrix} x_2 \\ \frac{1}{m}(-F_{\text{weight}} - F_{\text{magnetic}}(x_1) - F_{\text{damping}}(x_2) + F_{\text{d}}) \end{bmatrix} + \begin{bmatrix} 0 \\ \frac{1}{m} \end{bmatrix} \tau \tag{3.35}$$

$$\tau = \begin{bmatrix} 1 & 1 \end{bmatrix} u, \tag{3.36}$$

where $\tau \in \mathrm{R}$ is the total force applied to the system through the actuator set, $u \in \mathrm{R}^2$ is the physical actuator input vector. Equation 3.36 is referred to as the static effector model.

Assumption 3.2.1 is well founded in the case of the VCM actuator, whose response can be considered instantaneous. Nonetheless, the pressure dynamics are significant with respect to the LAU motion dynamics. For this reason, a later compensation stage is included in the proposed CA method (see Section 3.4.4).

In conclusion, it is possible to apply a CA scheme for the force distribution among actuators in the LAU system under the previous considerations.

3.4.2 Frequency Allocation

The LAU system is a dual stage system with a clear division of its acting forces. The key idea is to use the high density force of the pneumatic actuation as a passive gravity compensation while the VCM force handles the transient forces. For this purpose, frequency allocation takes advantage of the different bandwidths of the independent pressure and VCM actuators to distribute the applied force in the LAU.

It is intended that the low frequency component of the desired control effort τ_c is allocated to the pneumatic actuation. In this way, the pneumatic force ideally provides the total force required in the steady state with $x_2 = 0$. However, it has been identified that the pressure introduces a significant input disturbance to the system reflected as a force, which leads to a position variation.

On the other side, the higher bandwidth of the VCM enables the system to handle the fast transient and disturbances with higher frequency components of τ_c. This approach will also reduce the power consumption of the coil, reducing the heat emission that is an important disturbance factor in nanopositioning systems as discussed in Section 1.5.

In this sense, the frequency allocation method based on Davidson *et al.* [48] is used. The bandwidth difference from the pneumatic and VCM actuators sets the conditions for the division of the desired control effort in the frequency domain.

As analyzed in Section 2.6, the approximated process model of the pressure actuator has a bandwidth of 17.04 Hz. On the other side, the VCM bandwidth is 4.2 kHz that is significantly broader than its pneumatic counterpart.

With this division criterion, is possible to design a discrete low pass filter (LPF) in conjunction with a complementary structure given by

$$f_{c\,l}(z) = L(z)\tau_c(z) \tag{3.37}$$

$$f_{c\,h}(z) = [1 - L(z)]\tau_c(z), \tag{3.38}$$

where $f_{c\ l}$ is the low frequency sprectrum of τ_c in [N], $f_{c\ h}$ is the force with frequency complement of $f_{c\ l}$ in [N]; $f_{c\ l}(z), f_{c\ h}(z), \tau_c(z)$ are the $z-$transform of $f_{c\ l}(t), f_{c\ h}(t)$ and $\tau_c(t)$.

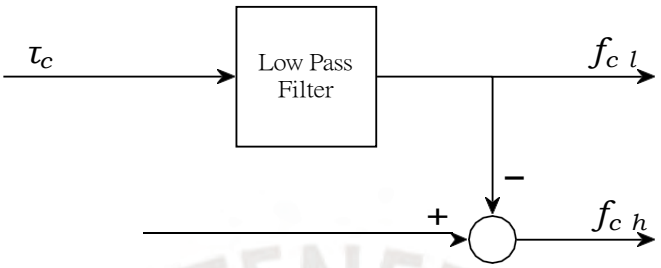

Figure 3.3: Frequency allocation structure.

The LPF output $f_{c\ l}$ feeds the pneumatic channel while the difference force $f_{c\ h}$ is provided by the VCM as shown in Figure 3.3. Any magnitude distortion in the LPF passband will be compensated by the VCM which is not desired in low frequencies. In this sense, a Butterworth filter is selected. It features a monotonic amplitude frequency response with a transition band that depends on its order.

The frequency allocation criterion in this application is defined such that the cutoff frequency of the LPF must be lower than the pressure bandwidth. Furthermore, the dynamics of the pressure actuation is not fully identified due to the intermediate pressure controller and pressure difference over the airline. In this sense, it is preferred to keep the pressure as constant as possible. In consequence, the cutoff frequency is set at 3 Hz with a filter order of 3 that leads to a shorter transition band with a decay of −60 dB per decade. The discrete filter is defined as

$$L(z) = \frac{8.356 \times 10^{-10} + 2.506 \times 10^{-9} z^{-1} + 2.506 \times 10^{-9} z^{-2} + 8.356 \times 10^{-10} z^{-3}}{1 - 2.996 z^{-1} + 2.992 z^{-2} - 0.996 z^{-3}} \tag{3.39}$$

and implemented in the system with a sample time of 0.1 ms. The frequency response of $L(z)$ is shown in Figure 3.4

Under the control allocation framework, it is important to note that the required force τ_c before and after the frequency allocation stage is the same due to its complementary structure. Hence, there is no force variation introduced in this stage.

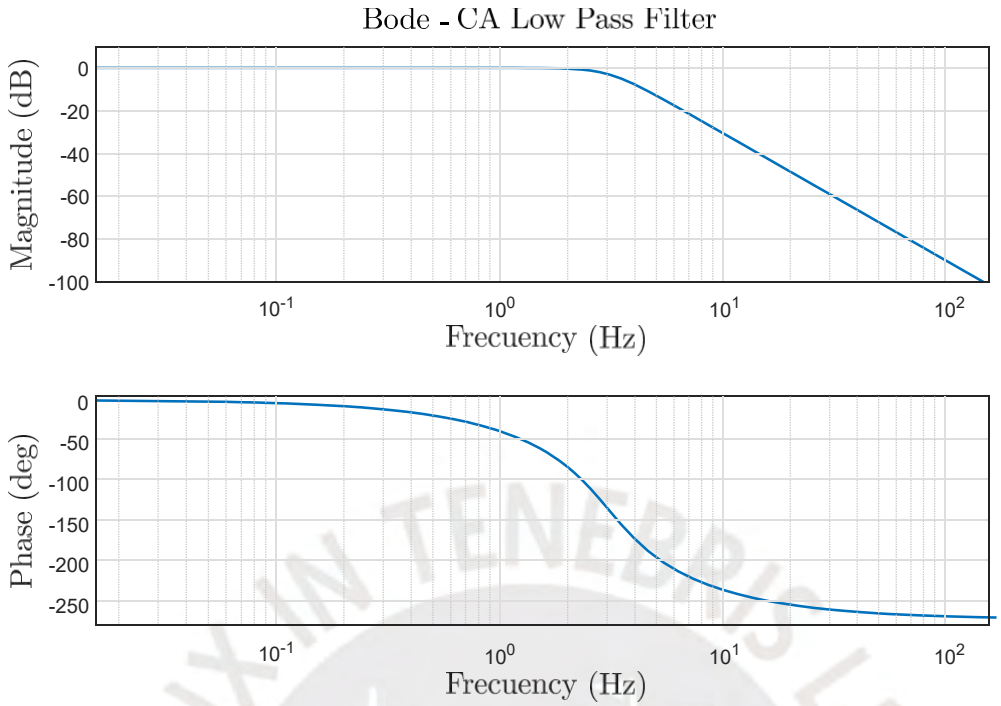

Figure 3.4: Frequency Allocation - LPF Frequency Response.

Furthermore, the previous distribution criterion allows disregarding actuator input constraints. As mentioned in Chapter 2, the pneumatic actuator is capable to lift the LAU top housing up to the maximum position by itself. It is possible to do it with a pressure higher than 0.62 bar of the 2 bar range. On the other side, the VCM does not produce enough force to move the LAU from the base without a pneumatic force offset. Hence, under the current implementation where the pneumatic force aims for a passive gravity compensation and the VCM only produces transient forces, the commanded inputs are always in the actuator input range, then no input constraints evaluation is required.

3.4.3 Transformation

The Frequency Allocation stage distributes τ_c in terms of forces assigned to each actuator. Nevertheless, the compensation stage includes the actuator model in terms of the manipulated variable. Therefore, an intermediate stage is needed to transform the assigned force into the commanded actuator manipulated variable u_c.

Under the conditions stated in Sections 2.4, 2.5 and with the parameters in Table 2.1, the transformation functions are expressed by

$$u_{\text{c pressure}}(k) = \frac{10^5}{A} f_{\text{c l}}(k) \tag{3.40}$$

$$u_{\text{c current}}(k) = \frac{10^3}{K_{\text{motor}}(x_1)} f_{\text{c h}}(k), \tag{3.41}$$

where $u_{\text{c pressure}}$ is the commanded pressure in [bar], $u_{\text{c current}}$ is the commanded current in [mA] and x_1 is the LAU position. Regarding Equation (3.41), the restriction $K_{\text{motor}}(x_1) > 0$ is guarantee as $x_1 \in [0, 10]$.

3.4.4 Kalman Filter based Compensation

The distributed forces cannot be input to the actuator controllers since the total force generated in the LAU will be different over time due to the non-negligible actuator dynamics (see Equation (2.16)). In consequence, the need for a compensation stage arises. In this work, we consider a Kalman Filter approach based on Morani *et al.* [52] to handle the compensation of the actuator dynamics and determine the control commands.

As an optimal estimator, the Kalman filter minimizes the error between the measured and estimated variable. In this sense, it is applied to reduce the difference between the desired u_c and the estimated actuator response u through the estimation of a virtual input x_u included in the state vector. It is given by

$$x_u(k+1) = x_u(k) + w_u, \tag{3.42}$$

where $x_u(k) \in \mathrm{R}$ is the virtual input to the actuator model and $w_u \sim (0, Q_u)$ is a Gaussian noise process with covariance Q_u .

The process model consists of an extended actuator dynamics state space representation. The additional state corresponds to the virtual input of the integrated actuator model. The discrete system model is given by

$$\begin{bmatrix} x_u(k+1) \\ x_{act}(k+1) \end{bmatrix} = \begin{bmatrix} I & 0 \\ \tilde{B} & \tilde{A} \end{bmatrix} \begin{bmatrix} x_u(k) \\ x_{act}(k) \end{bmatrix} + \begin{bmatrix} w_u \\ w_{act} \end{bmatrix} \tag{3.43}$$

$$y_{act}(k) = \begin{bmatrix} 0 & \tilde{C} \end{bmatrix} \begin{bmatrix} x(k) \\ x_{act}(k) \end{bmatrix},$$

where x_{act}, $\tilde{A}$, $\tilde{B}$ and $\tilde{C}$ of proper dimensions are the state vector, state matrix, input and output matrix, respectively, of the actuator linear dynamic representation. $w_{act} \sim (0, Q_{act})$, $w_u \sim (0, Q_u)$ are Gaussian noise processes. Finally, the system output y_{act} corresponds to the actuator model response.

Consider the measurement variable $z(k)$ as the desired input $u_c(k)$ determined by the previous CA stages such that

$$z(k) = u_c(k) + v(k) \tag{3.44}$$

with $v(k) \sim (0, R)$ as Gaussian noise with $R > 0$.

A Kalman filter implemented for the system (3.43) is able to estimate $x_u(k)$ such that it minimizes the error between the desired u_c and the *a apriori* estimated actuator model response $\hat{y}_{act}$. The procedure is described by the following equations

Prediction stage (*a priori*)

$$\hat{x}^-(k+1) = \tilde{A}\, x(k) \tag{3.45}$$

$$P^-(k+1) = A(k)\, P(k)\, A^T(k) + Q(k) \tag{3.46}$$

Correction stage (*a posteriori*)

$$K(k) = P^-(k)\, H^T(k) \quad H(k)\, P^-(k)\, H^T(k) + R(k)^{-1} \tag{3.47}$$

$$\hat{x}(k) = \hat{x}^-(k) + K(k) \quad z(k) - H\, \hat{x}^-(k) \tag{3.48}$$

$$P(k) = (I - K(k)\, H(k))\, P^-(k) \tag{3.49}$$

where $H = \begin{bmatrix} 0 & \tilde{C} \end{bmatrix}$ and

$$Q = \begin{bmatrix} Q_{\mathrm{u}} & 0 \\ 0 & Q_{\mathrm{act}} \end{bmatrix}. \tag{3.50}$$

Since the Kalman Filter is used as a minimization method, the noise covariance parameters are regarded as design parameters. The process $x_{\mathrm{u}}(k)$ considers the input variable with a constant first derivate, however, Q_{u} can be tuned to alter the process dynamics. The method relies on the actuator model dynamics; hence, Q_{act} tends to be smaller than Q_{u} so the actuator dynamics are preserved. In the same sense, R is recommended to be small to show high affinity to the desired command u_{c}.

Finally, the physical actuator input u is the estimated virtual input, such as

$$u = \begin{bmatrix} I & 0 \end{bmatrix} \hat{x}(k). \tag{3.51}$$

Although the objective of this technique is to reduce the error $u_{\mathrm{c}} - \hat{y}_{\mathrm{act}}$, it may not reach zero. This force difference can be considered as a disturbance in the system. Therefore, it is usual to combine DCA methods with a high-level motion controller based on adaptive or robust controllers that consider disturbances.

This method variance of Morani *et al.* [52] focuses on the compensation stage rather than the control effort allocation. From this perspective, u is determined based on the actuator dynamics while the allocation and input constraints, if applicable, are handled by the first stage.

Regarding the LAU application, it is worth noting the difference between the pneumatic and VCM actuator. The pneumatic actuator dynamics are similar to the LAU motion dynamics, while the VCM response is nearly instantaneous. In consequence, the Kalman filter compensation is applied to the pneumatic branch while the VCM is simplified to a static gain.

The process model for the pneumatic actuator compensation is based on the discrete version of the identified model in Section 2.6.1. Then, the process model 3.43 matrices are replaced with

$$\tilde{A} = \begin{bmatrix} 0.9999 & 9.9418 \times 10^{-5} \\ -0.8949 & 0.9884 \end{bmatrix} \tag{3.52}$$

$$\tilde{B} = \begin{bmatrix} 4.4832 \times 10^{-5} \\ 0.8949 \end{bmatrix} \tag{3.53}$$

$$\tilde{C} = \begin{bmatrix} 1 & 0 \end{bmatrix}. \tag{3.54}$$

The design parameters Q_{act}, Q_u, R are determined under the mentioned conditions and through experiments in the implemented LAU system.

$$Q_{act} = \begin{bmatrix} 10^{-5} & 0 \\ 0 & 1 \end{bmatrix} \tag{3.55}$$

$$Q_u = 1 \tag{3.56}$$

$$R = 10^{-3} \tag{3.57}$$

The input of the pneumatic actuator $u_{pressure}$ is the virtual input state estimated through the Kalman Filter. Then,

$$u_{pressure}(k) = \hat{x}_u(k) = \begin{bmatrix} 1 & 0 & 0 \end{bmatrix} \hat{x}(k). \tag{3.58}$$

The model that includes the dynamics of the VCM and the current controller is described by Equation (2.19). Since its response is much faster than the LAU motion dynamics, it is represented by the static gain $K_{current}$ in steady state condition. In order to compensate for the magnitude difference, the commanded input $u_{c\ current}$ is multiplied by the inverse. Then, the control input for the VCM is given by

$$u_{current}(k) = \frac{1}{K_{current}} u_{c\ current}(k) = u_{c\ current}(k)\, 1.0955. \tag{3.59}$$

Simulation Results

In this section, the proposed dynamic allocation structure response is reviewed. For this purpose, we consider the CA stage in open loop. This allows us to define the desired control effort τ_c and analyze its distribution between the actuators.

The overall response of the CA stage is presented in Figure 3.5. The ideal control effort τ_c is a square signal with additive noise as a disturbance. It supposes an extreme case not usual in real applications but permit us to demonstrate the power of the solution.

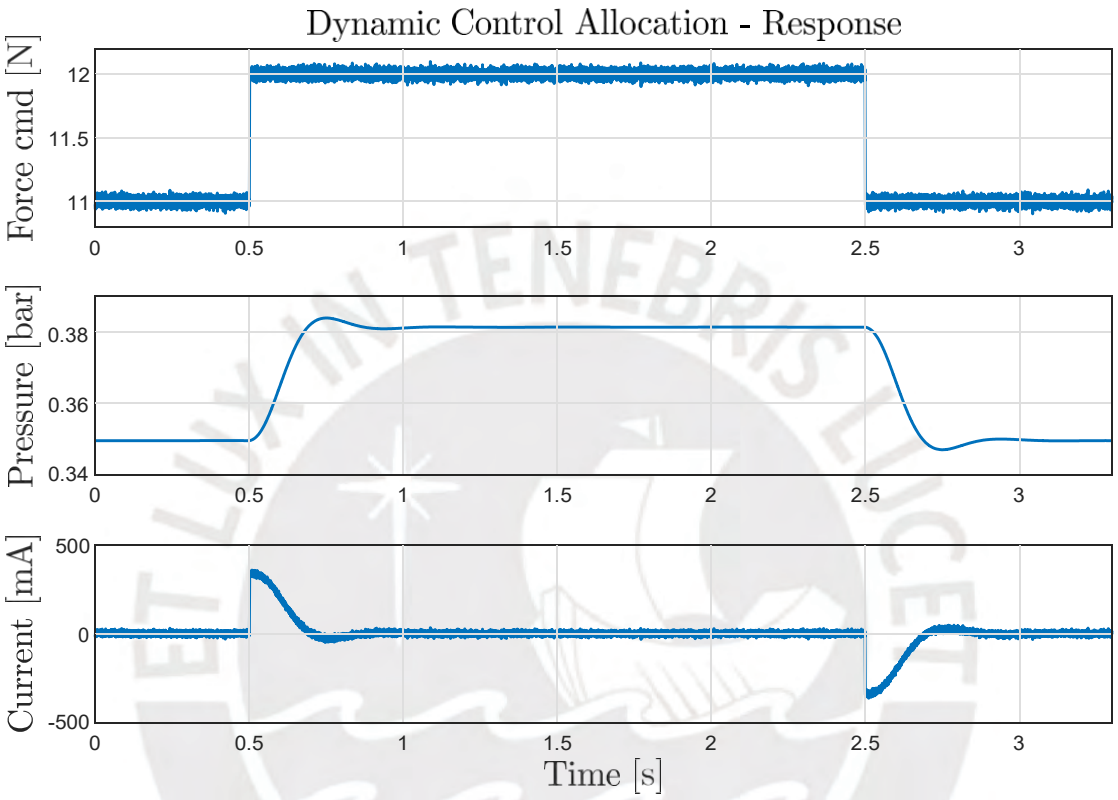

Figure 3.5: Dynamic Control Allocation - Step response.

The proposed method assigns the commanded control effort among the actuators. It determines the setpoint in the proper units for the low level controllers in each case. Due to the frequency allocation based on the pneumatic bandwidth criterion, the pressure input is determined within the actuator capabilities. On the other side, the transient and high frequency components of τ_c, such as the disturbance rejection, are allocated to the voice coil drive. Hence, the desired control effort is provided by both actuators according to their characteristics.

On top of that, the low power consumption requirement of the VCM is fulfilled. The VCM does not provide a constant force in steady state condition. Hence, the disturbance due to temperature increase is reduced.

The Kalman filter compensation determines the control input in case the actuator dynamics are significant with respect to the system motion dynamics. This is indeed the case, the pneumatic actuator and the LAU motion dynamics are comparable. As seen in Figure 3.6, the estimated input u compensates for the phase shift produced by the pneumatic actuator. In consequence, the error between the commanded pressure input u_c and the estimated pressure u_τ in the LAU is minimized. As a result, the effective control effort on the LAU tends to be similar to the determined by the frequency allocation stage.

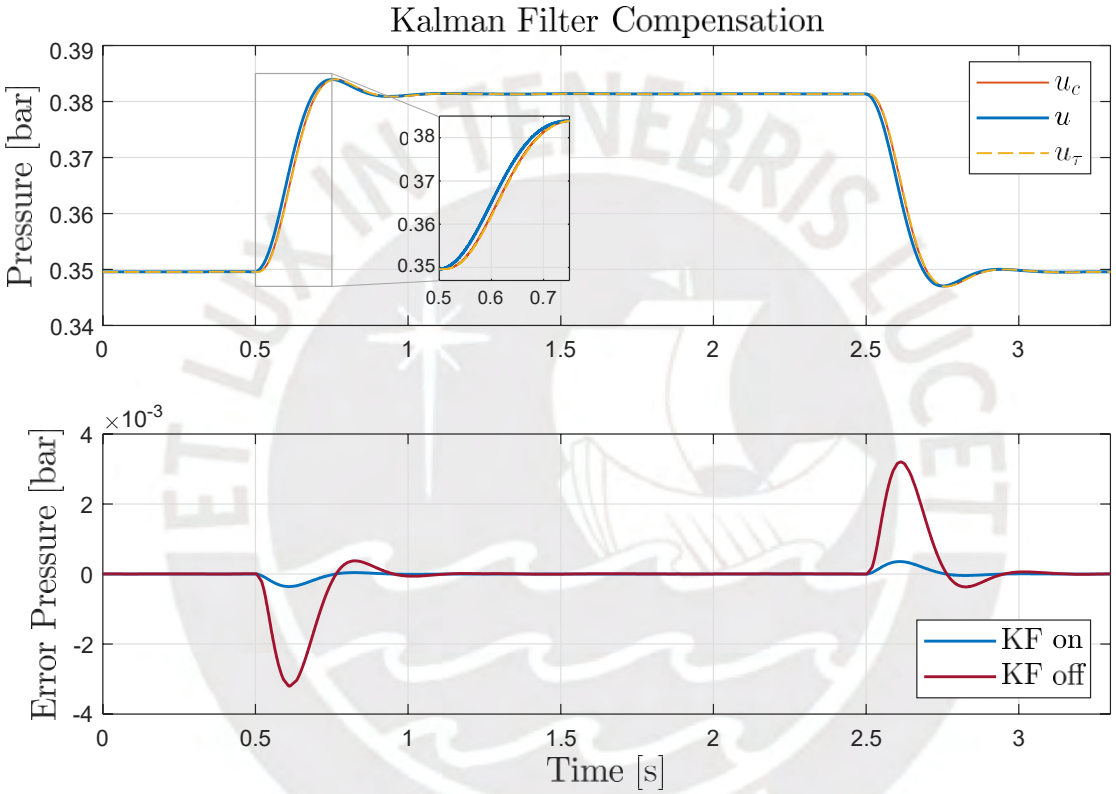

Figure 3.6: Kalman Filter Compensation - Pneumatic Actuation.

The second plot in Figure 3.6, shows the effect of the KF stage on the control effort difference. If the direct output from the transformation stage, Equations (3.40) and (3.41), is applied to the system without contemplating the actuator dynamic influence, the error between the commanded input u_c and the actual value u_τ in the LAU increases. In contrast, the KF stage actually reduces this error.

4 Control Structure

Control design for nanoposition systems usually deals with nonlinearities and noisy measurements. Actuator nonlinearities, such as creep and hysteresis presented in piezoelectric and ferromagnetic based actuators, difficult the control of these systems. Furthermore, unmodeled dynamics taken to simplify the control design or model uncertainties due to parameter variations, such as environmental effects, tend to affect the performance of the controller. Additional considerations arise in the digital implementation of the controller. The control algorithm must be capable to execute in real-time considering computational the limitations of the device. Also, sensor and quantization noise introduced in DAC/ADC components need to be taken into account. In this direction, nanoscale positioning demands a control strategy with high resolution, high bandwidth that is also stable against nonlinearities, uncertainties and noise. Hence robust, adaptive and learning techniques are often applied [53].

It is common to employ piezoelectric actuators due to their precision and high bandwidth. Nevertheless, its inherent hysteresis behavior needs to be considered in the controller design. In order to deal with this challenge, the control strategies can be categorized into two main branches depending on the characterization of hysteresis through a model or its consideration as an uncertainty. Specifically, the latter methods are of interest since it is the approach considered for the work in the LAU system.

4.1 Control Structure with Dynamic Control Allocation

The controller should be capable of controlling the vertical displacement of the LAU in the operating range with nanometer precision. Furthermore, the control allocation scheme should be applied. For this purpose, the system characteristics studied in Chapter 2 are taken into account.

Furthermore, a low power consumption of the voice coil actuator is required. For this reason, it is desired that the voice coil drive provides transient forces to prevent constant currents. As a complement, the pneumatic actuator is intended to work as a passive gravity compensation, i.e generate the overall force to lift the LAU in steady state condition.

The control design presents several challenges. The LAU architecture implementation uses proprietary controllers for pressure and current. This means that the dynamics of these components are undetermined and we rely on their capability to control the manipulated variables; nevertheless, approximated models describe their dominant behavior. The LAU operation is susceptible to heat, vibration and pressure disturbances. An important factor is the unmodeled hysteresis behavior of the internal magnetic force, which in conjunction with the disturbance, produces a major position variation in the μm range as discussed in Section 2.6.1.

The LAU position is a product of the applied control effort and the input disturbances. The idea is to counteract the uncertainties and disturbances estimated from the position measurement. In this direction, the proposed control structure considers a feedback linearization method with a disturbance observer for increased robustness in conjunction with the dynamic control allocation technique described in Section 3.4.The control diagram is shown in Figure 4.1.

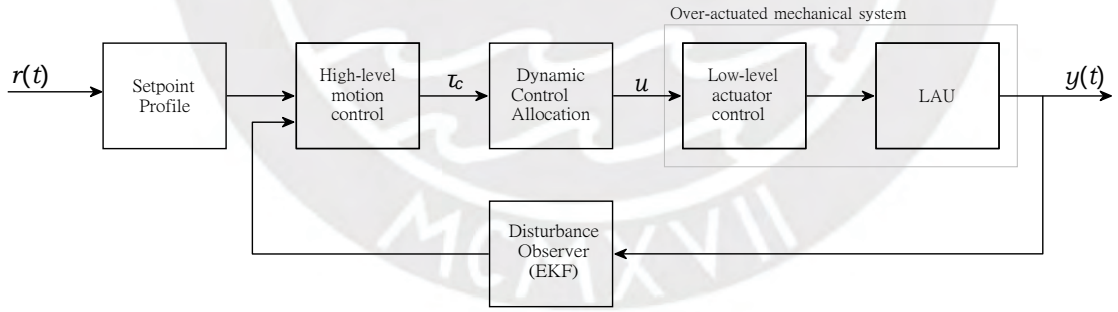

Figure 4.1: Proposed control structure for the LAU system.

An online trajectory shaping allows limiting the reference maximum speed to avoid measurement issues. The high level controller is designed under a feedback linearization approach. Hence, it is possible to use linear control techniques through a coordinate change and a compensation control law. The compensation allows separating the nonlinear components, uncertainties and disturbance effects from the linear control design. The disturbance observer estimates the unmodeled dynamics and disturbances

from the position measurements. The estimation seen as a disturbance force is used to cancel out its influence in the control effort. Finally, the dynamic control allocation stage distributes the force among the actuator set and compensates the actuator dynamics. The control structure is developed in the following sections.

4.2 Setpoint Profile

The LAU maximum speed displacement is limited by the hardware data throughput of the dSPACE interface. As determined in Section 2.1, the maximum travel speed is 1.977 mm s^{-1} to avoid counter issues in the dSPACE incremental encoder with the interferometer measurements.

It is of high importance to maintain the position measurement integrity through the LAU operation. Corrupted position data leads to position offsets with respect to the setpoint or even system instability. Therefore, the maximum speed $\dot{r}_{\max}$ is limited to 1 mm s^{-1} considering a security margin.

An alternative is to limit the speed of the reference r to reduce the required LAU displacement speed. In this direction, a setpoint filter with a speed saturation is considered. The speed saturation guarantees the maximum variation rate and set a trapezoidal profile to r. Subsequently, a first order low pass filter smooths the reference signal. The following equations describe the discrete procedure with the sample time $T_s = 1 \times 10^{-4}$ s.

$$q_{\max} = r(k-1) + \dot{r}_{\max} T_s \tag{4.1}$$

$$q_{\min} = r(k-1) - \dot{r}_{\max} T_s \tag{4.2}$$

$$q(k) = \begin{cases} q_{\max}, & r(k) \geq q_{\max} \\ q_{\min}, & r(k) \leq q_{\min} \\ r(k), & q_{\min} < r(k) < q_{\max} \end{cases} \tag{4.3}$$

where q is an auxiliary variable. The low pass filter is set to

$$r_0(z) = G(z)q(z), \qquad G(z) = \frac{0.0198}{z - 0.9801}, \tag{4.4}$$

with the chosen cutoff frequency $\omega_c = 200$ rad s^{-1} that corresponds to a bandwidth of 31.83 Hz, higher than the pneumatic actuator. The stage output is r_0.

This approach is suitable to move between operation points through step changes in r rather than reference tracking. The filter adds a phase shift and alters the magnitude as the reference reaches the cutoff frequency. The response to a 100 µm step is illustrated in Figure 4.2. The input is reshaped into a trapezoidal profile under the maximum speed permissible. The output r_0 presents the typical steady state error associated with a ramp input in a first order filter, that is finite and nonzero [29] . This effect is acceptable for the stage purpose.

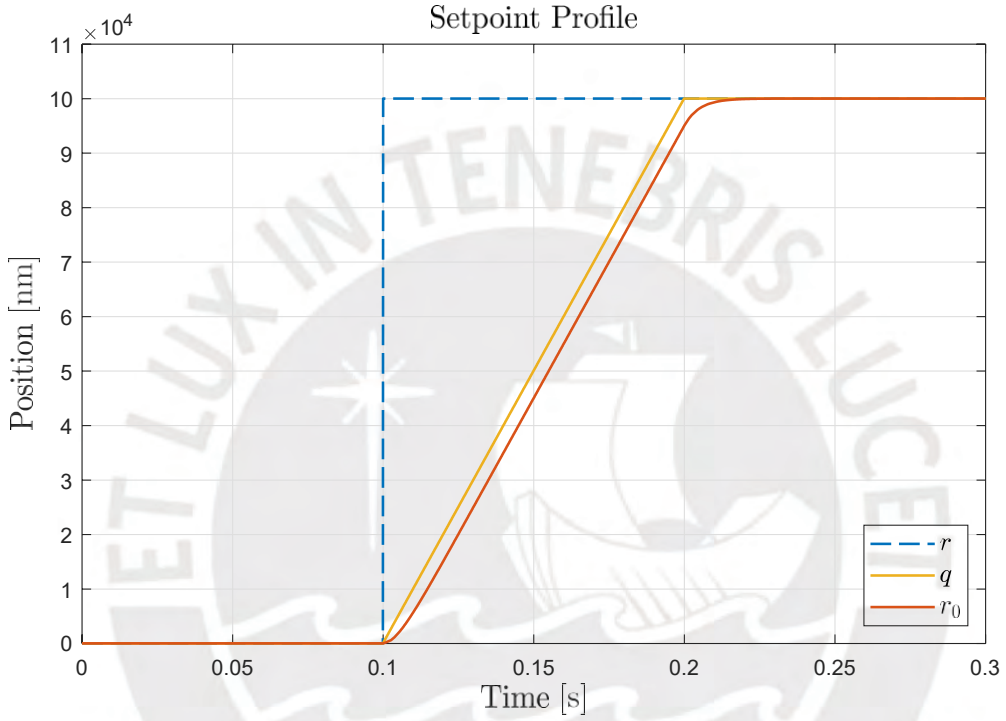

Figure 4.2: Setpoint Profile - Step response with limited speed.

4.3 Disturbance Observer

In the LAU system, the pressure presents a significant disturbance source that produces a position variation. The purpose is to estimate the disturbance in terms of the applied force into the LAU to counteract its effect on the system.

Consider the dynamic model [54]:

$$\dot{x} = Ax + Bu - \tau_d \tag{4.5}$$

$$\dot{x} = A_n x + B_n u - \tau_{dis}, \tag{4.6}$$

where $x \in \mathrm{R}^n$ is the state vector; A and $A_n \in \mathrm{R}^{n\times n}$ represent the uncertain and nominal states matrices, respectively; B and $B_n \in \mathrm{R}^n$ represent the uncertain and nominal control input vector; $u \in \mathrm{R}$ is the control input; $\tau_d \in \mathrm{R}^n$ represents the unknown plant dynamics and external disturbances; $\tau_{dis} \in \mathrm{R}^n$ represents the joint disturbance that includes the parameters uncertainties and τ_d. That is, $\tau_{dis} = (A_n - A)x + (B_n - B)u + \tau_d$.

Assume the disturbance model

$$\dot{x}_{dis} = A_{dis}\, x_{dis} \tag{4.7}$$

$$\tau_{dis} = C_{dis}\, x_{dis}, \tag{4.8}$$

where $A_{dis} \in \mathrm{R}^{m\times m}$ and C_{dis} are the state and output matrix of the disturbance model, respectively.

The disturbance dynamics are generally unknown; however, it is possible to estimate it based on a simple dynamic model under the disturbance observer (DOB) framework. The disturbance τ_{dis} can be estimated by an observer based on the augmented state space model of the nominal system

$$\begin{bmatrix} \dot{x} \\ \dot{x}_{dis} \end{bmatrix} = \begin{bmatrix} A_n & -C_{dis} \\ 0 & A_{dis} \end{bmatrix} \begin{bmatrix} x \\ x_{dis} \end{bmatrix} + \begin{bmatrix} B_n \\ 0 \end{bmatrix} u. \tag{4.9}$$

In this regard, a disturbance observer based on an Extended Kalman Filter (EKF) is proposed. Since the LAU dynamic model includes nonlinear functions, mainly due to the hysteretic force, an EKF suits the requirement to estimate the model states through linearization. The process model consists of the LAU dynamics extended with a noise model. The EKF estimates the force required to minimize the error difference within the estimated position and the interferometer measurement. In addition, it estimates the LAU speed required for a control feedback law.

The LAU model has notable uncertainties as the magnetic force is not determined through a hysteresis model. Therefore, the estimated disturbance force consists of the model uncertainties and pressure disturbance represented as forces.

4.3.1 Extended Kalman Filter (EKF)

The Extended Kalman Filter (EKF) is a recursive method capable to estimate the states $\hat{x}(k)$ of a nonlinear system based on inputs $u(k-1)$ and disturbed measurements $z(k)$. The uncertain states $x(k)$ are regarded as stochastic variables modeled by its probability distribution function $\mathrm{N}(\hat{x}(k), P(k))$, where the covariance $P(k)$ correspond to its *mean squared error* (MSE). The objective of the Kalman filter is to estimate $\hat{x}(k)$ that minimizes the MSE with respect to the observation $z(k)$ [55].

The dynamic behavior of the system relates the states in two consecutive time steps k and $k+1$. It is governed by the discrete stochastic nonlinear equation

$$x(k+1) = f(x(k), u(k)) + w(k), \tag{4.10}$$

where $x(k) \in \mathrm{R}^n$ is the state vector, $u(k) \in \mathrm{R}^m$ is a deterministic control input. The measurement $z(k) \in \mathrm{R}^p$ is given by the sensor model

$$z(k) = h(x(k)) + v(k). \tag{4.11}$$

The disturbances $w(k)$ and $v(k)$ are considered in terms of additive uncorrelated white noise processes with a zero mean Gaussian distribution. Their covariances are defined as $Q(k) = \mathrm{E}\langle w(k)w(k)^{\mathrm{T}} \rangle$ and $R(k) = \mathrm{E}\langle v(k)v(k)^{\mathrm{T}} \rangle$ respectively, where E is the expected value.

The EKF is able to deal with nonlinear systems through its linearization by the first order Taylor series expansions. The Jacobian or state matrix $A(k)$ evaluated at the estimated state $\hat{x}(k)$ is only used for solving the Riccati equation required for the Kalman gain K.

$$A(k) = \left.\frac{\partial f(x(k), u(k))}{\partial x(k)}\right|_{x(k)=\hat{x}(k)} \tag{4.12}$$

$$H(k) = \left.\frac{\partial h(x(k), u(k))}{\partial x(k)}\right|_{x(k)=\hat{x}(k)}. \tag{4.13}$$

The estimation $\hat{x}(k)$ is obtained after to processing the data in two stages. The prediction or *a priori* stage calculates the states at next time step based on the current system states. Note that the method still uses the nonlinear model (4.10) with the

unknown $w(k)$ as zero for the prediction.

$$\hat{x}^{-}(k+1) = f(\hat{x}(k), u(k)) \tag{4.14}$$

$$P^{-}(k+1) = A(k)P(k)A^{\mathrm{T}}(k) + Q(k). \tag{4.15}$$

In the second stage called correction or *a posteriori*, the estimation $\hat{x}^{-}(k)$ is updated based on actual measurements $z(k)$ and the error covariance is calculated.

$$K(k) = P^{-}(k)\,H^{\mathrm{T}}(k)\quad H(k)\,P^{-}(k)\,H^{\mathrm{T}}(k) + R(k)^{-1} \tag{4.16}$$

$$\hat{x}(k) = \hat{x}^{-}(k) + K(k)\ \ z(k) - H\,\hat{x}^{-}(k) \tag{4.17}$$

$$P(k) = (I - K(k)\,H(k))\,P^{-}(k). \tag{4.18}$$

Note that EKF is an attempt to include nonlinear dynamics under the linear Kalman filter scheme. This approach results in random variables that do not hold the assumed Gaussian distribution through the nonlinear transformations. In consequence, the distribution cannot be longer described only by the mean and covariance, leading to approximations of the exact linear Kalman Filter method.

In this sense, EKF is better applied on *quasilinear* systems where the errors due to linear approximation are tolerable compared to the model dynamic uncertainty [56].

4.3.2 Implementation

The disturbance observer is based on a process model that includes the LAU dynamics and a disturbance model. Consider the discrete linear process model

$$x(k+1) = A(k)\,x(k) + B(k)\,u(k) + w(k) \tag{4.19}$$

$$\begin{bmatrix} x_{\mathrm{LAU}}(k+1) \\ x_{\mathrm{d}}(k+1) \end{bmatrix} = \begin{bmatrix} A_{\mathrm{LAU}} & B_{\mathrm{d}} \\ 0 & A_{\mathrm{d}} \end{bmatrix} \begin{bmatrix} x_{\mathrm{LAU}}(k) \\ x_{\mathrm{d}}(k) \end{bmatrix} + \begin{bmatrix} B_{\mathrm{LAU}} \\ 0 \end{bmatrix} u_{\mathrm{act}}(k) + \begin{bmatrix} w_{\mathrm{LAU}} \\ w_{\mathrm{d}} \end{bmatrix}, \tag{4.20}$$

where $x_{\mathrm{LAU}}(k) \in \mathrm{R}^2$ is the LAU state vector, $x_{\mathrm{d}}(k) \in \mathrm{R}^2$ is the disturbance state vector, $u_{\mathrm{act}}(k) \in \mathrm{R}^2$ is the control input after the actuators, A_{LAU} and B_{LAU} are the state and input matrices of the LAU model, and w_{LAU}, w_{d} represent the zero mean Gaussian noise.

With the measurement

$$z(k) = h(x(k)) + v(k), \tag{4.21}$$

where $z(k)$ is interferometer position measurement and $v(k)$ is a zero mean Gaussian noise.

The overall LAU model can be represented as a four order model where the dynamics of motion and the pneumatic actuator are included. Note that the VCM dynamics are regarded as a static gain. Nevertheless, the proposed implementation of the EKF only considers the second order LAU motion dynamics due to dSPACE computational limitation. As an alternative, the pneumatic dynamics are included in a previous stage out of the EKF. Hence, the input u_{act} refers to the response of discrete dynamics of the actuator set to u, the control input after the dynamic allocation stage. The discrete transformation of the dynamics and input signal, with the sample time T_s = 0.1 ms, is given by

$$u(z)_{act} = \begin{bmatrix} G_{pneumatic}(z) & 0 \\ 0 & G_{current}(z) \end{bmatrix} u(z) \tag{4.22}$$

$$G_{pneumatic}(z) = \frac{4.4832 \times 10^{-5} z + 4.4658 \times 10^{-5}}{z^2 - 1.9883z + 0.9884} \tag{4.23}$$

$$G_{current}(z) = K_{current}, \tag{4.24}$$

where $u_{act}, u \in \mathrm{R}^2$.

The LAU nonlinear model can be considered *quasilinear* as the nonlinear components are modeled as a polynomial sufficiently differentiable, reducing the linearization error. Then, the LAU motion dynamics are linearized by

$$A_{LAU} = \frac{\partial f(x,u)}{\partial x} = \begin{bmatrix} 0 & 1 \\ \frac{dx_{mm}}{dK_{motor}(x_{mm})} u_2 - \frac{dx_{mm}}{dF_{magnetic}(x_{mm})} \times 10^3 \frac{1}{m} & \frac{-C_{damp}}{m} \end{bmatrix}_{x=\hat{x}(k)}^{k}, \tag{4.25}$$

where its matrix entries are evaluated in each cycle at the estimated operation point $\hat{x}(k), u(k)$.

The disturbance force is considered as a second order process given by

$$x_d(k+1) = A_d\, x_d(k) \tag{4.26}$$

$$A_d = \begin{bmatrix} 1 & 0 \\ 0 & 0 \end{bmatrix} \tag{4.27}$$

and the input matrix B_d as

$$B_d = \begin{bmatrix} 0 & 0 \\ \frac{1}{m} & 0 \end{bmatrix}. \tag{4.28}$$

Then, the continuous state matrix A_m is defined as

$$A_m = \begin{bmatrix} A_{LAU} & B_d \\ 0 & A_d \end{bmatrix}. \tag{4.29}$$

The process model A_m considers the LAU state variables in the meter range. For implementation purposes, the matrix A_m is scaled through the transformation T to the nanometer range. The scaled matrix A is given by

$$A = T\, A_m\, T^{-1} \tag{4.30}$$

$$T = \begin{bmatrix} 10^9 & 0 & 0 & 0 \\ 0 & 10^9 & 0 & 0 \\ 0 & 0 & 1 & 0 \\ 0 & 0 & 0 & 1 \end{bmatrix} \tag{4.31}$$

Then, the discrete model is approximated through the Euler method

$$A_k = e^{A\Delta t} \approx (I + A\, T_s), \tag{4.32}$$

where I is the identity matrix with dimensions of A.

In summary, the EKF is applied to a process model of order 4, i.e. $x(k) \in \mathrm{R}^4$ where $x_1(k)$ and $x_2(k)$ are the position and speed in the nanometer range, respectively; and $x_3(k)$ is the estimated disturbance force with $x_4(k)$ as its derivative.

According to the EKF procedure described by Equations (4.14)-(4.18), the *a priori* stage requires the discrete nonlinear model response and the process model (4.20) state matrix. The implementation of the discrete model response (4.14) is approximated using the forward Euler method with T_s as the sampling interval of the system [57] given by

$$\hat{x}^{-}(k+1) \approx \hat{x}(k) + f(x(k), u(k))\, T_s, \qquad T_s = 1 \times 10^{-4}\,\mathrm{s} \tag{4.33}$$

where $f(\cdot)$ is the LAU nonlinear model (2.26) - (2.28) that includes the actuator set dynamics.

In the current application, the weighting matrices Q and R are considered as design parameters. These matrices, tuned through experiments in the LAU system, are given by

$$Q = \mathrm{diag}(10^9, 10^{11}, 10^3, 10^2) \tag{4.34}$$

$$R = 10^{-3}. \tag{4.35}$$

The small magnitude in the input covariance implies that the LIF measurement has a small noise component. This makes sense under the scenario where the pressure disturbance has a higher effect in the LAU position than any disturbance or drift that affects the LIF measurements. The large magnitude weights assigned to the LAU states indicate a significant model uncertainty due to the hysteresis effect as well as the force variation due to the unmodeled pressure behavior. The weights related to the disturbance states have a considerable effect on the LAU position, as observed in the experiments, as they increase or decrease the disturbance compensation.

In conclusion, the DOB estimates the LAU motion states and the disturbance $\hat{F}_d = \begin{bmatrix} 0 & 0 & 1 & 0 \end{bmatrix} \hat{x}(k)$, which is used as compensation in the control law.

4.4 High Level Motion Controller

In conjunction with a control allocation approach, the high level motion controller handles the system nonlinearities as well as the main control objectives. It guarantees the system stability and should give certain robustness against disturbances.

An advantage of the CA approach is that the design of the motion controller is, in general, independent from the distribution of forces between the actuators and possible actuator failures. Hence, the distribution stage is transparent to the stability of the system.

As the control allocation stage is in charge of the force distribution, the LAU model is slightly modified from 2.28 to a virtual single input system that comprises the pneumatic and electromagnetic force. Therefore, the virtual input F_τ is given by

$$F_\tau = F_{\text{pneumatic}}(u_1) + F_{\text{coil}}(x_1, u_2). \tag{4.36}$$

Under the CA strategy, the high level controller is designed based on the motion dynamics of the plant neglecting the actuator dynamics. Then, system 2.28 can be expressed as

$$\begin{aligned} \dot{x}_1 &= x_2 \\ \dot{x}_2 &= \frac{1}{m}\left[F_\tau - F_{\text{weight}} - F_{\text{magnetic}}(x_1) - F_{\text{damping}}(x_2) + F_d\right]. \end{aligned} \tag{4.37}$$

This rearrangement leads to a single input single output system. The system is nonlinear due to the hysteresis behavior contained in $F_{\text{magnetic}}(x_1)$. The proposed method does not consider a hysteresis model for this force, hence it is considered as a bounded uncertainty as explained in Section 2.3.2. Furthermore, the system has an important disturbance input F_d due to the pressure required for the pneumatic actuation.

4.4.1 Feedback Linearization

Consider a class of nonlinear system given by

$$\dot{x} = f(x) + g(x)u \tag{4.38}$$

$$y = h(x), \tag{4.39}$$

where $x \in \mathrm{R}^n$, $u \in \mathrm{R}$, $y \in \mathrm{R}$ with f, g and h sufficiently smooth in a domain $D \subset \mathrm{R}^n$. The mappings $f, g : D \to \mathrm{R}^n$ are vector fields on D.

The relative degree r results from the successive derivation of y with respect the time until u emerges, that is

$$y^{(r)} = L_{\mathbf{f}}^{r} h(x) + L_g L_{\mathbf{f}}^{r-1} h(x)\, u \tag{4.40}$$

with $LgLf^{r-1} \neq 0$; where $L_f h(x)$ refers to the *Lie Derivative* of h with respect to f. The properties of the Lie Derivative can be found in [58].

Definition 4.4.1 *(Relative Degree [58]) The nonlinear system* (4.38)-(4.39) *is said to have relative degree* r, $1 \leq r \leq n$, *in a region* $D \subset \mathrm{R}^n$ *if*

1. $L_g L_{\mathbf{f}}^{i-1} h(x) = 0, \qquad i = 1, 2, \ldots, r-1$
2. $L_g L_{\mathbf{f}}^{r-1} h(x) \quad 0$

for all $x \in D$.

Since the system output is defined as position, Input - Output linearization applies. Nevertheless, is it possible to reach Exact Input Linearization under the condition $r = n$.

Lemma 4.4.1 *(Flat Output [59]) The Exact Linearization Problem is solvable if and only if there exist a neighborhood* D *of* x *and a real-valued function* $h(x)$, *defined on* x_0, *such that the system* (4.38)-(4.39) *has relative degree* $r = n$ *at* x.

Theorem 4.4.1 *(Transformation [58]) Consider the system* (4.38)-(4.39), *and suppose it has relative degree* $r = n$ *in* D. *Then for every* $x_0 \in \mathrm{R}^n$, *a neighborhood* D *of* x_0 *exist such that the map*

$$T(x) = \begin{matrix} h(x) \\ L_f h(x) \\ . \\ . \\ L_{\mathbf{f}}^{n-1} h(x) \end{matrix} \tag{4.41}$$

restricted to D, *is a diffeomorphism on* D.

Then is possible to expressed the system (4.38)-(4.39) in the new coordinates as

$$\begin{aligned} \dot{z}_1 &= z_2 \\ \dot{z}_2 &= z_3 \\ &\cdot \\ \dot{z}_{n-1} &= z_n \\ \dot{z}_n &= L_f^n h(x) + L_g L_f^{n-1} h(x)\, u. \end{aligned} \tag{4.42}$$

Now consider the external reference input v given by

$$v = L_f^n h(x) + L_g L_f^{n-1} h(x)\, u \tag{4.43}$$

$$u = a(x) + \beta(x) v \tag{4.44}$$

$$a(x) = -\frac{L_f^n h(x)}{L_g L_f^{n-1} h(x)} \tag{4.45}$$

$$\beta(x) = \frac{1}{L_g L_f^{n-1} h(x)} \tag{4.46}$$

Definition 4.4.2 *(Exact Input linearization [58]) A nonlinear system of the form* (4.38) *is said to be feedback linearizable (or input-state linearizable) if there exist a diffeomorphism* $T : D \to \mathrm{R}^n$ *such that* $D_x = T(D)$ *contains the origin and the change of variables* $z = T(x)$ *transforms the system 4.38 into the form*

$$\dot{z} = Az + Bv \tag{4.47}$$

$$v = \frac{1}{\beta(x)}(u - a(x)) \tag{4.48}$$

with (A, B) *controllable and* $\beta(x)$ *nonsingular for all* $x \in D$.

From Equation (4.48), the system is linearized through the state feedback control law

$$u = a(x) + \beta(x) v, \tag{4.49}$$

where v is the external reference input. As a result, the system is presented in the

Brunovsky form

$$\dot{z} = \begin{bmatrix} 0 & 1 & \dots & 0 \\ 0 & 0 & \ddots & \vdots \\ \vdots & \vdots & \ddots & 1 \\ 0 & 0 & \dots & 0 \end{bmatrix} z + \begin{bmatrix} 0 \\ \vdots \\ 0 \\ 1 \end{bmatrix} v \tag{4.50}$$

Implementation The system (4.37) can be expressed as

$$\dot{x} = \begin{bmatrix} x_2 \\ \frac{1}{m}(-F_{\text{weight}} - F_{\text{magnetic}}(x_1) - F_{\text{damping}}(x_2) + F_{\text{d}}) \end{bmatrix} + \begin{bmatrix} 0 \\ \frac{1}{m} \end{bmatrix} u \tag{4.51}$$

with $x \in \mathrm{R}^2$ and the position x_1 as output function

$$y = h(x) = x_1. \tag{4.52}$$

Assume a sufficiently smooth $F_{\text{magnetic}}(x_1)$ represented by its average value in Equation (2.7) and $F_{\text{d}} = 0$.

For notation clarity the components of $f(x)$ are defined as

$$f_1(x) = x_2 \tag{4.53}$$

$$f_2(x) = \frac{1}{m}(-F_{\text{weight}} - F_{\text{magnetic}}(x_1) - F_{\text{damping}}(x_2)) \tag{4.54}$$

The relative degree of the system (4.51)- (4.52) is determined by

$$\dot{y} = L_{\text{f}} h(x) + L_{\text{g}} h(x) u \tag{4.55}$$

$$L_{\text{f}} h(x) = \frac{\partial h}{\partial x} f(x) = (1\ 0) \begin{bmatrix} f_1(x) \\ f_2(x) \end{bmatrix} = x_2 \tag{4.56}$$

$$L_{\text{g}} h(x) = \frac{\partial h}{\partial x} g(x) = (1\ 0) \begin{bmatrix} 0 \\ \frac{1}{m} \end{bmatrix} = 0 \tag{4.57}$$

$$\ddot{y} = L_f^2 h(x) + L_g L_f h(x) u \tag{4.58}$$

$$L_f^2 h(x) = \frac{\partial L_f h(x)}{\partial x} f(x) = \begin{pmatrix} 0 & 1 \end{pmatrix} \begin{pmatrix} f_1(x) \\ f_2(x) \end{pmatrix} = f_2(x) \tag{4.59}$$

$$L_g L_f h(x) = \frac{\partial L_f h(x)}{\partial x} g(x) = \begin{pmatrix} 0 & 1 \end{pmatrix} \begin{pmatrix} 1 \\ \frac{1}{m} \end{pmatrix} = \frac{1}{m} \tag{4.60}$$

The relative degree of the SISO LAU system is $r = 2$, the same as the system order n. Hence, y is already a flat output of system (4.51). Therefore, transformation T (4.41) is reduced to the identity

$$z = T(x) = \begin{pmatrix} x_1 \\ x_2 \end{pmatrix}, \tag{4.61}$$

such that the system in the new coordinates is given by

$$\dot{z}_1 = z_2 \tag{4.62}$$

$$\dot{z}_2 = f_2(x) + \frac{1}{m} u. \tag{4.63}$$

Instead of using compensation law (4.48), we only apply a partial compensation alternative. The idea is to maintain the linear dynamics of the system (4.51) and only compensate for the nonlinear forces. In this case, the linear damping force remains. The alternative feedback law is given by

$$\beta(x) = m \tag{4.64}$$

$$\alpha(x) = -\left(-F_{\text{weight}} - F_{\text{magnetic}}(x_1)\right) \tag{4.65}$$

Then, the linear system is given by

$$\begin{aligned} \dot{z}_1 &= z_2 \\ \dot{z}_2 &= -\frac{C_{\text{damp}}}{m} z_2 + v \end{aligned} \tag{4.66}$$

Expressed in state space form

$$\begin{bmatrix} \dot{z}_1 \\ \dot{z}_2 \end{bmatrix} = \begin{bmatrix} 0 & 1 \\ 0 & \frac{-C_{damp}}{m} \end{bmatrix} \begin{bmatrix} z_1 \\ z_2 \end{bmatrix} + \begin{bmatrix} 0 \\ 1 \end{bmatrix} v. \tag{4.67}$$

As a result, the control law u with the compensation component and the estimated disturbance is given by

$$u = - \quad - F_{\text{weight}} - F_{\text{magnetic}}(x_1) + \hat{F}_{\text{d}} \quad + m\,v \tag{4.68}$$

The benefit of expression (4.68) is that it allows us to represent the uncertainties and disturbances in form of a joint force. This allows the disturbance estimation to cancel out these components.

4.4.2 Linear Controller

LQR with Integrator

Consider the continuous extended state space representation of the system (4.67)

$$\begin{bmatrix} \dot{z}_1 \\ \dot{z}_2 \\ \dot{z}_3 \end{bmatrix} = \begin{bmatrix} 0 & 1 & 0 \\ 0 & \frac{-C_{damp}}{m} & 0 \\ -1 & 0 & 0 \end{bmatrix} \begin{bmatrix} z_1 \\ z_2 \\ z_3 \end{bmatrix} + \begin{bmatrix} 0 \\ 1 \\ 0 \end{bmatrix} v + \begin{bmatrix} 0 \\ 0 \\ 1 \end{bmatrix} r_0, \tag{4.69}$$

where z_1, z_2 are the LAU position [m] and speed [m s^{-1}] respectively and z_3 is the error integration of z_1 and the internal position setpoint r_0.

The model is scaled to nm through the transformation T in order to avoid numerical issues.

$$T = \begin{bmatrix} 10^9 & 0 & 0 \\ 0 & 10^9 & 0 \\ 0 & 0 & 10^9 \end{bmatrix}, \tag{4.70}$$

where $T \in \mathrm{R}^{3\times3}$ is a nonsingular matrix and $T : \mathrm{R}^3 \to \mathrm{R}^3$. The scaled system is defined by $\bar{A} = TAT^{-1}$, $\bar{B} = TB$. The discrete version of the model is employed to design an

LQR with an integrator to eliminate stationary errors. The state and input weighting matrices, Q and R, are tuned through experiments in the LAU system.

$$Q = \begin{bmatrix} 0.5 & 0 & 0 \\ 0 & 5 & 0 \\ 0 & 0 & 500 \end{bmatrix} \tag{4.71}$$

$$R = 10^{15}. \tag{4.72}$$

The solution to discrete Riccati equation determines the LQR gains

$$K_{\text{LQR}} = \begin{bmatrix} 3.3158 \times 10^{-7} & 5.7100 \times 10^{-8} & -7.0511 \times 10^{-7} \end{bmatrix}. \tag{4.73}$$

The corresponding closed loop system eigenvalues in the $s-$plane are

$$\lambda = \begin{bmatrix} -2.1904 + 2.1902i \\ -2.1904 - 2.1902i \\ -73.6985 \end{bmatrix}. \tag{4.74}$$

Then, control law for the linear model is given by

$$v = -K_{\text{LQR}}\, z. \tag{4.75}$$

Finally, the control law under the feedback linearization scheme is updated to

$$u = -\left(-F_{\text{weight}} - F_{\text{magnetic}}(x_1) + \hat{F}_{\text{d}}\right) + m\left(-K_{\text{LQR}}\, \hat{x}_{\text{LAUi}}\right), \tag{4.76}$$

where $\hat{x}_{\text{LAUi}}$ are the estimated LAU states with the integrated position error as an additional state and $\hat{F}_{\text{d}}$ as the estimated disturbance force.

PI with Lead Compensation

As an alternative, a linear PI controller is tuned and tested. The robustness of the system is enhanced with a lead compensation that increases the margin phase.

Through the Laplace transformation, the system 4.67 can be expressed as a transfer function in the $s-$plane

$$G(s) = \frac{1}{s\left(s + \frac{C_{damp}}{m}\right)}. \tag{4.77}$$

The PI controller with lead compensation enhances the stability of the system as it increases the phase margin. A first order compensator adds a pole and zero, as shown in the following structure

$$C(s) = K_p + K_i \frac{1}{s} \left(\frac{aTs+1}{Ts+1}\right), \tag{4.78}$$

where K_i, K_p are the integral and proportional gains. T and $a > 1$ are design parameters of the lead compensation.

The controller parameters are selected such as the open loop dynamics $L(s)$ is dominated by the lead compensation dynamics. Therefore,

$$\begin{aligned} L(s) &= C(s)G(s) \\ &= \left(K_p + K_i \frac{1}{s}\right) \cdot \frac{1}{s\left(s + \frac{C_{damp}}{m}\right)} \cdot \left(\frac{aTs+1}{Ts+1}\right) \\ &= \frac{K_p}{s^2} \cdot \frac{s + \frac{K_i}{K_p}}{s + \frac{C_{damp}}{m}} \cdot \left(\frac{aTs+1}{Ts+1}\right) \end{aligned} \tag{4.79}$$

The idea is to cancel the system poles with the controller zero through

$$s + \frac{K_i}{K_p} = s + \frac{C_{damp}}{m} \tag{4.80}$$

$$K_i = \frac{C_{damp}}{m} K_p. \tag{4.81}$$

Without the compensation tranfer function, the dynamics of $L(s)$ has the dynamics of a double integrator. Then, the crossover frequency ω_s at 0 dB is determined by

$$\|L(s)\| = \left\| \frac{K_p}{s^2} \right\| = 1$$

with $s = j\omega$

$$\|L(j\omega)\| = \left\| \frac{K_p}{(j\omega)^2} \right\| = 1$$

$$K_p = \omega_s^2 \tag{4.82}$$

Then, the open loop dynamics is given by

$$L(s) = \frac{K_p}{s^2} \quad \frac{aTs+1}{Ts+1} \quad . \tag{4.83}$$

The LAU application requires a relatively slow response and a high phase margin to increase the overall robustness. Therefore, the parameters of the lead compensation are designed for low frequencies. After experimental validation, the parameters are defined as

$$K_p = 100, \qquad \omega_s = 10 \text{ rad s}^{-1} \tag{4.84}$$

$$K_i = 2.0772 \times 10^3 \tag{4.85}$$

$$\omega_p = \frac{1}{T} = 55, \qquad T = 0.01818 \tag{4.86}$$

$$\omega_x = \frac{1}{aT} = 4.5833, \qquad a = 12 \tag{4.87}$$

The frequency response of $L(s)$ is shown in Figure 4.3. The final phase margin is 56.8° at 20.9 rad s^{-1}.

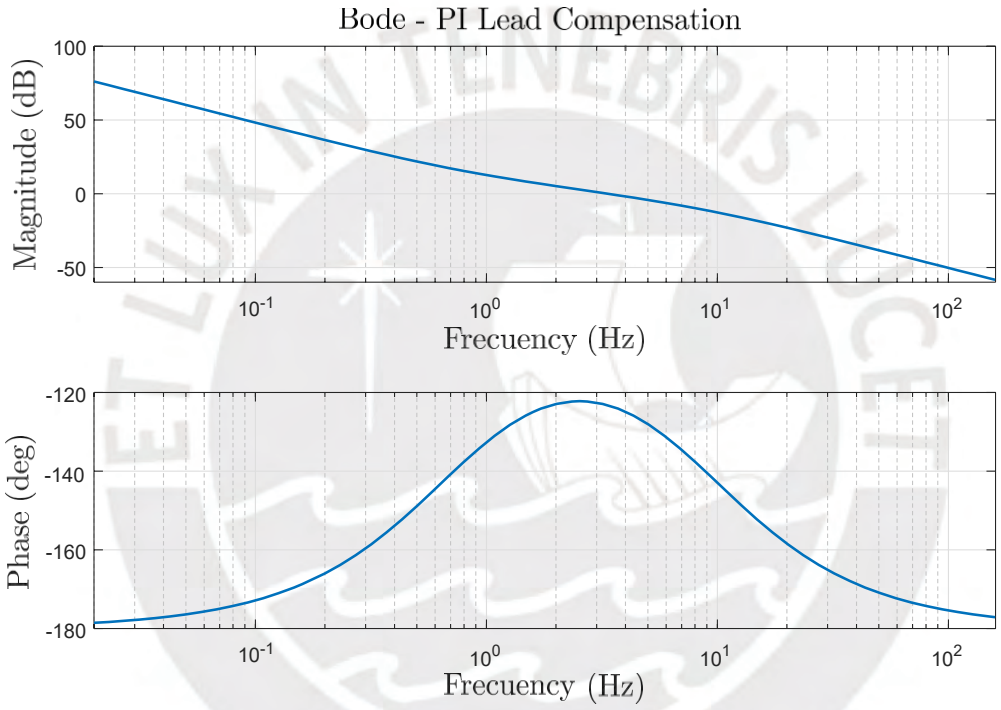

Figure 4.3: Frequency Response of close loop with PI Lead controller

5 Experimental Results

The following experiments are performed to prove the LAU system stability and review the control stages response. The LAU is designed as an actuator capable of displacement with nanometer precision in the millimeter range. Hence, it is of interest to review the system behavior on both scales.

The experiments are performed with the LAU testbench placed on top of an isolation table and protected with a plastic cover to reduce the effect of external disturbances such as vibrations and air drafts. The position measurements are done with the interferometer. In consequence, the maximum speed is limited to preserve data integrity. Consider that the system relies on the complete control structure with the PI with lead compensation (4.78) as a high level controller.

5.1 Millimeter Range

As a first approach, the step response in the millimeter range is presented in Figure 5.1. As expected, the control reference signal r is reshaped into a ramp, in order to slow down the system response. The LAU transient displacement shows an overshoot and oscillations not present in the reference r_0. This phenomenon is better observed in the position error in Figure 5.2. This behavior can be partially explained by unmodeled nonlinearities. However, the system does not display a position error in the millimeter range at steady state. The estimated speed is kept under the maximum limit as it can be seen in Figure 5.2. The maximum speed reached by the LAU is 1.4568 mm s^{-1} when the overshoot occurs. Hence, the indirect method to limit the speed is experimentally proven.

The behavior of the pneumatic actuator influences the performance of the LAU system since it is expected that it follows the pressure setpoint but also because it is considered

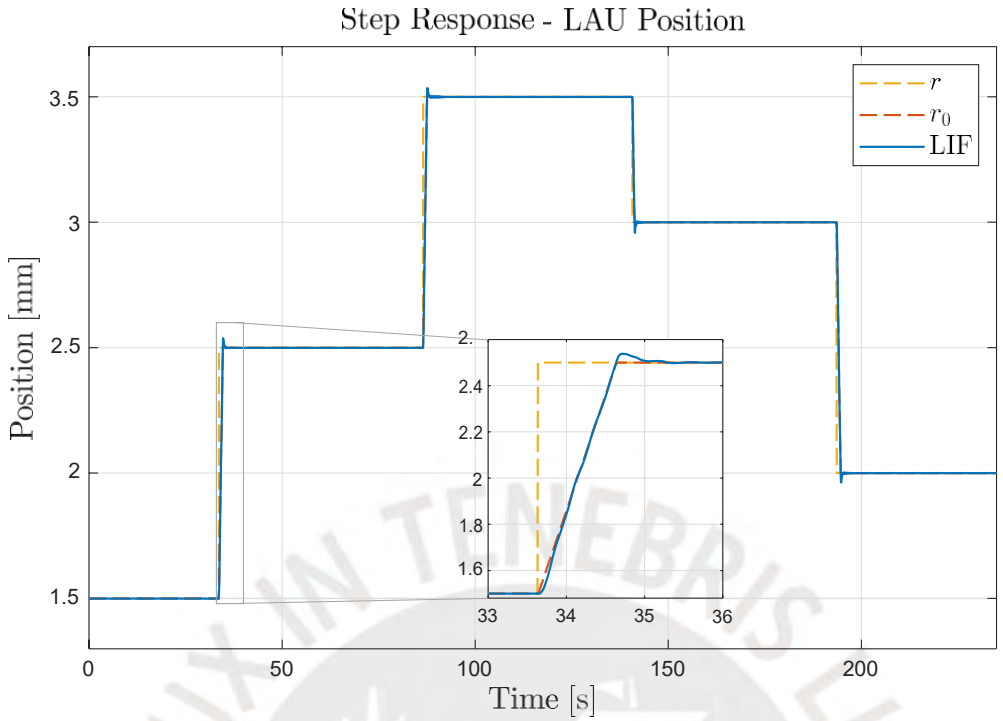

Figure 5.1: LAU system step response in the millimeter range

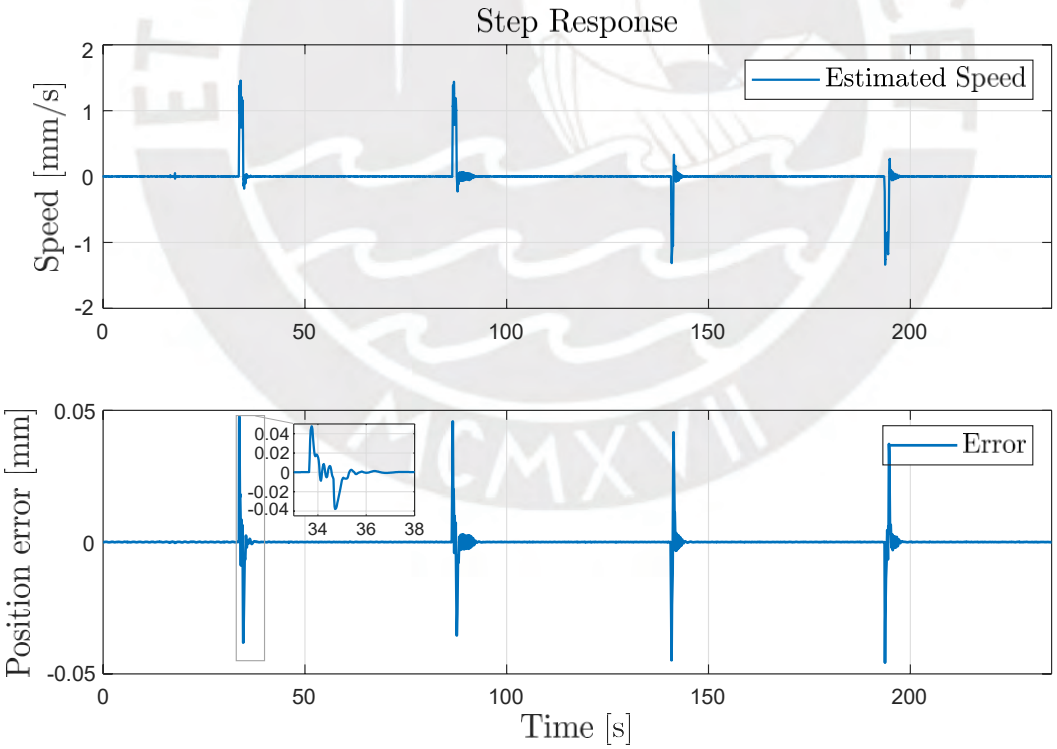

Figure 5.2: Step response - Speed and position Error in the millimeter range

a disturbance source. Figure 5.3 shows the measured pressure in the first position step. It compares the pressure at two different points of the air line with respect to the pressure setpoint u_{pressure}, which is the input to the AirCom pressure controller. The pressure near the controller is similar to u_{pressure} but it presents additional nonlinearities. The measured pressure indicates the presence of oscillations in the actuator response. The system seems to amplify to some extent the setpoint oscillations, as shown in the transient pressure. On the other side, the Digima sensor measures the pressure closer to the LAU. It shows a similar response but with pressure offset of 3 mbar. Then, if the measurements are accurate, the pressure inside the LAU chamber is higher than the commanded one. In conclusion, there are nonlinear effects in the pressure actuator which represents a disturbance force applied to the LAU.

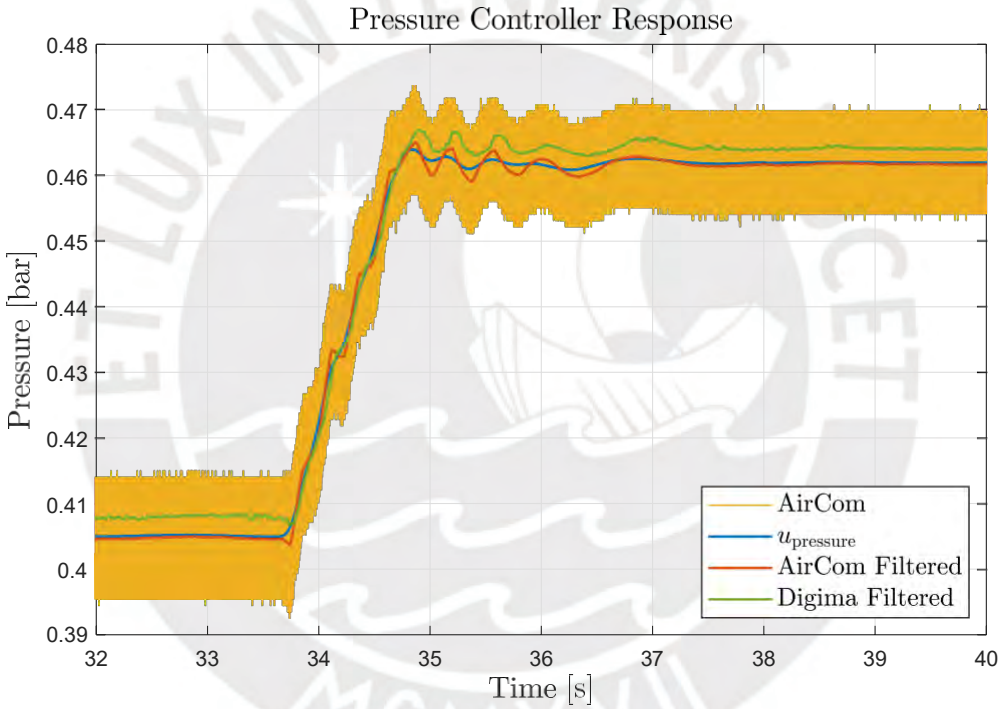

Figure 5.3: Pressure step response in the air line.

In this sense, the incorporation of the disturbance observer in the control structure is justified. As indicated in Section 4.3, the disturbance force includes the unmodeled dynamics of the system, parameters uncertainties and external disturbances. In this case, the estimated disturbance force for the step response is shown in Figure 5.4. The magnitude of the estimated force $\hat{F}_{\text{d}}$ changes as the LAU moves between steady operation points due to the LAU hysteresis behavior. It represents the magnetic force difference with respect to the calculated average value at the current position used in the disturbance observer model. In addition, the effect of unmodeled pressure dynamics

is also reflected as an oscillation component in the force.

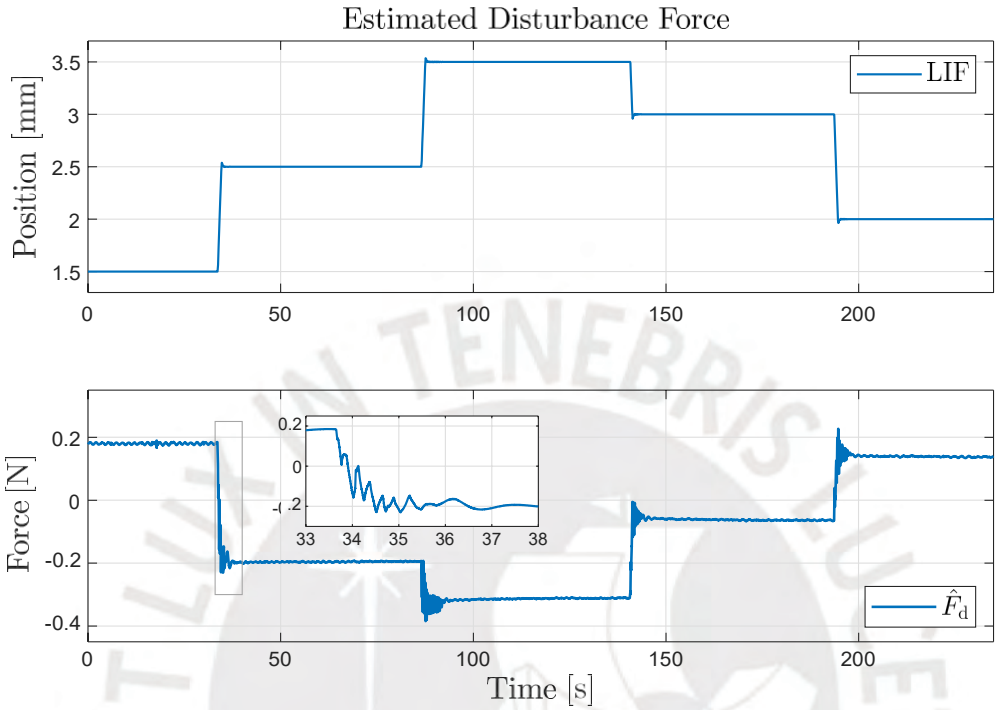

Figure 5.4: Estimated disturbance force in the millimeter range displacement.

Regarding the dynamic control allocation stage, the distribution of the commanded control effort τ_c among the actuators is shown in Figure 5.5. The frequency allocation effectively assigns the low frequencies of the required force, including the constant component, to the pressure actuator. This means that the pneumatic actuator acts as passive gravity compensation for the LAU weight and provides the additional slow varying forces. For instance, the pneumatic actuator produces 14.53 N with 0.4619 bar to lift the LAU to 2.5 mm. As a complement, the force difference, i.e. the high frequency component, is generated by the voice coil drive. Therefore, the voice coil motor handles the transient and fast varying forces. It does not generate any constant force, in consequence, the power consumed by the coil is reduced with a maximum of 17.762 mW (99.337 mA) in the first force peak in the referred case and requires an average of 1.3 µA at steady state. It is worth noting that the actuator forces are a result of the equivalent control input determined in the transformation and Kalman filter compensation stages.

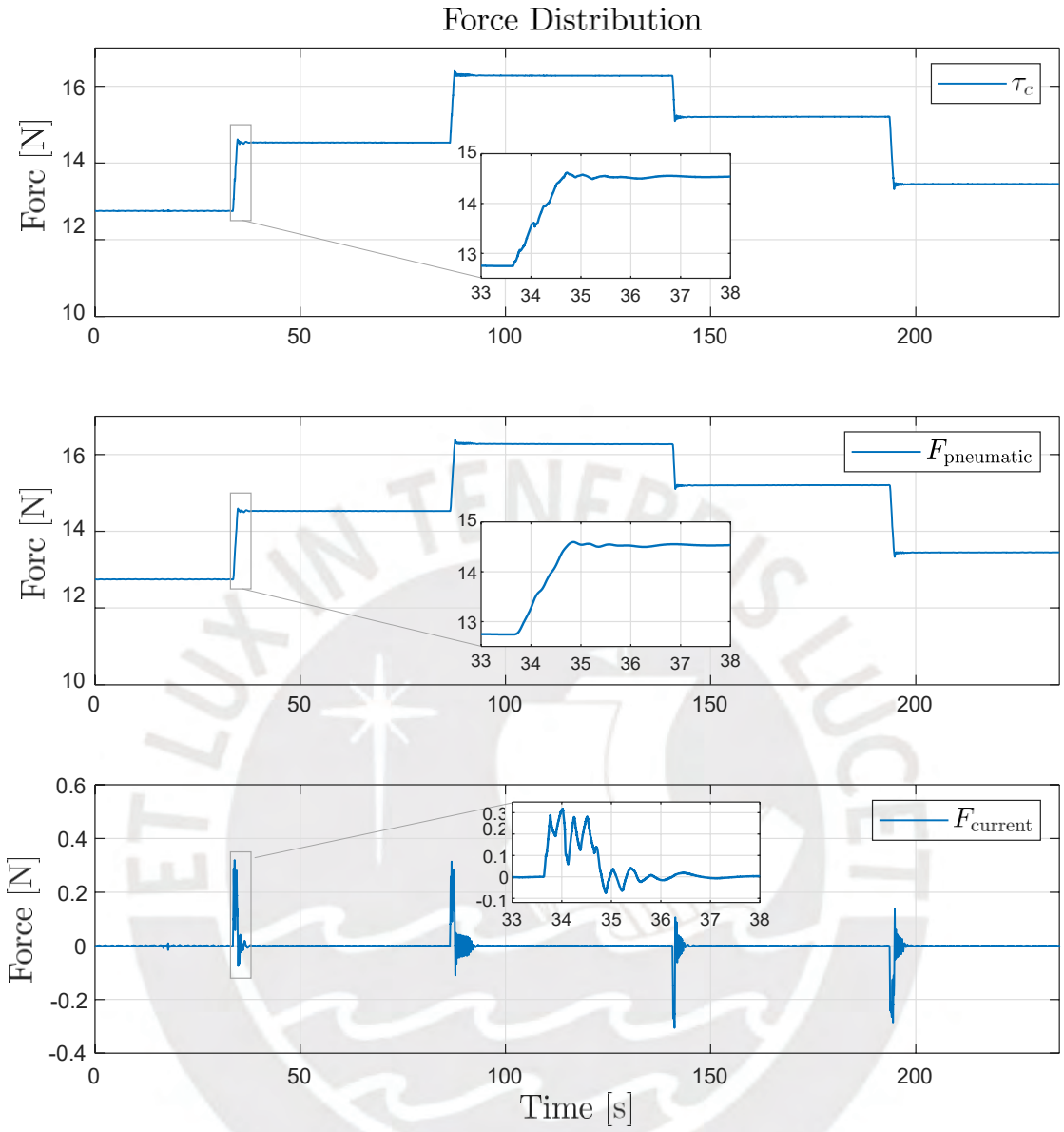

Figure 5.5: Force distribution for a step input in the millimeter range.

5.2 Nanometer Range

At the nanometer scale, additional conditions become evident. The system response to steps with an amplitude of 100 nm and 10 nm, at the operation point of 2.555 mm, are shown in Figure 5.6. It is possible to appreciate the higher step among the measured position variation, nevertheless smaller position steps, such as 10 nm, are only observable after the signal is processed with a moving average filter.

The position deviation in the order of µm due to the constant pressure mentioned in Section 2.6.1 is greatly reduced. The position variation is bounded between ±50 nm at steady condition. In this direction, the disturbance observer with fine tuned parameters contributes to reducing this effect.

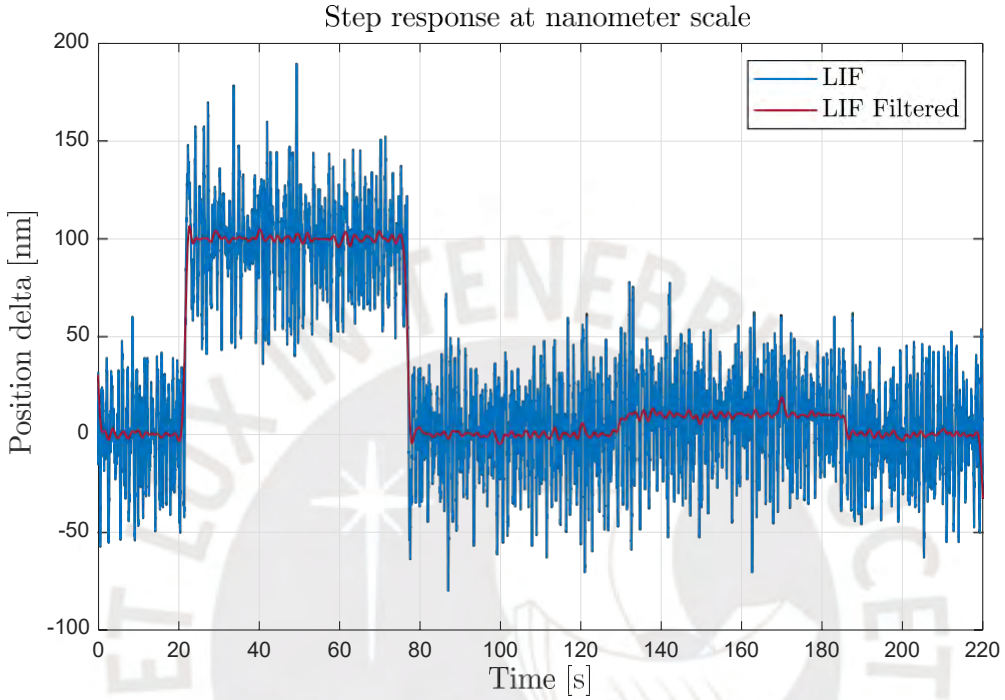

Figure 5.6: LAU step response in nanometer range at 2.555 mm

The estimated disturbance force $\hat{F}_d$ presents a similar behavior to the millimeter range as shown in Figure 5.7. The disturbance observer estimates the force deviation with respect to the magnetic force due to the hysteresis in a step change. Moreover, it is capable to estimate the smaller force component due to the pressure disturbance in order to counteract the position deviation. The slow changing interferometer measurement drift, similar to mentioned in Section 2.2, is perceptible at nanoscale. Since it is not possible to identify the source of drift, is it considered as part of an internal force to compensate.

Figure 5.8 shows the force distribution through the dynamic control allocation stage for a small control effort variation. In this scenario, the pneumatic actuator provides the low frequency force component and generates 14.85 N through 0.4719 bar to support the LAU at 2.555 mm. In addition, a force variation of 4 mN is provided due to the 100 nm step change.

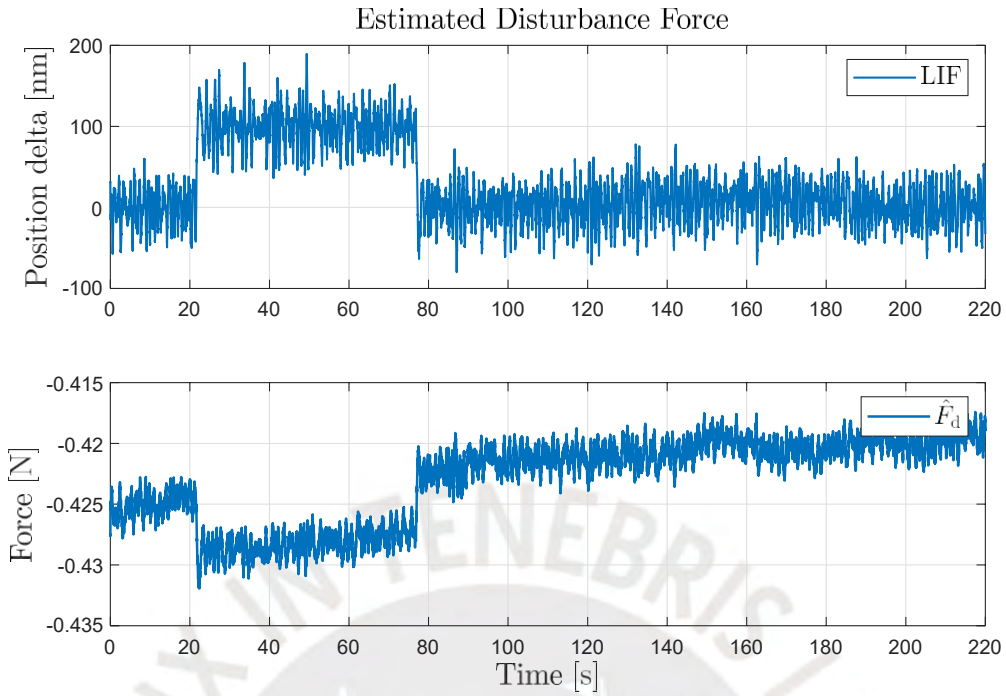

Figure 5.7: Estimated disturbance force for a nanometer range displacement.

Nevertheless, the DCA property to assign the high frequency component to the faster actuator has an increased impact at this scale. It enables the system to generate an accurate control effort τ_c, required in the disturbance rejection structure so that the position deviation in the presence of disturbances is reduced. In this sense, the voice coil motor handles the fast changing force component. In the case presented in Figure 5.8, it generates a maximum positive force of 2.4 mN (0.7458 mA) and a maximum negative force of −3.1 mN (−0.9650 mA) that represents power consumption peaks of 1.0012 µW and 1.6762 µW, respectively. The average current during the experiment is −1.5 µA.

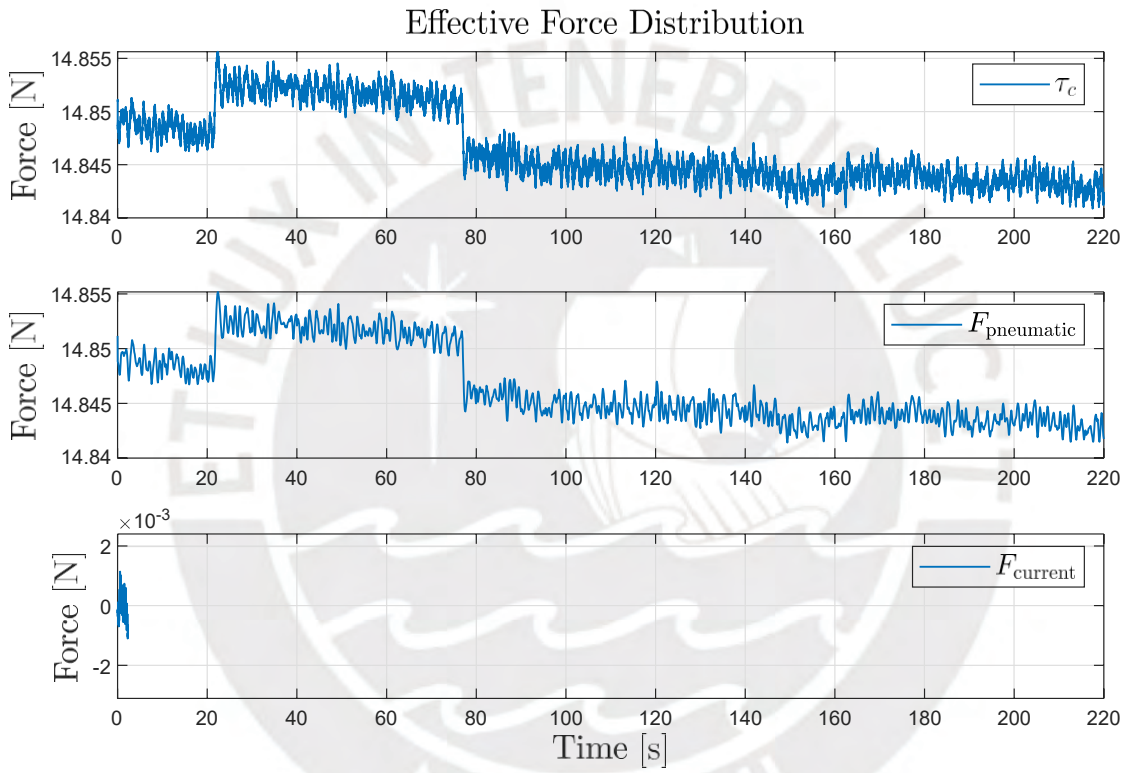

Figure 5.8: Force distribution for a step input in the nanometer range.

6 Conclusion and Future Work

In this work, a control structure for the LAU nanopositioning system based on dynamic control allocation is proposed. The control allocation structure allows separating the design of the high level controller from the force distribution stage. Therefore, the thesis requirement of system stability and precision are regarded to the high level controller. Whereas, the allocation stage design determines the control input for the actuator set based on the requirement to use the pneumatic actuator as a passive gravity compensation and the VCM for fine force adjustment.

In Chapter 2, the LAU motion and actuators dynamics are modeled. The obtained information serves to identify the implementation restrictions such as the maximum travel speed limit. The determined actuator bandwidth is also a design criterion for the force distribution method.

A dynamic control allocation approach is decided as the actuator dynamics effects are significant with respect to the LAU motion dynamics. The control effort distribution is based on frequency allocation criterion. The low and high frequencies components of the required force are divided through an LPF with a cutoff frequency of 3 Hz. The constant and slow varying force is assigned to the pneumatic actuator while the higher frequencies components are handled by the voice coil drive. Then, a Kalman Filter compensation stage is designed to minimize the actuator effects on the determined control input. The simulations and experimental results clearly show that the pneumatic actuator produces constant and slow varying forces while the VCM handles the high frequency forces. In this sense, the objective of the pneumatic actuator as a passive gravity compensation is achieved.

The LAU system has an unmodeled internal magnetic force with hysteresis behavior regarded as model uncertainties. Furthermore, the pressure input has an important disturbance component. Under these conditions, an EKF disturbance observer is proposed to estimate the disturbances and uncertainties in form of a joint force. The

weighting matrices are regarded as tuning parameters defined through experiments. As a result, it is possible to observe the variation of the estimated disturbance force according to the LAU displacement. In conjunction with the high level controller, it is possible to control the position with nanometer precision. Nevertheless, the experimental results show a position variation of $\pm 50\,\text{nm}$ due to the disturbance.

The flexibility of the proposed method, due to the separation concept of the high level controller from the allocation stage, opens the possibility of several improvements and alternative implementations. For instance, the high level controller can be improved with a hysteresis model of the magnetic force. Furthermore, robust and adaptive controllers can be implemented. Optimal control methods with speed constraints can be investigated. In addition, a reference trajectory generation can be used instead of a setpoint speed limit profile.

Regarding the control allocation stage, it is possible to enhance its functionality by including an actuator constraints evaluation. The proposed method can be applied to a LAU based platform with 6 degrees of freedom. In this case, the effectiveness matrix needs to be updated; however, the frequency allocation concept still applies. Finally, alternative compensation techniques based on the measured input variable can be investigated.

Abbreviations

AFM	Atomic Force Microscopy
CA	Control Allocation
D2W	Die-to-Wafer
DCA	Dynamic Control Allocation
DPN	Dip-Pen Nanolithography
EKF	Extended Kalman Filter
EURAMET	European Association of National Metrology Institutes
EUV	Extreme Ultraviolet
FE-SPL	Field-emission SPL
IC	Integrated Circuit
IRDS	International Roadmap for Devices and Systems
KF	Kalman Filter
LAU	Lifting and Actuating Unit
LIF	Laser Interferometer
LPF	Low Pass Filter
MISO	Multiple Input Single Output
NPMM	Nanopositioning and Nanomeasuring Machines
PRBS	Pseudo-random Binary Sequence
SPL	Scanning Probe Lithography
SPM	Scanning Probe Microscopy

SRA	Strategic Research Agenda
UHV	Ultra High Vacuum
UV-NIL	UV-Nanoimprint Lithography
VCM	Voice Coil Motor
W2W	Wafer-to-Wafer

List of Figures

Bibliography

[1] A. S. Ball, S. Patil, and S. Soni, "Chapter 1 - introduction into nanotechnology and microbiology," in *Nanotechnology*, ser. Methods in Microbiology, V. Gurtler, A. S. Ball, and S. Soni, Eds. Academic Press, 2019, vol. 46, pp. 1 – 18.

[2] M. C. Roco, "Overview," in *Nanotechnology Commercialization*. John Wiley & Sons, Ltd, 2017, ch. 1, pp. 1–23.

[3] S. T. Picraux, "Nanotechnology," 2018.

[4] EURAMET, *Strategic Research Agenda for Metrology in Europe*. EURAMET e.V., 2016, pp. 3–5,7,48–49.

[5] G. Jäger, E. Manske, T. Hausotte, A. Müller, and F. Balzer, "Nanopositioning and nanomeasuring machine NPMM-200—a new powerful tool for large-range micro- and nanotechnology," *Surface Topography: Metrology and Properties*, vol. 4, no. 3, p. 034004, jul 2016.

[6] D. E. Babatunde, I. H. Denwigwe, O. M. Babatunde, S. L. Gbadamosi, I. P. Babalola, and O. Agboola, "Environmental and societal impact of nanotechnology," *IEEE Access*, vol. 8, pp. 4640–4667, 2020.

[7] IEEE, *The International Roadmap for Devices an Systems : 2018*, 2019, ch. Metrology, pp. 1–3.

[8] ASML, "Big steps in tiny patterns - euv lithography," 2019.

[9] E. Rani and L. S. Wong, "High-resolution scanning probe nanolithography of 2d materials: Novel nanostructures," *Advanced Materials Technologies*, vol. 4, no. 7, p. 1900181, 2019.

[10] M. Holz, E. Guliyev, A. Ahmad, T. Ivanov, A. Reum, M. Hofmann, C. Lenk,

M. Kaestner, C. Reuter, S. Lenk, I. W. Rangelow, and N. Nikolov, "Field-emission scanning probe lithography tool for 150mm wafer," *Journal of Vacuum Science & Technology B*, vol. 36, no. 6, p. 06JL06, 2018.

[11] S. T. Howell, A. Grushina, F. Holzner, and J. Brugger, "Thermal scanning probe lithography—a review," *Microsystems & Nanoengineering*, vol. 6, no. 21, 2020.

[12] G. Liu, S. H. Petrosko, Z. Zheng, and C. A. Mirkin, "Evolution of dip-pen nanolithography (dpn): From molecular patterning to materials discovery," *Chemical Reviews*, 2020.

[13] M. Hofmann, S. Mecholdt, M. Mohr, M. Holz, S. Dallorto, E. Manske, H.-J. Fecht, and I. W. Rangelow, "Nanoscale lift-off process using field emission scanning probe lithography," *Journal of Vacuum Science & Technology B*, vol. 37, no. 6, p. 061803, 2019.

[14] M. Kühnel, T. Fröhlich, R. Füßl, M. Hoffmann, E. Manske, I. Rangelow, J. Reger, C. Schäffel, S. Sinzinger, and j.-p. Zöllner, "Towards alternative 3d nanofabrication in macroscopic working volumes," *Measurement Science and Technology*, vol. 29, 08 2018.

[15] L. Weidenfeller, M. Hofmann, J. Kirchner, S. Supreeti, I. W. Rangelow, S. Sinzinger, and E. Manske, "Micro- and nanofabrication technologies using the nanopositioning and nanomeasuring machines," in *Optical Measurement Systems for Industrial Inspection XI*, P. Lehmann, W. Osten, and A. A. G. Jr., Eds., vol. 11056, International Society for Optics and Photonics. SPIE, 2019, pp. 817 – 829.

[16] S. Gorges, S. Hesse, C. Schäffel, I. Ortlepp, E. Manske, E. Langlotz, and D. Dontsov, "Integrated planar 6-dof nanopositioning system," *8th IFAC Symposium on Mechatronic Systems MECHATRONICS 2019*, vol. 52, no. 15, pp. 313 – 318, 2019.

[17] A. Okyay, M. B. Khamesee, and K. Erkorkmaz, "Design and optimization of a voice coil actuator for precision motion applications," *IEEE Transactions on Magnetics*, vol. 51, no. 6, pp. 1–10, 2015.

[18] H. Zhang, B. Kou, Y. Jin, H. Zhang, and Y. Zhou, "Analysis and optimization of an electromagnetic actuator with passive gravity compensation," in *2016 19th International Conference on Electrical Machines and Systems (ICEMS)*, 2016, pp. 1–6.

[19] Z. Gong, Z. Zhang, L. Zhang, R. Yang, Y. Liu, and H. Huang, "Reliability enhancement test of vertical voice-coil motor on wafer stage of lithography machine," in *2013 International Conference on Quality, Reliability, Risk, Maintenance, and Safety Engineering (QR2MSE)*, 2013, pp. 991–995.

[20] E. Asadi, A. Khajepour, and M. B. Khamesee, "A new low-profile electromagnetic-pneumatic actuator for high-bandwidth applications," *IEEE/ASME Transactions on Mechatronics*, vol. 23, no. 5, pp. 2207–2217, 2018.

[21] S. Gorges, B. Leistritz, S. Hesse, I. Ortlepp, G. Slotta, C. Schäffel, and Ilmenau Scientific Colloquium. Technische Universität Ilmenau ; 59 (Ilmenau) : 2017.09.11-15, "Development of an integrated guiding and actuation element for high dynamic nanopositioning systems," *Engineering for a Changing World: Proceedings; 59th IWK, Ilmenau Scientific Colloquium, Technische Universität Ilmenau, September 11-15, 2017*, vol. 59, 2017, no. 1.1.05, Oct 2017.

[22] Q. Chen, N. Yin, and X. Chen, "Energy consumption analysis of a linear motor," in *2018 IEEE 3rd Advanced Information Technology, Electronic and Automation Control Conference (IAEAC)*, 2018, pp. 1523–1527.

[23] Solenoid Systems, "Analyzing magnetic and mechanical hysteresis in a proportional solenoid," 2016.

[24] M. Ruderman, "Stroke-dependent magnetic hysteresis modeling in proportional solenoids using parametric gaussian-mixture preisach distribution," in *2014 IEEE/ASME International Conference on Advanced Intelligent Mechatronics*, 2014, pp. 1587–1591.

[25] M. Balakrishnan and N. Kumar N, "Detection of plunger movement in dc solenoids," 2015.

[26] K. Kołek and M. Rosół, "Velocity estimation for slow motion devices equipped with encoder," in *2017 22nd International Conference on Methods and Models in Automation and Robotics (MMAR)*, 2017, pp. 809–814.

[27] D. S. Bernstein, "Ivory ghost [ask the experts]," *IEEE Control Systems Magazine*, vol. 27, no. 5, pp. 16–17, 2007.

[28] Y. He, C. Zhang, J. Gao, C. Cui, Z. Yang, X. Chen, K. Zhang, Y. Chen, and

H. Tang, "Research on position force control based on voice coil motor," in *2018 19th International Conference on Electronic Packaging Technology (ICEPT)*, 2018, pp. 1079–1083.

[29] F. Golnaraghi and B. Kuo, *Automatic Control Systems*, 10th ed. McGraw-Hill, 2017.

[30] H. K. Khalil, *Nonlinear Systems*, 3rd ed. Pearson, 2002, ch. Lyapunov Stability, pp. 133–139.

[31] F. Golnaraghi and B. Kuo, *Automatic Control Systems*, 10th ed. McGraw-Hill, 2017.

[32] T. A. Johansen and T. I. Fossen, "Control allocation - a survey," *Automatica*, vol. 49, no. 5, pp. 1087 – 1103, 2013.

[33] O. Härkegård and S. T. Glad, "Resolving actuator redundancy—optimal control vs. control allocation," *Automatica*, vol. 41, no. 1, pp. 137 – 144, 2005.

[34] A. Casavola and E. Garone, "Fault-tolerant adaptive control allocation schemes for overactuated systems," *International Journal of Robust and Nonlinear Control*, vol. 20, no. 17, pp. 1958–1980, 2010.

[35] M. W. Oppenheimer, D. B. Doman, and M. A. Bolender, "Control allocation for over-actuated systems," in *2006 14th Mediterranean Conference on Control and Automation*, 2006, pp. 1–6.

[36] O. Harkegard, "Efficient active set algorithms for solving constrained least squares problems in aircraft control allocation," in *Proceedings of the 41st IEEE Conference on Decision and Control, 2002.*, vol. 2, 2002, pp. 1295–1300 vol.2.

[37] O. Härkegård, "Dynamic control allocation using constrained quadratic programming," *Journal of Guidance, Control, and Dynamics*, vol. 27, no. 6, pp. 1028–1034, 2004.

[38] G. M. Clayton, C. J. Dudley, and K. K. Leang, "Range-based control of dual-stage nanopositioning systems," *Review of Scientific Instruments*, vol. 85, no. 4, p. 045003, 2014.

[39] M. Kirchengast, M. Steinberger, and M. Horn, "Input matrix factorizations for

constrained control allocation," *IEEE Transactions on Automatic Control*, vol. 63, no. 4, pp. 1163–1170, 2018.

[40] B. Ye, J. Xiong, Q. Wang, and Y. Luo, "Design and implementation of pseudo-inverse thrust allocation algorithm for ship dynamic positioning," *IEEE Access*, vol. 8, pp. 16 830–16 837, 2020.

[41] J. Stephan and W. Fichter, "Fast exact redistributed pseudoinverse method for linear actuation systems," *IEEE Transactions on Control Systems Technology*, vol. PP, pp. 1–8, 11 2017.

[42] H. Yang and Q. Hu, "Research and experiment on dynamic weight pseudo-inverse control allocation for spacecraft attitude control system," in *2019 Chinese Control Conference (CCC)*, 2019, pp. 8200–8205.

[43] M. Naderi, T. Johansen, and A. Khaki-Sedigh, "A fault tolerant control scheme using the feasible constrained control allocation strategy," *International Journal of Automation and Computing*, pp. 1–16, 2019.

[44] D. Wang, Q. Yang, and P. Ge, "Diffeomorphism transformation based disturbance rejection control and its allocation of vehicle dynamic stable systems," *IEEE Access*, vol. 7, pp. 105 734–105 745, 2019.

[45] E. Dyer, S. Sirouspour, and M. Jafarinasab, "Energy optimal control allocation in a redundantly actuated omnidirectional uav," in *2019 International Conference on Robotics and Automation (ICRA)*, 2019, pp. 5316–5322.

[46] *Energy-Efficient Control Allocation for Over-Actuated Systems With Electric Vehicle Applications*, ser. Dynamic Systems and Control Conference, vol. ASME 2010 Dynamic Systems and Control Conference, Volume 1, 09 2010.

[47] L. Zaccarian, "Dynamic allocation for input redundant control systems," *Automatica*, vol. 45, no. 6, pp. 1431 – 1438, 2009.

[48] F. Lallman, J. Davidson, and W. Bundick, *Integrated reconfigurable control allocation*, 2001.

[49] M. W. Oppenheimer and D. B. Doman, "A method for compensation of interactions between second-order actuators and control allocators," in *2005 IEEE Aerospace*

Conference, 2005, pp. 1–8.

[50] M. Oppenheimer and D. B. Doman, "Methods for compensating for control allocator and actuator interactions," *Journal of Guidance Control and Dynamics*, vol. 27, pp. 922–927, 2004.

[51] M. Kissai, B. Monsuez, X. Mouton, D. Martinez, and A. Tapus, "Model predictive control allocation of systems with different dynamics," in *2019 IEEE Intelligent Transportation Systems Conference (ITSC)*, 2019, pp. 4170–4177.

[52] G. Morani, F. Nebula, F. Corraro, and M. Ariola, "Dynamic control allocation through kalman filtering," *American Journal of Engineering and Applied Sciences*, vol. 12, pp. 46–56, 01 2019.

[53] S. Devasia, E. Eleftheriou, and S. O. R. Moheimani, "A survey of control issues in nanopositioning," *IEEE Transactions on Control Systems Technology*, vol. 15, no. 5, pp. 802–823, 2007.

[54] E. Sariyildiz, R. Oboe, and K. Ohnishi, "Disturbance observer-based robust control and its applications: 35th anniversary overview," *IEEE Transactions on Industrial Electronics*, vol. 67, no. 3, pp. 2042–2053, 2020.

[55] B. Noack, "State estimation for distributed systems with stochastic and set-membership uncertainties," Ph.D. dissertation, 2014.

[56] M. S. Grewal and A. P. Andrews, *Kalman Filtering*. John Wiley & Sons, Ltd, 2008, ch. General Information, pp. 1–29, 293–297.

[57] F. L. Lewis, L. Xie, and D. Popa, *Optimal and Robust Estimation With an Introduction to Stochastic Control Theory*. CRC Press, 2008, pp. 70 – 90.

[58] H. K. Khalil, *Nonlinear Systems*, 3rd ed. Prentice-Hall, 2002, ch. Feedback Linearization, pp. 508,510,516.

[59] A. Isidori, *Nonlinear Control Systems*, 3rd ed. Springer-Verlag, 1995, ch. Elementary Theory of Nonlinear Feedback for Single-Input Single-Output Systems, p. 152.